DEVELOPMENT AND ANALYSIS OF ALL DIODE LASER ns-MOPA SYSTEMS FOR HIGH PEAK POWER APPLICATIONS

vorgelegt von
Master of Science
THI NGHIEM VU
aus Nghe An, Vietnam

von der Fakultät II
Mathematik und Naturwissenschaften
der Technischen Universität Berlin
zur Erlangung des akademischen Grades
Doktor der Naturwissenschaften
- Dr. rer. nat. -

genehmigte Dissertation

Promotionsausschuss:
Vorsitzender: Prof. Dr. Michael Lehmann
Gutachter: Prof. Dr. Michael Kneissl
Gutachter: Prof. Dr. Günther Tränkle
Gutachter: Prof. Dr. Martin Hofmann

Tag der wissenschaftlichen Aussprache: 24. January 2017

Berlin 2017

Contents

Abstract i

Zusammenfassung iv

Acknowledgements vii

1 Introduction 1

2 Basic principle of LIDAR and DIAL systems-light sources for LIDAR and DIAL 6

2.1 Basic principle of LIDAR system and basic equation 6
2.2 Differential absorption LIDAR (DIAL) for gas measurements, e.g., water vapor profiling 11
2.3 Specific requirements of laser systems for LIDAR and DIAL 15
2.4 Current status of diode laser based MOPA systems as laser transmitters for aerosols and water vapor 20

3 Diode laser based MOPA concept approaches 25

3.1 Monolithic MOPA concept 26
3.2 Hybrid MOPA concepts 28
3.2.1 Master oscillators 28
3.2.1.1 RW-DFB laser as master oscillator 31
3.2.1.2 Dual wavelength Y-branch-DFB lasers . . 34
3.2.2 Multi-section tapered power amplifiers 36
3.2.2.1 Four-section tapered power amplifier 37
3.2.2.2 Two-section tapered power amplifier 38

4 Experimental setup 40

4.1 Characterization under continuous wave excitation 40
4.1.1 Electro-optical characterization 40
4.1.2 Spectral properties 42
4.2 Characterization under ns-pulsed excitation 44
4.3 Electrical circuit for high current at ns-pulses regime 50

5 Wavelength stabilized diode laser based ns-MOPA 52

5.1 Monolithic MOPA 52
5.1.1 Characterization of the tapered section without seeding 53

5.1.2 Timing scheme for high power and low amplified spontaneous emission . . . 54
5.1.3 Spectral properties . . . 59
5.2 Hybrid MOPA concepts . . . 62
5.2.1 RW-DFB laser characterization . . . 62
5.2.2 Characterization of the tapered power amplifier under ns-pulse excitation . . . 64
5.2.3 The behavior of optical power and amplified spontaneous emission under delay time . . . 66
5.2.4 Spectral properties . . . 72
5.3 Conclusion . . . 74

6 Tunable wavelength ns-MOPA diode lasers **75**
6.1 Tunable RW-DFB laser . . . 76
6.2 Amplified spontaneous emission under ns-pulse excitation . 78
6.3 Dependence of output powers on input powers, saturation behavior . . . 80
6.4 Spectral tuning properties . . . 85
6.5 Conclusion . . . 89

7 Dual wavelength diode laser based MOPA systems **91**
7.1 Dual wavelength Y-branch-DFB laser as master oscillator . 92
7.2 Amplified spontaneous emission under ns-pulse excitation . 95
7.3 Optical power and spectral properties of MOPA system with dual wavelength . . . 95
7.4 Conclusion . . . 99

8 Conclusion and outlook **100**
8.1 Conclusion . . . 100
8.2 Outlook . . . 102

List of Abbreviations and Symbols **103**

List of Publications **106**

Bibliography **109**

Abstract

The aim of this work is to design and characterize all-diode laser based master oscillator power amplifier ($MOPA$) systems, which operate in the ns-pulse region with peak powers in the range of more than 10 W. They should provide the ability to be implemented into micro light detection and ranging ($LIDAR$) or differential absorption $LIDAR$ ($DIAL$) systems, commonly known as Micro Pulse Lidar systems ($MPLs$). The $MPLs$ then enable to detect aerosols and water vapor in the lower troposphere, the lowest layer of the earth's atmosphere which is about 6 -10 km above the sea level. Thus the diode laser based $MOPA$ systems have to fulfill the requirements of laser transmitters in $MPLs$ for aerosols and water vapor measurement.

Due to varying spatial distribution of aerosols and water vapor, the resolution of the $LIDAR$ system needs to be high both in vertical and lateral directions. The response time for the detection of the photons determines the spatial resolution of the $LIDAR$ measurement, e.g. a response time in the ns-pulse regime corresponds to a resolution in the m range. To distinguish between the resolution intervals, the emitted laser pulse should have a length well below the response time of the system. The repetition rate of the laser transmitter determines the maximal time interval between emission and detection without a temporal overlap of the emitted pulses. Together with the speed of light the possible measuring range can be calculated. A repetition rate of 25 kHz, i.e. a time between two pulses of 40 μs corresponds to a measuring range of 6000 m.

For gas absorption measurements, the spectral line width of the laser transmitter has to be narrower than the gas absorption line width. The spectral line width of water vapor at atmospheric pressure is about 10 pm at wavelength of 975 nm, therefore a line width below 10 pm of the laser transmitter is needed. For aerosols, only the intensity of the back scattered signal is of interest, so that a laser with a broad spectral line width together with a filter of 300 pm can be used. This linewidth is required to suppress the sunlight background of the daytime operation.

Two $MOPA$ concepts are demonstrated. One is a monolithic $MOPA$

and the other is a hybrid $MOPA$ system.

The monolithic $MOPA$ is a compact device where the MO and the PA are integrated on one single chip. It operates at a wavelength of 1064 nm. A peak power of about 16.3 W at a pulse width of 3 ns and a repetition rate of 800 MHz are obtained. At this power, a spectral line width of about 150 pm is achieved, which is sufficient for the detection of aerosols. However, the spectral width is not suited for water vapor detection.

The hybrid $MOPA$ concept features separated chips for the seed laser (the MO) and the power amplifier (PA). It allows to freely adjust and individually control the operation conditions of the MO and the PA as well as specifically select each device for desired purposes. In this work, three hybrid $MOPA$ systems providing stabilized, tunable and dual wavelengths are investigated. A stabilized wavelength is required for specific absorption line detection, whereas a tunable wavelength emission allows scanning over several absorption lines. Dual wavelength emission enables switching between on and off resonance detection of the spectral absorption lines. As master oscillators for these applications either distributed feedback (DFB) lasers or $Y-branch-DFB$ lasers are employed. In order to achieve high optical output power operation in the ns-pulse regime, multi-section tapered power amplifiers are used. The MO is operated in continuous wave (CW) mode to provide a narrow spectral line width. The multi-section tapered amplifier consists of a ridge wave-guide section used as optical gate (OG) for the generation of short pulses and a tapered section (TS) for the amplification of the generated pulses.

The hybrid $MOPA$ system operates at a wavelength of 1064 nm with a stable spectral line width of below 10 pm and a side mode suppression ratio ($SMSR$) larger than 46 dB. A peak power of 16 W at a pulse width of 3 ns is achieved at a repetition rate of 800 MHz. By adjustment of timing delay between the OG and the TS with respect to the shape of the laser pulse, ideally a flat-top-hat-like and a small value of ASE, the optimized excitation timing is found. It is related to the lifetime of carriers and the time needed to create the carrier density inversion in the upper level. In this case an amount of amplified spontaneous

emission (ASE) smaller than 1% is observed. These parameters meet the demands of a light source suitable for the measurement of absorption lines of molecular species under atmospheric condition.

A hybrid $MOPA$ system operation at 975 nm is investigated to target absorption lines of water vapor detection. The pulse width and repetition rate are varied to adapt to the expected resolution and measured range. For concentration calibration, adjustment of the working points and the selection of suitable absorption lines, the system could not only be stabilized at a specific wavelength but also be tuned continuously for scanning over several absorption lines. A tuning range of 0.9 nm is obtained by adjustment of the injected current into the DFB laser. This allows to scan over several absorption lines of water vapor. A constant spectral line width of below 10 pm and a $SMSR$ larger 40 dB are achieved at a peak power of 16.3 W at a pulse width of 8 ns and at a repetition rate of 25 kHz. An amounts of ASE of smaller than 1% is observed.

In differential absorption $LIDAR$ ($DIAL$), two wavelengths for on /off lines are needed. A hybrid $MOPA$ system featuring a dual wavelength is investigated for this purpose. The $MOPA$ consists of a $Y-branch-DFB$ laser as MO and a two-section tapered amplifier as PA. The $Y-branch-DFB$ laser emits alternatively at two wavelengths, which can be finely tuned by current and temperature. Thus a desired pair of wavelengths for *on* and off resonance of water vapor absorption lines can be selected. Two pair wavelengths at two absorption lines of water vapor (different absorption coefficients) are selected. A stable behavior of peak power, spectral line width and $SMSR$ at each wavelength is observed. It is a suitable system for ($DIAL$) application.

In summary, we have developed all-semiconductor diode laser based $MOPA$ systems suitable for the laser transmitter in MPL applications, which can be used for detection of atmospheric gases, such as H_2O, and aerosols. They are potentially applicable in $LIDAR$ or $DIAL$ and would allow a new generation of ultra-compact, low cost systems.

Zusammenfassung

Die Zielstellung dieser Arbeit ist es, Diodenlasersysteme zu charakterisieren, welche potentiell für die Detektion von Aerosolen und Wasserdampf in der tiefen Troposphäre geeignet sind. Diese Lasersysteme sollen die Voraussetzungen schaffen, um in ein laserbasiertes Detektions und Fernmessung atmosphärischer Parameter (engl. *LIDAR* - LIght Detection And Ranging) oder ein miniaturisiertes Differentialabsorptions-LIDAR (engl. *DIAL* - DIfferential Absorption LIDAR) integriert werden zu können. Dementsprechend sollen Diodenlasersysteme die Rolle als Lasertransmitter in Mikropuls LIDAR (engl. *MPL* - Micro Pulse *LIDAR*) Systemen für die Detektion von Aerosolen und Wasserdampf übernehmen.

Es werden zwei Konzepte mit gekoppeltem Leistungsverstärker (engl. *MOPA* - Master Oscillator Power Amplifier) untersucht, zum Einen ein monolithisches, zum Anderen ein hybrides *MOPA* System. Das monolithische *MOPA* System ist ein äußerst kompaktes System, bei dem der Masterlaser (engl. *MO* - Master Oscillator) und Leistungsverstärker (engl. *PA* - Power Amplifier) auf dem selben Chip untergebracht sind. Dieser emittiert bei einer Wellenlänge von 1064 nm, einer Standardwellenlänge für die Detektion von Aerosolen. Hier wird eine Spitzenleistung von 16.3 W bei einer Pulsbreite von 3 ns und einer Wiederholrate von 800 MHz erreicht. Bei dieser Leistung wird eine spektrale Linienbreite von 150 pm erreicht, was ausreichend ist für die Detektion von Aerosolen. Bei der Messung der Verteilung von Aerosolpartikeln ist lediglich die Intensität des rückgestreuten Lichts von Interesse, weshalb ein Laser mit großer spektraler Linienbreite zusamment mit einem Band-pass Filter eingesetzt werden kann. Damit lässt sich das durch Sonnenlicht verursachte Rauschen im Tages messungen ausreichend unterdrücken.

Für die Messung der Absorption von Gasen muss die spektrale Linienbreite des Lasers schmaler sein als die Absorptionslinie des Gases. Im Falle von Wasserdampf in der Atmosphäre ist die spektrale Linienbreite ca. 10 pm breit. Das hybride *MOPA* Konzept mit separaten Chips für *MO* und *PA* wird ebenfalls vorgestellt. Es kann frei an den

gewünschten Einsatzzweck angepasst werden und erlaubt eine individuelle Aussteuerung des MO und PA.

Das hybride $MOPA$ Konzept bietet die Möglichkeit zur Wellenlängenstabilisierung, Durchstimmbarkeit oder des dualen Wellenlängenbetriebes. Eine Wellenlängenstabilisierung wird für die Detektion von spezifischen Wellenlängen benötigt. Die Durchstimmbarkeit gewährleistet, dass über mehrere Absorptionslinien gescannt werden kann. Dualer Wellenlängenbetrieb erlaubt es, zwischen on und off Resonanzbedingung spektraler Absorptionslinien umzuschalten. Der MO für diese Anwendungen kann entweder ein Laser mit verteilter Rückkopplung (engl. DFB - Distributed FeedBack) oder ein Y-DFB-Laser sein. Um eine ns-Pulsbreite und hohe optische Ausgangsleistung zu erreichen, werden Mehrsektions-Trapezverstärker eingesetzt. Der Betrieb des MO im Dauerstrichbetrieb gewährleistet eine schmale spektrale Linienbreite. Der Mehrsektions-Trapezverstärker besteht aus einer Rippenwellenleiter Sektion, verwendet als optischer Schalter (engl. OG - Optical Gate) für die Generierung von kurzen Pulsen, und einer Trapezförmigen Sektion (engl. TS - Tapered Section) zur Verstärkung des Pulses.

Das hybride $MOPA$ System emittiert bei einer Wellenlänge von 1064 nm mit einer stabilisierten spektralen Linie unterhalb von 10 pm sowie einer Nebenmoden unterdrückung (engl. $SMSR$ - Side Mode Supression Ratio) größer als 46 dB. Eine Spitzenleistung von 16 W bei einer Pulsbreite von 3 ns wird bei einer Wiederholrate von 800 MHz erreicht. Durch die Anpassung der Zeitverzögerung zwischen OG und TS kann ein optimales Anregungsverhalten erreicht werden. Dieses ist abhängig von den Ladungsträgerdichten und der benötigten Zeit, um die Besetzungsinversion zu erzeugen. In diesem Fall ist der Teil der emittierten spontanen Emission (engl. ASE - Amplified Spontaneous Emission) kleiner als 1%. Diese Parameter erfüllen die Voraussetzungen einer Lichtquelle, welche für die Messung von molekularen Absorptionslinien unter atmosphärischen Bedingungen geeignet ist.

Für das Ziel der Detektion von Wasserdampf in der unteren Troposphäre wird ein hybrides $MOPA$ System bei einer Wellenlänge von 975 nm untersucht, da hier Absorptionslinien von Wasserdampf liegen. Dabei werden die Pulsbreiten und Wiederholraten variiert, um die er-

wartete Auflösung und den erforderlichen Messbereich zu erreichen. Zur Konzentrationskalibrierung und Einstellung der Arbeitspunkte und der Auswahl geeigneter Absorptionslinien sollte das System nicht nur bei einer bestimmten Wellenlänge stabilisiert sein, sondern auch kontinuierlich durchstimmbar, um über mehrere Absorptionslinie scannen zu können. Durch passende Regelung des in den DFB Laser injizierten Stromes wird ein Durchstimmbereich von 0.9 nm erhalten. Eine konstante spektrale Linienbreite von unter 10 pm und ein $SMSR$ von über 40 dB werden bei einer Spitzenleistung von 16.3 W bei einer Pulsbreite von 8 ns und einer Wiederholrate von 25 kHz erreicht. Ein ASE Anteil von unter 1% wird dabei beobachtet. Dieses Ergebnis deckt sich mit der Simulation. Mit dem gegebenen Durchstimmbereich lässt sich über mehrere Absorptionslinien von Wasserdampf scannen.

Für das Differenzabsorptions $LIDAR$ (engl. $DIAL$ - DIfferential Absorption $LIDAR$) Verfahren sind zwei Wellenlängen für $on-off$ Resonanz nötig. Das hybride $MOPA$ System benutzt dafür einen $Y-DFB$-Laser als MO und einen Zweisektionen PA. Der $Y-DFB$-Laser emittiert alternierend bei zwei Wellenlängen, welche fein eingestellt werden können, indem Strom und Temperatur angepasst werden, damit ein geeignetes Wellenlängenpaar für $on-off$ Resonanzen gewählt werden kann. In dieser Arbeit werden zwei Wellenlängenpaare für zwei Absorptionslinien von Wasserdampf untersucht. Es wird stabiles Verhalten der Spitzenleistung, der spektralen Linienbreite und des $SMSR$ bei jeder der untersuchten Wellenlängen beobachtet. Somit ist dies eine ideale Konfiguration für $DIAL$ Systeme.

Zusammenfassend wurden Halbleiterdiodenlaser-basierte $MOPA$ Systeme entwickelt, die als Lasertransmitter geeignet für MPL-Anwendungen sind, welche für die Detektion von Atmosphärengasen wie Wasserdampf und Aerosole verwendet werden können. Sie sind potentiell einsetzbar in Mikro-$LIDAR$-Systemen und ermöglichen eine neue Generation von ultrakompakten und kostengünstigen Systemen.

Acknowledgements

First and foremost, I would like to express my sincere gratitude to Prof. Dr. Günther Tränkle for offering me the opportunity to conduct research leading to the results of this work at the Ferdinand-Braun-Institut, Leibniz-Institut für Höchstfrequenztechnik. His active interest in my work, his constant advice and encouragement have been of great help in daily life and the research works during the course of this work.

I wish to convey my gratitude to Dr. Bernd Sumpf for his daily guidance and constructive ideas. His permanent availability to provide advice and support in terms of physical and organizational matters at all stages of this work were crucial to its progress and are greatly appreciated.

I am highly appreciate the kind helps from Dr. Andreas Klehr for his daily guidance in experiments and the fruitful discussion.

I am highly appreciate many valuable discussion and his thoughtful guidance to Prof. Dr. Michael Kneissl.

My thanks also go to Prof. Dr. Martin Hofmann for having accepted to as an appraiser of the Ph.D. thesis.

My warm thanks go to my colleagues in Laser Sensors Lab Group (Maiwald Martin, Müller Andre, Ruhnke Norman, Braune Marcel, Tawfieq Mahmoud, Kabitzke Julia and Zink Christof) for daily help, collaboration and discussion.

The experiment part of my PhD work has an important contribution of Krichler Maria for programming support and Dr. Bernd Eppich for spatial characterization and propagation simulation of laser beams. I highly appreciate their assistance.

I am indebted to Dr. Hans Wenzel, Dr. Gunnar Blume, Dr. Olaf Brox, Dr. Jörg Fricke for their support in discussion about the devices, correction of my thesis.

I would like to thank Dr. Armin Liero, Thomas Hoffmann for electrical circuit discussions, especially with regard to ns-pulse electric circuits used in the frame of this work.

I am grateful to all colleagues at Ferdinand-Braun-Institut, who have contributed to the design, epitaxy, coating and mounting of diode lasers

applied in this work. In particular, I wish to thank Mr. Arnim Ginolas for fruitful discussions on the structures of mounted devices. I highly appreciate their assistance.

During my working time in laboratory, I got very kind help and sharing opinions as well as emotion everyday from Jacqueline Hopp, and also lot of good technical supports from Heidemann Jörg, and helpful discussions from my colleagues in the department, who are very kind with me, so I would like to thank them for everything.

In FBH, I already enjoyed a very nice environment with German colleagues, Marlies Gielow and the colleagues come from many countries, many thanks to them.

Needless to say, I got continuously support from Institute of Materials Science (IMS), Vietnam Academy of Science and Technology ($VAST$). I thank the Director of (IMS) Prof. Dr. Sc. Nguyen Quang Liem. Many thanks go to the head of our group Semiconductor lasers Laboratory Dr. Tran Quoc Tien and other colleagues in IMS, $VAST$, who indirectly contribute to the success in my PhD works.

The PhD course belongs to the Training Scientific and Technical Cadres in Institutions overseas with the State Budget (Project 322) and Deutscher Akademischer Austausch Dienst (DAAD) (A/10/76664). I would like to thank the funding from Vietnamese government.

Last but not least, I thank all people in my 'big family' for their supports and encouragement continuously. Final thanks, I reserve them to my 'small family' to my beloved, who always see the same way with me; to my children, who made me smile after working time.

1 Introduction

Aerosols and water vapor are extremely important for the weather forecast and climate studies to predict dangerous situations. Aerosols are suspended particles for example sea-salts, mineral dust, organic matter and smoke. They enter the atmosphere from a variety of natural and anthropological sources and play an important role in countering global warming effects by reflecting incoming solar radiation and by influencing the hydro-logical cycle. Hence, aerosols play an important role in the complex climate system of the earth [1–3]. Water vapor is one of the most important atmosphere constitutes. It governs the atmosphere water cycle, which is the basic for life on earth and plays a crucial role in both radiation and convective energy transfer through the atmosphere [4–7]. Water vapor is a key gas with extreme and rapid variability, which is related to various atmosphere effects. Water is transported into the atmosphere via evaporation where the rate depends on the ocean and air temperature [8].

Accurate measurement of aerosols and water vapor in the atmosphere is necessary to understand its behavior. It is a key information for both the weather forecast and climate research. The main challenge of aerosols and water vapor detection is the variability of its prevalence [1–7]. It is essential to understand their spatial and temporal variability in relation to various atmospheric effects.

The concept of Light Detection and Ranging ($LIDAR$) systems was first introduced in the early 1960s after the invention of the laser [9]. The $LIDAR$ systems allow measuring the distribution of specific trace gas species in the atmosphere with a good accuracy and a sufficient spatial resolution [10, 11]. $LIDAR$ is a powerful tool for enhancing the knowledge and understanding of a wide variety of environmental phenomena which relate to the atmosphere, oceans, land surface, ice cover and finally to life [11]. It uses light in form of a pulsed laser which is transmitted through the atmosphere. Where it hits an object and scatters. A portion is scattered back to a detector system. Based on the arrival time of the backscattered, a spatial resolved distribution of particles, aerosols and molecules can be determined [12–14].

Differential absorption $LIDAR$ ($DIAL$) is a developed technique that operates at two wavelengths, one on resonance and one off resonance of the water vapor absorption line. The on resonance wavelength is more strongly absorbed than the off resonance wavelength. The difference between both back scattering signals is proportional to concentration of the water vapor [15–25]. Thus, the quantity of water vapor at a particular pinpointed location can be inferred.

Conventional $LIDAR$ systems use very high power (MW-peak power), ns pulse length, mJ peak energy at low repetition rates in the Hz-range. Solid state lasers such as Ti:Sapphire lasers [13, 14], Alexandrite lasers [15], optical parametric oscillators (OPO) [16], $Cr : LiSAF$ lasers [17, 18], and $Nd : YAG$ lasers [19, 20] were used. These lasers provide high pulse energies to achieve the necessary spatial and temporal resolution. Although yielding high pulse energy, the practical use of solid state lasers is not widely implemented in $LIDAR$ systems that require deployment in standalone network configurations. Due to the high maintenance cost, the replacement of pump sources and gain medium, the low electro-optical and optical-optical efficiencies, the large optical footprints and large nominal ocular hazard distances are detrimental [26].

An alternative approach known as the Micro Pulse $Lidar$ (MPL) system was used [27–29]. The first MPL was developed by $NASA's$ Goddard Space Flight Centre in 1993. In MPL systems, the repetition rates (f) are increased to approximately some 10 kHz and the pulse length (τ) shortened to a few μs. The large signal-to-noise ratio can be achieved by summing over millions of pulses in fairly short time intervals of several minutes. This allows to reduce the pulse energies to the μJ ranges. The low pulse energy is an important factor for eye-safety systems. A diode pumped $Nd : YAG$ laser was used because of the availability and their suited properties.

Recent progress in diode laser technology allowed an improvement of the vertical layer structures by the introduction of super large optical cavities and herewith reduction of the facet load. The development of a highly reliable mirror technology by applying cleaning and passivation techniques and the use of highly reliable mirror coating are demonstrated. An all diode laser system becomes feasible to reach a

peak power above 10 W [27, 30–33]. Master oscillator power amplifier ($MOPA$) systems in which a distributed Bragg reflector (DBR) laser, a distributed feedback (DFB) laser, or an external cavity diode laser ($ECDL$) acts as master oscillator (MO) and a tapered amplifier acts as power amplifier (PA). The MO offers a stabilized wavelength and a small spectral line width whereas the PA provides a high output power.

The $MOPA$ systems have the capability to reach a peak power in the range of 10 W and the output energy in the μJ range. A $MOPA$ is powerful enough to be used as an all semiconductor laser transmitter in $LIDAR$ or $DIAL$ for aerosols and water vapor detection. They are not only compact, inexpensive, highly efficient, mechanically stable, but also feature widely varied wavelengths. This allows to select a precise wavelength at absorption lines for each molecular atmospheric composition to achieve an optimal efficient detection. This thesis demonstrates all-diode lasers based $MOPA$ systems. The developed systems show the potentially applicable in $LIDAR$ or $DIAL$ systems for aerosols and water vapor detection and allow ultra-compact, low cost systems and can be known as Micro Pulse Lidar systems ($MPLs$).

This work is organized as follows:

- The second chapter discusses the principles of operating $LIDAR$ systems as well as gaining understanding of the requirements of the laser transmitters for $LIDAR$ systems. Then the specifications of the light source for elastic-backscatter $LIDAR$ system for aerosols are derived. For more accuracy and higher resolution, e.g, water vapor profiling, the differential absorption $LIDAR$ ($DIAL$) is introduced. Success in $MPLs$ development is strongly connected with particular laser technology. A certain $MPLs$ technique needs specifically designed laser transmissions. For this reason, specific parameters of the laser systems in this work will be discussed. Then the status of the diode laser based $MOPA$ systems as laser transmitters for aerosols and water vapor will be shown.
- The third chapter will present the approaches of the $MOPA$ concepts. A short description of the fabrication of the monolithic $MOPA$ and the individual devices of hybrid $MOPA$ systems used in this work will be given.

- For characterization of diode lasers and $MOPA$ systems, the experimental setups are comprised in chapter four. Basic characterization such as electro-optical characterization, spectral properties under continuous wave mode and under the ns-pulse excitation are shown. A description of the electrical circuit for high currents and short pulses will be discussed.

- Chapter five goes into details of the experimental results of the wavelength stabilized diode laser based $ns-MOPA$ systems. Two concepts of monolithic and hybrid $MOPA$ systems operation at 1064 nm are investigated. One is a monolithic $MOPA$ and another is a hybrid $MOPA$ system. The monolithic $MOPA$ is a compact approach with integrated MO and PA on a single chip. The hybrid $MOPA$ system consists of a DFB laser and a multi-section amplifier. Based on specification of two concepts further investigation is oriented. The hybrid $MOPA$ system is suitable for atmospheric gases as well as for aerosols measurement whereas the monolithic $MOPA$ is sufficient only for aerosols.

- For concentration calibration, adjustment of the working points and the selection of suitable absorption lines, the laser transmitters need not only to be stable at a specific wavelength but also must be tuned continuously to scan over more than one absorption line. Chapter six presents a tunable wavelength hybrid $MOPA$ system. It operates at wavelengths of around 975 nm where one potential spectral region for water vapor detection is located. The behavior of the output power on the input power as well as saturated operation of the system will be discussed. The delay time between the optical gate and tapered section targeting of a small of amount of amplified spontaneous emission is investigated. Then the spectral tuning range of 0.9 nm will be shown. It is possible to scan over several absorption lines of water vapor.

- Chapter seven describes an investigation of a $MOPA$ system operation at two wavelengths for an application in differential absorption $LIDAR$ ($DIAL$) systems. The $MOPA$ uses a dual wavelength $Y-branch-DFB$ laser and a multi-section tapered amplifier.

It features two wavelengths at around of 964 nm. By changing the temperatures and currents of the $Y-branch-DFB$ the tuning of two wavelengths is achieved. Two pair wavelengths for on-off lines with different absorption coefficients of water vapor are selected. The peak power, spectral line widths and $SMSR$ at each wavelength are given.

- Finally, summary and outlines of future areas of interest for the extension of the ideas developed in this work will be shown in chapter eight.

2 Basic principle of LIDAR and DIAL systems-light sources for LIDAR and DIAL

2.1 Basic principle of LIDAR system and basic equation

In order to understand the needs of the *MOPA* light sources in the *LIDAR* or *DIAL* systems, a short overview of the operation principle of the *LIDAR* system is given in this part. The *LIDAR* equation is introduced to analyze the contribution of each parameter of the laser transmitter in such a system.

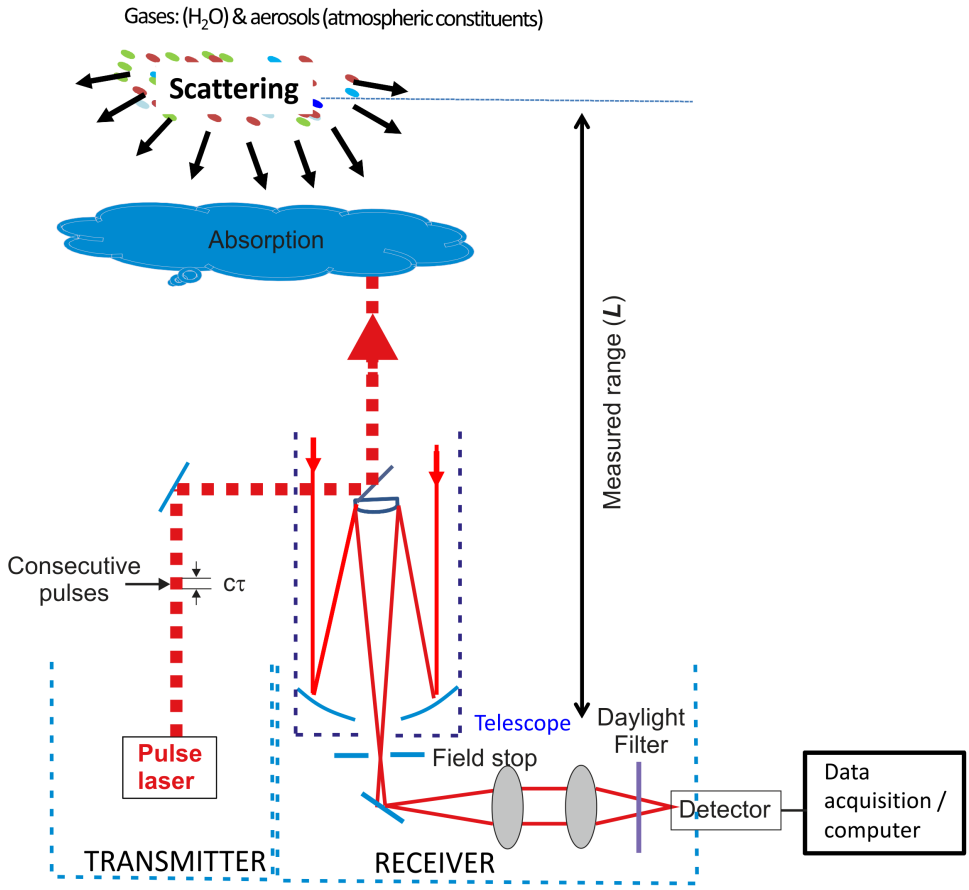

Figure 2.1: Schematic diagram of LIDAR system block diagram.

A principle scheme of the *LIDAR* is given in Fig 2.1. In the simplest term, it consists of a transmitter and a receiver. Short laser pulses with lengths of few to several hundreds of nanoseconds and specific spectral

properties are generated by a laser. The collimated light beam is sent into the atmosphere. It can be absorbed and scattered by atmospheric constituents. At the receiver, a telescope collects the photons backscattered from the atmosphere then passes through a field stop placed at the focus plane of the telescope. The field stop limits the field of view such that returns from multiple scattering events and stray background light are prevented before reaching the detector. A narrow optical filter placed in front of the detector is to ensure that only the backscattered light from the laser transmitter is measured by the detector. The duration time of each scattering event from a single laser pulse is proportional to the distance to the scattering volume along the entire illuminated path. The signal processing and data acquisition are analyzed to inform the characterization of the extent and properties of aerosols, gases such as water vapor or other particles based on the real-time detection and post-processing of the signal return.

The received power $P(\lambda, R)$ from a distance R at a wavelength λ can be calculated by the $LIDAR$ equation, written in ref.[34] for a single scatter, monochromatic elastic $LIDAR$ with the simplest form as

$$P(\lambda, R) = K(\lambda, R)G(R)\beta(\lambda, R)T(\lambda, R). \tag{2.1}$$

It can be seen that the received power $P(\lambda, R)$ includes four factors. Going into more detail for each factor, the first factor in equation (2.1) $K(\lambda, R)$ represents the system factor and can be written as

$$K(\lambda, R) = P_0(\lambda)\frac{c\tau}{2}A\eta \tag{2.2}$$

where $P_0(\lambda)$ is the average power of a single laser pulse and τ [s] is the optical pulse width and $c\tau$ is the length of the laser pulse at a fixed time. The factor $1/2$ appears because the laser pulse has to travel forward and backward. A is the area of the primary receiver optics responsible for collection of backscattered light, and η is the overall system efficiency. It includes the optical efficiency of all elements such as the transmitter, receiver and the detection efficiency. It can be optimized for the best possible signal. The telescope area A $[m^2]$ and the average laser power $P_{avg}[W] = {}^{P_p * \tau}/_{T}$ (with P_p is peak power, τ is pulse width and T is the period of time, in inverse to the pulse repetition rate frequency f_{rep} [Hz]) are primary design parameters of a $LIDAR$ system.

The second factor in equation (2.1) $G(R)$ is a geometric factor, the ratio of the laser beam receiver-field-of-view overlap and the term R^2 and written as

$$G(R) = \frac{O(R)}{R^2} \tag{2.3}$$

The laser beam receive-field-of-view is the receiver telescope area or the entrance area of the telescope receiver. The quadratic reduction of the signal intensity with the distance (R[m]) is due to the fact that the receiver telescope area makes up a part of a sphere's surface with radius R that encloses the scattering volume. This leads to a strong influence on the received intensity. For example, a detected signal at 10 m with $O(R) = O(10) = 1$ will be 6 orders of magnitude lower at 10 km.

Both the first and second factors in equation 2.1 are completely determined by $LIDAR$ setup.

The third factor in equation (2.1) $\beta(\lambda, R)$ is the backscatter coefficient at the distance R. It is the subject of investigation, the primary atmospheric parameter that determines the strength of the $LIDAR$ signal and ascertains how much light is scattered into the backward direction, i.e towards the $LIDAR$ receiver. The backscatter coefficient is a specific value for the scattering angle of $\theta = 180^0$. If N_j is the concentration of scattering particles of kind j in the length of the laser duration pulse and the particles' differential scattering cross section for the backward direction at the wavelength λ is $\frac{d\sigma_{j,sca}(\pi,\lambda)}{d\Omega}$. The backscatter coefficient can be written as a sum of all kinds of scatters,

$$\beta(\lambda, R) = \sum\nolimits_j N_j(R) \frac{d\sigma_{j,sca}(\pi, \lambda)}{d\Omega}. \tag{2.4}$$

N_j is given in units of $[m^{-3}]$ and differential scattering cross section ($\frac{d\sigma_{j,sca}(\pi,\lambda)}{d\Omega}$) in $[m^2 sr^{-1}]$, the backscatter coefficient ($\beta(\lambda, R)$) has the unit $[m^{-1} sr^{-1}]$.

In the atmosphere, the laser light is scattered by air molecules and aerosols. It can be expressed as $\beta(\lambda, R) = \beta_m(\lambda, R) + \beta_a(\lambda, R)$ where β_m and β_a are the molecular and aerosol backscatter coefficients, respectively.

The final factor in equation (2.1) $T(\lambda, R)$ is the transmission term. It describes how much light gets lost on the way from the laser transmitter

to the distance R and back. It is the subject for studying. It results from the specific form of the Lambert-Beer's law for $LIDAR$. Thus it can be values between 0 to 1 and given by

$$T(\lambda, R) = \exp\{-2 \int_0^R \alpha(\lambda, r)\mathrm{d}r\}. \tag{2.5}$$

The integral considers the path from the $LIDAR$ to the distance R. The factor 2 is due to two-way transmission path. The $\alpha(\lambda, r)[m^{-1}]$ is the extinction coefficient and is the product of number concentration $N_j(r)[m^3]$ and extinction cross section $\sigma_{j,ext}$ for each type of scatter j,

$$\alpha(\lambda, r) = \sum\nolimits_j N_j(r)\sigma_{j,ext}(\lambda) \tag{2.6}$$

extinction is caused by both scattering and absorption of light and both by molecules and particles. The total extinction coefficient $\sigma_t(\lambda, r)[m^{-1}]$ thus includes molecular scattering and aerosol scattering, molecular and aerosols absorption. It can be expressed as

$$\alpha_t(\lambda, r) = \alpha_{m,sca}(\lambda, r) + \alpha_{a,sca}(\lambda, r) + \alpha_{m,abs}(\lambda, r) + \sigma_{a,abs}(\lambda, r) \tag{2.7}$$

The subscripts m and a stand for molecular and aerosol, sca and abs for scattering and absorption respectively. Due to scattering into all directions, the general extinction cross section is caused by the scattering cross section σ_{sca}, $[m^2]$ and the absorption cross section σ_{abs}, $[m^2]$. It can be written as

$$\sigma_{ext}(\lambda) = \sigma_{sca}(\lambda) + \sigma_{abs}(\lambda). \tag{2.8}$$

Finally, summarizing all the individual terms, the $LIDAR$ equation can be rewritten as

$$P(\lambda, R) = P_0 A\eta(\lambda)(\frac{c\tau}{2})\{\frac{O(R)}{R^2}\}\beta(\lambda, R)\exp\{-2 \int_0^R \alpha(\lambda, r)\mathrm{d}r\}. \tag{2.9}$$

Equation 2.9 is a common equation form of the $LIDAR$ system. Depending on interaction processes of the laser transmitter with the atmospheric constituents, $LIDAR$ systems can be classified into five different systems based on the specifically physical phenomenons such as elastic-backscatter, differential absorption, Raman, resonance fluorescence and

Doppler. The $LIDAR$ equation of each kind of $LIDAR$ therefore is also developed based on each physical interaction.

In this work, diode laser based $MOPA$ concepts suitable for elastic-backscatter and differential $LIDAR$ systems for aerosols and water vapor detection are demonstrated. In the following, a further discussion about these systems is given.

Elastic-backscatter $LIDAR$ is developed based on elastic scattering in which the wavelength is conserved with incident wavelength but its direction is modified. It provides information of the presence and location of aerosols and cloud layers. The system uses one laser emitting a single wavelength and one detector measuring the radiation elastically backscattered from the atmospheric molecules and particles. Depending on the size of the particles, elastic backscatting $LIDAR$ can be a *Rayleigh* or a *Mie* $LIDAR$. *Rayleigh* scattering can be defined as the elastic scattering from particles that are very small compared to the wavelength of the radiation (laser transmitter). Its scattering intensity is proportional to λ^{-4}.

In case of particles with sizes comparable to the wavelength of the radiation or larger, *Mie* scattering dominates. It is not limited to a certain size of the scatters. The scattered intensity is a function of particle radius relative to wavelength and the particles complex refractive index. Scattering from very large particles does not depend on the wavelength.

Because of the different shapes of particles in the atmosphere, *Mie* scattering theory is applied for providing a very rough approximation. Since the particles are small compared to the wavelength, the actual shape does not play a major role for the scattering properties as theories for not-spherical scatters show [35].

In general, both Rayleigh-Mie $LIDARs$ measure the total atmosphere backscatter without separation of particle and molecular contribution. They provide a rough profile of the climate relevant volume extinction coefficient of the particles.

The requirement of light source for these systems therefore is effortless to the spectral line width. The intensity of the backscattered signal is of interest, so that a laser with a broad spectral line width can be used. However, to suppress the sunlight background of the daytime operation,

Table 2.1.1: Parameters of light sources for elastic-backscatter $LIDAR$ system for aerosols detection

Peak power: P_p	$>$ 10 W
Pulse width: τ	$<$ 10 ns
Repetition rate: f	$>$ 20 kHz
Spectral linewidth: $\Delta\lambda$	$<$ 300 pm
Wavelength: λ	1064 nm
ASE:	$<$ 10%

a filter of 300 pm is often used. Thus, a spectral line width of about 300 pm should be sufficient. The light sources with a high peak power to achieve a large signal-to-noise ratio are to be expected. In this work, a peak power of above 10 W with a repetition rate more than 20 kHz to achieve more photons backscatted to receiver are applied. A short pulse width provides a high resolution of the system. A single wavelength with certain wavelength to avoid uncertain in the laser line position which causes errors in measurement. A small amount of amplified spontaneous emission (ASE) provides a spectral purity which needs to prevent errors in measurement. These parameters are given in the table 2.1.1.

In order to provide accuracy and high resolution, e.g, water vapor profiling, the differential absorption $LIDAR$ or $DIAL$ is introduced.

2.2 Differential absorption LIDAR (DIAL) for gas measurements, e.g., water vapor profiling

Differential absorption $LIDAR$ ($DIAL$) technique uses two different wavelengths, one of which is absorbed more strongly than the other. The differential molecular absorption coefficient $\Delta\alpha_{mol,abs}$ can be determined, if the differential absorption cross section $\Delta\sigma_{mol,abs}$ for the two wavelengths is known. The number concentration of the gas atoms or molecules can be determined.

When two wavelengths are very close to each other in the spectral

regions where any absorption by gases in the atmosphere is negligible except for water vapor absorption. Going into the elastic back scatter $LIDAR$ equation 2.9 as mention above, the factors such as system (K), geometric (G), backscatter coefficient (β) are equivalent for two wavelengths. Only the transmission term (T) factor is effected by wavelengths which is caused only by water vapor and induced by the Lambert-Beer's law. In the idealized case, the $LIDAR$ signal back scattering intensities are described as

$$P(\lambda, R) = P_0 A \eta (\frac{c\tau}{2}) \{\frac{O(R)}{R^2}\} \beta(R) \exp\{-2 \int_0^r \alpha(\lambda, r) \mathrm{d}r\}. \quad (2.10)$$

Therefore, the received power $P(\lambda, r)$ from range r at the wavelength (λ) is dependent on the wavelength, only by water vapor.

Applying for two wavelengths λ_{on} and λ_{off}, corresponding to larger and smaller absorption cross sections, then it is divided between each other and can be written

$$\frac{P(\lambda_{on}, r)}{P(\lambda_{off}, r)} = \frac{\exp\{-2 \int_0^r \alpha(\lambda_{on}, r) \mathrm{d}r\}}{\exp\{-2 \int_0^r \alpha(\lambda_{off}, r) \mathrm{d}r\}} \quad (2.11)$$

In the simplest form, it is set as:

$$\begin{aligned} P(\lambda_{on}, r) = P_{on}(r),\ P(\lambda_{off}, r) = P_{off}(r), \\ \alpha(\lambda_{on}, r) = \alpha_{on}(r),\ \alpha(\lambda_{off}, r) = \alpha_{off}(r) \end{aligned} \quad (2.12)$$

The water vapor extinction coefficient is product of water vapor number density N_{WV} and the absorption cross section σ_{WV}. It is written as

$$\alpha_{WV} = \sigma_{WV}\ N_{WV} \quad (2.13)$$

And it can be set,

$$\alpha_{on} = \sigma_{on}\ N_{WV},\ \alpha_{off} = \sigma_{off}\ N_{WV} \quad (2.14)$$

Replaying the equations (2.12- 2.14) into the equation 2.11 and differentiating both sides of the equation, they can be written as

$$\ln\{\frac{P_{on}(r)}{P_{off}(r)}\} = \frac{\{-2 \int_0^r \sigma_{on}\ N_{WV} \mathrm{d}r\}}{\{-2 \int_0^r \sigma_{on}\ N_{WV} \mathrm{d}r\}} \quad (2.15)$$

The differential between the two spectral separated $LIDAR$ returns over an adjacent range, $dr = {}^{c\tau}/_{2}$, can be written as

$$\{\ln(P_{on}, r) - \ln(P_{on}, r+dr)\} - \{\ln(P_{off}, r)) - \ln(P_{off}, r+dr)\} = 2\int_{r}^{r+dr} \sigma_{on}\ N_{WV}\mathrm{d}r' - 2\int_{r}^{r+dr} \sigma_{off}\ N_{WV}\mathrm{d}r' \tag{2.16}$$

The molecular concentration in the Lambert-Beer's law relationship is also assumed to be a constant over a singe range dr, allowing the integral in equation 2.16 to be simplified as

$$\begin{aligned} 2\int_{r}^{r+dr} \sigma_{on}\ N_{WV}\mathrm{d}r' &= 2\sigma_{on}\ N_{WV}(r+\mathrm{d}r)\ dr \\ 2\int_{r}^{r+dr} \sigma_{off}\ N_{WV}\mathrm{d}r' &= 2\sigma_{off}\ N_{WV}(r+\mathrm{d}r)\ dr \end{aligned} \tag{2.17}$$

After algebraic manipulation the water vapor concentration can be written

$$N_{WV}(r+dr) = \frac{1}{2\ \sigma_{eff}(r)\ dr} \ln\{\frac{P_{on}(r)}{P_{on}(r+dr)}\ \frac{P_{off}(r+dr)}{P_{off}(r)}\} \tag{2.18}$$

where $\sigma_{eff}(r) = \sigma_{on}(r) - \sigma_{off}(r)$ is the effective cross section. The $dr = {}^{c\tau}/_{2}$ is the range size, $P_{on}(r)$, $P_{on}(r+dr)$, $P_{off}(r)$ and $P_{off}(r+dr)$ are the intensities coming back to receiver at the wavelengths online and offline at the range of r and $r+dr$, respectively. More details can be read in [35–37].

In practice, the $DIAL$ equation 2.18 is used to calculate the water vapor concentration. It is realized by forming the ratio with the above assumptions. Taken into account to achieve a accuracy measurement, the errors caused by detectors, atmospheric effects and laser transmitters should be minimized.

For detectors as background signal noise from solar radiation, the detector dark current and amplifier noise should be considered [38].

For atmospheric effects and laser transmitters, the main atmospheric effects include temperature sensitivities, pressure broadening and pressure shifts of the H_2O absorption lines, and Doppler broadening of the Rayleigh backscattered component in the $LIDAR$ return [36–42].

Table 2.2.1: Parameters of light sources for *DIAL* for water vapor concentration detection in the lower troposphere in this work

Peak power: P_p	$>$ 10 W
Pulse width: τ	8 ns
Repetition rate: f	25 kHz
Spectral linewidth: $\Delta\lambda$	$<$ 10 pm
Wavelength: λ	975 nm, tunable
Wavelength: λ	965 nm, dual
ASE:	$<$ 1%

Thus laser transmitters for water vapor concentration should be chosen an appropriate absorption line strength for minimizing the absorption cross-section sensitivity to temperature, pressure broadening, etc, as well as isolated from other nearby absorption lines. The line width of light source smaller than spectral line width of the absorption line is requested. The spectral purity and a certain wavelength are also needed to limit the error in measurement.

Success in MPL system development is strongly connected with optical and electronic technology, in particular laser technology [35]. To meet the requirements of a certain MPL system, specifically designed lasers for laser power, pulse width, repetition rate, wavelengths, spectral line width and spectral purity are needed.

In this target, the main parameters of the laser systems are shown in table 2.2.1. A peak power more than 10 W with a high repetition rate provides a high photons backscatted to receiver. A spectral linewidth is smaller than the absorption line of the water vapor at the 975 nm region at the normal atmosphere. A short pulse width (8 ns) provides a high resolution of the system (1.2 m). A tunable wavelength to scan over several absorption lines of the water vapor for concentration calibration and selection the working points or a dual wavelength to switch on and off absorption line can be expected. A small amount of amplified spontaneous emission provides a spectral purity which needs to prevent errors in measurement.

More details of these parameters of light sources in the $MPLs$ systems, an analysis of each parameter is given in the following section.

2.3 Specific requirements of laser systems for LIDAR and DIAL

Going into detail of the contribution of each parameter of the light source of the $MPLs$ the specific parameters of diode laser based $MOPA$ systems in this work are clarified as following.

The first parameter is the peak power. A high value is desired for many applications. A peak power higher than 10 W is the target. For high energy of light sources is needed for $LIDAR$ systems, one can be used by high peak powers and low repetition rates and another can be applied by low peak powers with high repetition rates. In the case of repetition rates of 10 kHz, peak powers in the range between 2 W and 10 W with a pulse width of 1 μs were performed [22–26]. The water vapor profiling in the range of 7 km and a resolution of 150 m were reported in the measured time of about 10 minutes. Comparable with our systems, a peak power of more than 10 W at higher repetition rates (25 kHz) at the pulse width of 8 ns should be sufficient to provide a high backscattering signal. A shorter pulse width should provide a higher spatial resolution of the $LIDAR$ systems, and a higher repetition rate can be reduced the measurement time.

The second and third parameters are the pulse width and the repetition rate. The pulse width of the light sources determines the achievable spatial resolution in such systems whereas the repetition rate determines the possible measured range of the system [12, 28, 29, 43]. The explicit dependence of the resolution (ΔL) and measured range (L) on the pulse width and repetition rate of laser pulses, an example of two consecutive laser pulses is sketched in Fig. 2.2. The relevant return signals as well as the resolved-time interval are detected in the receiver. They are expressed on the time scale axis (t) and the distance scale axis (L) respectively. The symbols used to express the parameters are as follow: the pulse width (τ), the repetition rate (f), the measured range (L) and the resolution (ΔL).

The measured range L is determined by comparing the time elapsed

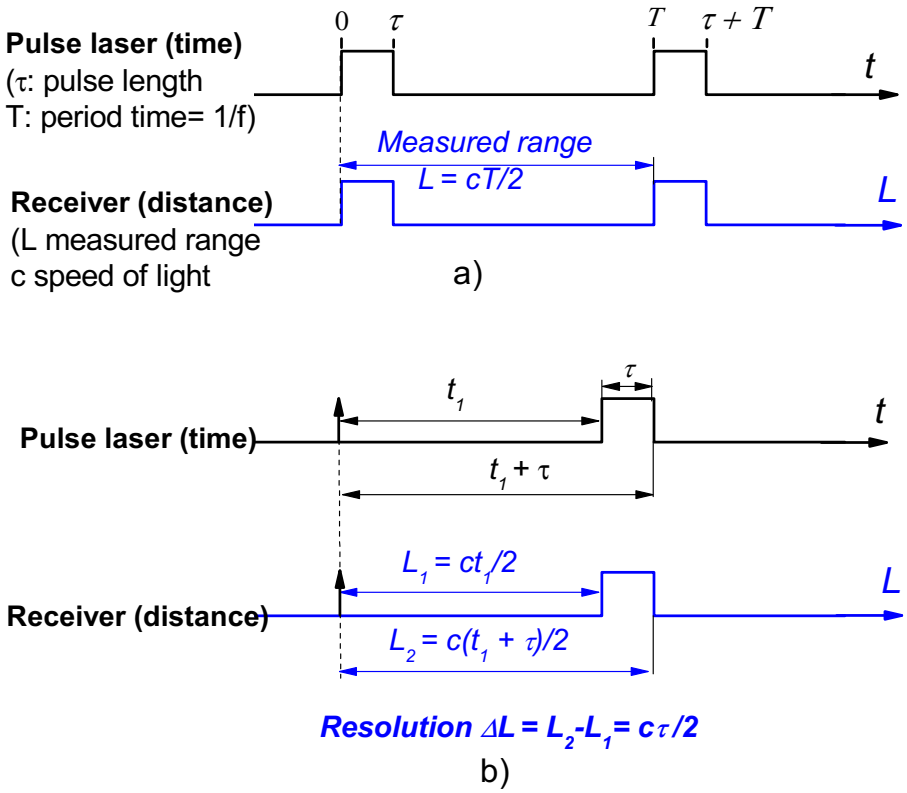

Figure 2.2: Schematic diagram of two consecutive laser pulses and relevant receiver for calculation the distance (a) and resolution (b) of the LIDAR system .

between the transmitted laser pulse and the return pulse T (corresponding to a repetition rate $f = 1/T$). It is calculated by $L = cT/2$. It is a product of the speed of the light (c) and the factor $1/2$ as the light has to travel forward and backward. A repetition rate between 1 MHz and 25 kHz, corresponding to the periods of time of 1 μs and 40 μs, is needed for a measured range between 330 m and 6000 m, respectively.

The resolution is estimated by the analog recording of the backscattered light. It depends on the pulse width τ according to $\Delta L = c\tau/2$ with c speed of light. At a certain measurement time t_1 signals from the leading edge of the pulse arrive at the detector from the position $L_1 = 1/2ct_1$ and from training edge is $L_2 = 1/2c(t_1 + \tau)$. The resolution (the difference of leading and training edge positions) is determined by $\Delta L = L_2 - L_1 = c\tau/2$. Thus, in order to obtain a resolution in the range from 0.3 m to 1.2 m, pulse widths between 2 ns and 8 ns are needed.

The fourth parameter is related to the backscattered signal intensity. The stronger the absorption line is, the lower is the scattering signal that returns back. Such a line should be applied for a short measured range or a low concentration. And vice versa, the weaker the absorption line is, the higher is the scattering signal that returns back. This line should be applied for a long measured range and a high concentration. In the case of water vapor absorption lines detection, usually absorption lines in the near infrared region or visible range are preferred. The shorter wavelengths (visible) increase the backscattering coefficient and the near infrared region allow the use of high conversion efficiency of semiconductor lasers as well as high sensitive silicon based photo detectors. Therefore it is chosen in this work.

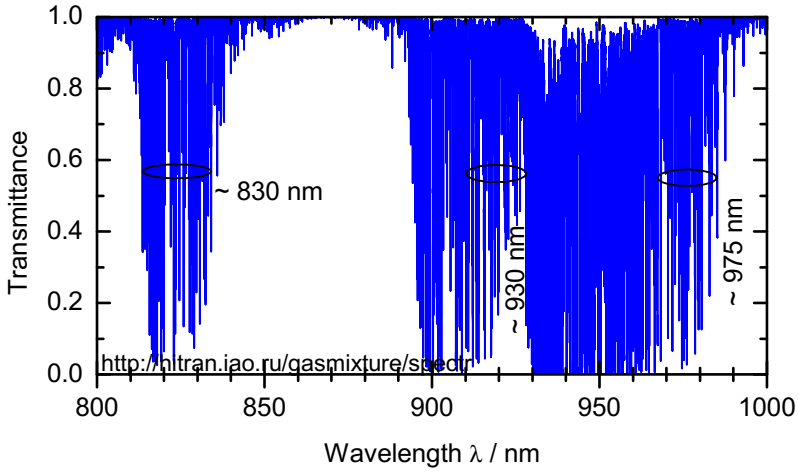

Figure 2.3: Transmission spectrum for water vapor in the near infrared based on the *HITRAN* data compilation [43] for a path length of 500 m at a temperature of 296 K and a total pressure of 1 atm (25% relative humidity).

To select a proper region the simulation was performed based on Hitran database [43]. A spectrum of water vapor in the near infrared spectral range from 800 nm to 1000 nm is plotted in Fig. 2.3. Here a path length of 500 m at a temperature of 296 K and a total pressure of 1 atm (25% relative humidity, partial pressure of the water vapor P_{H2O} of 0.0069 atm) are used. It is remarked at three regions at 830 nm, 930 nm and 975 nm where locates the potential regions for water vapor

absorption lines detection. It is obvious that the transmission values of about 50% are obtained in the spectral region of 830 nm which was used for the water vapor measurement referred in refs [22–26]. Comparable absorption would be in the region around 935 nm as used by Fix *et al.* [44] or in the region around 975 nm. An advantageous property of the spectral region at 975 nm are the high efficient conversion of $GaAs$-based high power diode and the availability of the diode lasers and the power amplifiers as well as the detectors.

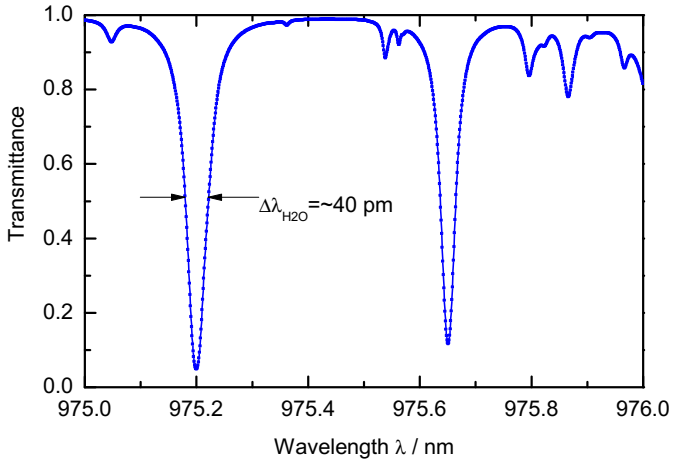

Figure 2.4: High resolution of transmission spectrum for water vapor in the range between of 975 nm and 976 nm zoomed in from Fig. 2.3.

The fifth parameter deals with the spectral line width. To minimize spectral distortion of the shape and width of the water vapor absorption lines, the laser spectral line width must be no larger than one-quarter of the water vapor line width [45–47]. A spectrum of water vapor in the range between of 975 nm and 976 nm is compiled by $HITRAN$ [43] and given in Fig. 2.4. Here the same conditions as in Fig. 2.3 are used. It can be seen that at the wavelength of 975.20 nm, the full width at half maximum of the spectral line width is about 40 pm. A one-quarter spectral line width therefore is about 10 pm. Thus, a spectral line width smaller than 10 pm should be sufficient.

The final consideration is the amplified spontaneous emission (ASE). An example spectrum including laser and ASE is given in Fig. 2.5.

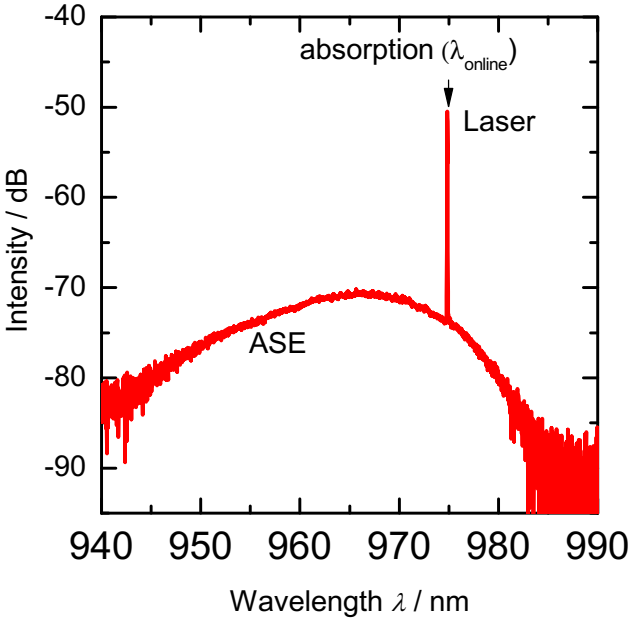

Figure 2.5: An example of a broad emission spectrum consisting ASE and lasing emission.

The ASE covers a wide spectral range outside of absorption line of the water vapor and is non-absorbed by H_2O. Thus, their back scattering signals are similar to the off-line absorption lines. In $LIDAR$ or $DIAL$ application, the H_2O concentration is retrieved by using the differential absorption cross section between the on and off wavelengths, whereas the online laser energy is assumed to be absorbed by H_2O molecules and the offline laser energy is transmitted. It causes an error in the measurement that changes with distance and cannot be corrected [35, 48–50].

To estimate the error caused by the ASE, it can be assumed that fraction P_{ASE} is the total transmitted energy that is outside a well-defined laser line. Since this portion of the transmitted light passes the atmosphere with no absorption, its contribution to the backscatter for online wavelength will increase with optical thickness (τ_0). The relative error in the retrieved absorption coefficient is then [34]

$$\frac{\Delta\alpha}{\alpha} = \frac{P_{ASE}}{P_{ASE} + (1 - P_{ASE})e^{-\tau_0}} \tag{2.19}$$

In [38], the influence of spectral purity, the ratio of the energy within the acceptable spectral limits to the total energy transmitted (caused by ASE) on H_2O in $DIAL$ measurements was simulated. The number density errors increased from 1% up to 15% when the spectral purity of the laser reduces from 0.05% to 5%. It was reported that for most $DIAL$ applications, lasers with the spectral purity better than 0.99%, the amount of ASE smaller than 1% are necessary. Therefore, the final parameter is considered to reduce the amount of ASE down to below 1%.

Briefly, the goal of this work is to realize all diode laser based $MOPA$ systems that meet all above-mentioned parameters for both aerosols and water vapor detection.

2.4 Current status of diode laser based MOPA systems as laser transmitters for aerosols and water vapor

In the above sections, the motivation for the research in framework of this thesis is carried out. The specific parameters concerning the laser systems were defined. Now, a short overview of the recent investigations of all-semiconductor diode lasers based $MOPA$ systems as laser transmitters for water vapor and aerosols detection is given.

The laser transmitters based $MOPA$ systems based diode lasers for water vapor and aerosols detection were introduced in 1996 by Reagen *et al.* [51]. The simulated results were given in daytime measurement with an averaged time over 15 minutes for 5 μJ of laser energy for the on/off line wavelength at wavelength of 830 nm, a 10 kHz repetition rate and 1 μs pulse width. A relatively clear aerosol profile with back scatter at a height of 3 km at the standard atmosphere (T= 296K, p= 1 atm) [52] was shown. At nighttime, a better signal up to 5 km was observed. These results suggested that all diode laser based $MOPA$ systems should be suitable for aerosols and water vapor sensing.

Up to now numerous studies of the diode laser based $MOPA$ systems as light sources for the water vapor absorption lines and aerosols have been performed. They are listed in following table.

Machol *et al.* [22] used a DFB laser operating at 823 nm as seed

Table 2.4.1: Recent literature of the experimental $MOPA$ systems as laser transmitters in $MPLs$ for water vapor and aerosols profiles in the atmosphere (The white and blue colors are remarked as external and internal references)(Refs: references, P_P: peak power, PG: pulse generation, τ: pulse width, f: repetition rate,λ: wavelength, $\delta\lambda$: Spectral line width, $\Delta\lambda$: tuning range, ASE: amplified spontaneous emission, TPA: tapered power amplifier, ECDL: external cavity diode laser, DM: direct modulation.)

Refs	MO	PA	P_P[W]	PG	τ [ns]	f [kHz]	λ [nm]	$\delta\lambda$ [pm]	$\Delta\lambda$[nm]	ASE [%]
[22]	DFB	TPA	0.5	DM	600	6-10	823	0.03		
[53]	ECDL	2 TPA	0.5	DM	500	0.5	830	0.001	17	
[25, 54]	ECDL	2 TPA	0.5	DM	1000	20	830	0.001	17	
[23, 24]	ECDL	2TPA	2	DM	1000	20	830	0.001	17	
[26]	ECDL	TPA	7	DM	1000	10	830	0.001	17	
[27]	DBR	TPA	10	DM	1000	10	830	0.023		
[28]	2DBR	TPA	5.6	DM	900	9	830	0.023		
[30]	DBR	TPA	50	ML	0.001	16000	1064			
[31, 32]	DBR	TPA	60	Q-Sw	1000	0.008	1060	0.2		17.6
[33]	DBR	TPA	74	ML	0.001	1250	1060	1000		

laser with a spectral linewidth of about 0.03 pm (12 MHz bandwidth) and a diode flared amplifier as power amplifier. The DFB operated in continuous wave (CW) and the PA operation in pulsed mode. A peak power of 0.5 W with a pulse width of 600 ns at repetition rate of 6-10 kHz was obtained. The system could offer a minimum range resolution of 90 m (corresponding to a pulse width of 600 ns), measure a range of 18.75 km at a repetition rate of 8 kHz and need an average time of 30 minutes for the measurement.

Nehrir *et al.* used an $ECDL$ as MO and either two-stage amplification with a CW tapered pre-amplifier and a pulsed driven tapered amplifier [23, 24] or only one pulsed amplifier [25, 27]. At a wavelength of 824 nm a spectral width of 0.001 pm ($\leq$ 0.3 MHz bandwidth) with a $SMSR$ of 45 dB was reported at peak powers of 2 W [23] or 7 W [24, 25] or 10 W [27] respectively. The generated pulses at repetition rates between 20 kHz and 10 kHz were applied for water vapor profiling corresponding to ranges of 7.5 km and 15 km respectively, at a spatial resolution of about 150 m, and measured time of about 20 minutes. It is noted that in refs [23–27] the pulse widths were limited to τ =1 μs by the applied electronics.

Recently, Spuler *et al.* a report of field-deployable diode laser based differential absorption lidar ($DIAL$) for profiling water vapor was published [28]. Two DBR laser diodes emission at two wavelengths for on/off line and tapered semiconductor power amplifier were used. The pulse width of 900 ns at 9 kHz repetition rate provides a spatial resolution of about 150 m. With a repetition rate of 10 kHz a measuring range of 15 km and with 20 kHz repetition rate a range of 7.5 km would be possible together with 10 minutes for measured time.

Common for the above mentioned, a maximal peak power of 10 W [27], a pulse width of about 600 ns by directed modulation (DM) into the power amplifier [28] was reported. It leaded to result in a 90 m vertical resolution.

In ref [28], it was suggested that the power of the laser transmitter could be increased by increasing the injected current into the tapered power amplifier (TPA). However, it was reported that the exceeding pulse currents into the TPA could adversely affect transmitter lifetimes.

A suggestion of reducing the pulse duration to achieve higher spatial resolution should be considered.

Shorter pulses would allow improving the spatial resolution ΔL. The optical pulses in nanoseconds and picoseconds ranges can be generated by gain switching, Q-switching and mode locking of diode lasers either as monolithic devices or in $MOPA$ system.

In the Ferdinand-Braun-Institut, Leibniz-Institut für Höchstfrequenztechnik, numerous papers were reported. Klehr *et al.* [30] described a short pulse $MOPA$ system using a hybrid mode locked master oscillator. The energies in the nJ range with a pulse length in the 10 ps range (peak power of about 50 W) at a repetition rate of 16 MHz were obtained. Unfortunately, they did not mention the spectral linewidth and amount of ASE.

In[31, 32] Schwertfeger *et al.* used a single stage all semiconductor master oscillator power amplifier system, consisting of a Q-switches distributed Bragg reflector laser as master oscillator and a tapered power amplifier. They reported of pulses with a length of 80 ps, a peak power of 50 W [31] or 60 W [32] and a spectral width less than 0.2 nm around a center wavelength of 1066 nm. Wenzel *et al.* [33] showed gain switched modules for pulse widths in the range between 1 ns and 100 ns which provided a peak power of 10 W with a spectral width less than 0.1 nm. Q-switched modules for pulse widths around 100 ps yielded a peak power up to of more than 30 W with a spectral width less than 0.5 nm. Mode-locked DBR laser is combined with two-stage ridge wave-guide pre-amplified operation in CW and pulsed current for tapered section of 20 A. A peak power of 72 W with a pulse width of 9.2 ps at a repetition rate of 100 MHz was obtained. A spectral width around 1 nm was also reported in [33] .

Harth *et al.* used a DFB laser operated CW and a power amplifier consisting of pulsed modulator and amplifier sections [55]. By changing the temporal overlap of the modulator and amplifier current pulses, optical pulses with lengths between 0.4 ns and 1.0 ns were generated. The repetition rates were between 100 kHz and 816 kHz. A peak power of 0.6 W was reached with a $SMSR$ of 54.9 dB at 1064 nm wavelength.

A maximal peak power of 72 W could be achieved at the pulse width

of 9.3 ps with a spectral line width of 1 nm [33]. A complicated structure and modulation for both MO and PA were implemented. In contrast, the operation in ns pulse width, a $MOPA$ system consisting of DFB laser and a tapered amplifier integrated a ridge wave-guide were used. The ridre waveguide operation in CW was a pre-amplification section. The gain-switch operation of the DFB laser generated optical pulses. The tapered section was driven with pulse currents. A peak power of about 10 W with the spectral line width of 100 pm was observed [33].

In this work, $MOPA$ systems based diode lasers feature a spectral line width below 10 pm operation in ns pulse width at some 10 kHz repetition rate, a peak power above 10 W and an amount of amplified spontaneous emission (ASE) below 1%. The systems could be potential light sources for water vapor and aerosols detection in the $MPLs$ systems.

3 Diode laser based MOPA concept approaches

A master oscillator power amplifier ($MOPA$) is a configuration which consists of a master oscillator (MO) (a seed laser) and a power amplifier (PA) to boost the output power. Ideally the MO provides spectral and spatial properties of the system, whereas the PA only increases the power and preserves the MO's spectral properties. There are several approaches of the $MOPA$ configurations. For all-semiconductor laser systems, it can be distinguished into two concepts, monolithic and hybrid $MOPA$ systems.

In the monolithic $MOPA$, the MO and the PA are integrated on one chip. The device can be made of at least of two sections (MO and PA sections) or more additional sections. The MO acts as seed laser, the PA amplifies the power and another sections can be used for modulation or changing the phase. In our case, it consists of three sections, a Distributed Feedback (DFB) laser section as the MO, a ridge wave-guide section as an optical gate (OG) section and a tapered gain section as PA.

Due to the integration of MO and PA on one single chip, the temperature change within the tapered section during pulse operation effects properties of the MO.

The hybrid $MOPA$ system features separated chips for the seed laser (the MO) and the power amplifier (PA). Here, the radiation of the MO has to be coupled into the PA via suitable optics. The MO can be a $Fabry-Perot$ laser, a Distributed Bragg Reflector (DBR) laser, or a Distributed Feedback (DFB) laser. As mentioned above, a single-mode operation and a narrow spectral line width to adapt the requirement of aerosols and water vapor detection is needed. This in this work, the MOs are selected as $RW-DFB$ and $Y-branch-DFB$ lasers. This will be discussed in detail in following sections.

The PA has multiple sections used for pulse generator and amplification. Two structures of the PA are investigated, one of which is a four-section and other is a two-section device. The four-section tapered amplifier consists of two ridge wave-guide sections as optical filters for controlling the input power and avoiding the unwanted feedback, a ridge

wave-guide section as an optical gate and a tapered section as a gain section. The two-section device omits the optical filter section. Both types of PA are investigated to find out the better structure for hybrid $MOPA$ systems.

To generate the optical pulses, on the one hand, it can be achieved by injection pulses current directly into PA [22–28]. The pulse width was limited by a commercial pulse current driver [24, 26–28]. On the other hand, it can be obtained by modulation directed into the MO [30–33], the broaden spectral linewidth is reported. Using a ridge wave-guide section integrated in the tapered amplifier as an optical gate for pulse generation is a good solution. The optical gate is completely independent from the MO. Thus, it has no influence on the spectral properties of the MO which often cause the variation of wavelength during the optical pulse and fluctuations in the near and far field profiles under high injection conditions in the gain-switched diode lasers [56]. Furthermore, it is integrated into the tapered amplifier a compact system can be obtained.

An all diode laser system offers the compact, low cost systems which feature a stabilized wavelength, a tunability, a dual wavelength together with narrow spectral line width and small amount of ASE operation under ns-pulse operation.

In this part, a short description of the manufacturing of each device in the $MOPA$ systems is given. The properties of the systems will be discussed in the following chapters.

3.1 Monolithic MOPA concept

The monolithic $MOPA$ is a compact concept. It is integrated the MO and the PA on a single chip which was developed based on an established technology for obtaining high-power, nearly diffraction limited and wavelength-stabilized optical output [57, 58]. The scheme top view of monolithic $MOPA$ is shown in Fig. 3.1 a. The device consists of three sections, a 1 mm long ridge wave-guide distributed feedback $RW-DFB$ section as the MO, a 1 mm long ridge wave-guide section as optical gate (OG) and a 4 mm long tapered section as gain section (TS). The DFB

section and optical gate section (OG) has a 5 μm width of ridge wave-guide for the lateral optical confinement. The tapered section has a full taper angle of 6° [57–59].

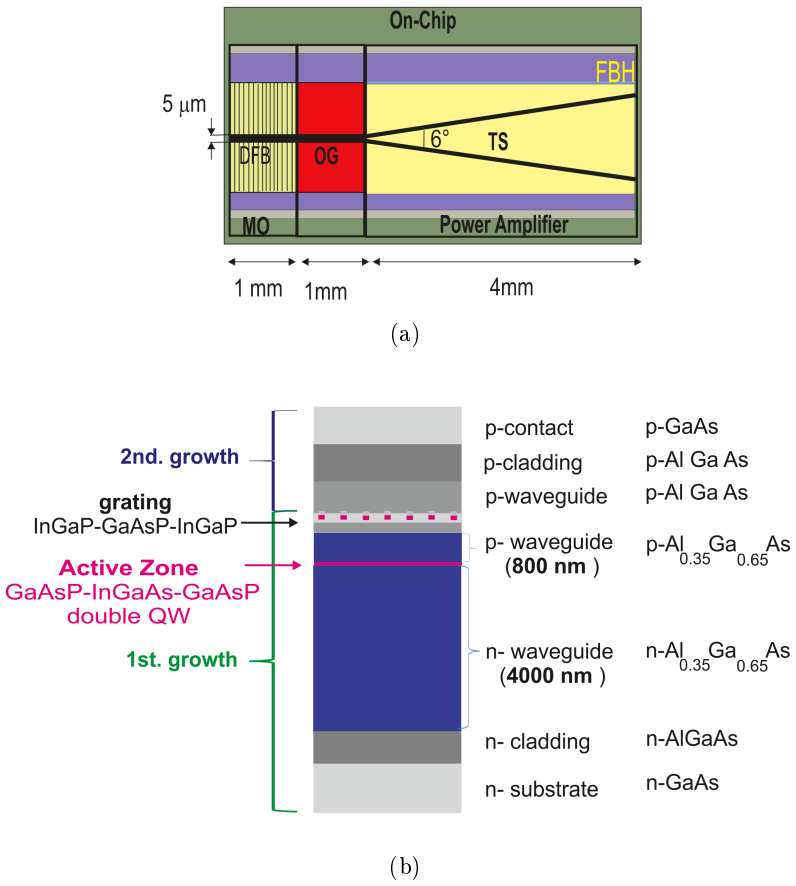

Figure 3.1: a) Schematic diagram of top view of monolithic MOPA system.
b) Epitaxial layer structure of the monolithic MOPA.

As the device features a $RW - DFB$ section, the vertical wave-guide structure is grown by metal organic vapor phase epitaxy in two steps, shown in Fig. 3.1 b. In the first growth step, the vertical structure including n-$GaAs$ substrate, the n-$AlGaAs$ cladding, the broad n-$AlGaAs$ wave-guide, the double quantum well of $GaAsP/InGaAs/GaAsP$ active region, the first part of the p-$AlGaAs$ wave-guide and the grating layer sequence ($InGaP/GaAsP/InGaP$), respectively are grown. To achieve a small vertical far field divergence a double quantum well active region placed asymmetrically into the 4.8 μm broad $AlGaAs$ vertical wave-guide is implemented.

Then the Bragg gratings are realized by holographic photo-lithography and wet-chemical etching into the $InGaP/GaAsP/InGaP$ layer sequence. The second order Bragg grating with a period of about 320 nm for lasing at a wavelength of 1064 nm is performed [59, 60].

When the Bragg grating process is finished, the second epitaxy step is performed in order to complete the vertical structure with the remaining the p-$AlGaAs$ wave-guide, the p-$AlGaAs$ cladding and highly doped p-$GaAs$ contact layer. It is now ready for lateral structure implementation.

The process is started by etching the ridge wave-guide (RW). Then an insulation layer is deposited which is opened at each section to allow separated contacts by subsequent metallization. A 5 μm ridge wave-guide is created in the DFB section and optical gate section (OG) for the lateral optical confinement which supports only the fundamental guide mode. Consequently, it is suppressed the higher order modes generated in the tapered section and reflected back/forward at the front facet. The tapered section has a full taper angle of 6°. The back side of the DFB facet is coated with a reflectivity of $R > 0.9$ whereas the amplifier facets have an anti reflectivity (AR) coating with a remaining power reflectivity of $R \leq 5 \times 10^{-4}$. The device is mounted p-side up on C-mount for individual currents for each section. The fabrication of devices can be found in more detail in refs [57–59].

3.2 Hybrid MOPA concepts

The principle of a hybrid $MOPA$ systems is shown in Fig. 3.2. It consists of a master oscillator, optical components and a power amplifier. In this part, a short description of the operation principle and manufacture of MO and PA used in this work are given.

3.2.1 Master oscillators

As mentioned above, the development and understanding of light sources for water vapor and aerosol detection in the troposphere is the target of this work. A single mode operation and a narrow spectral

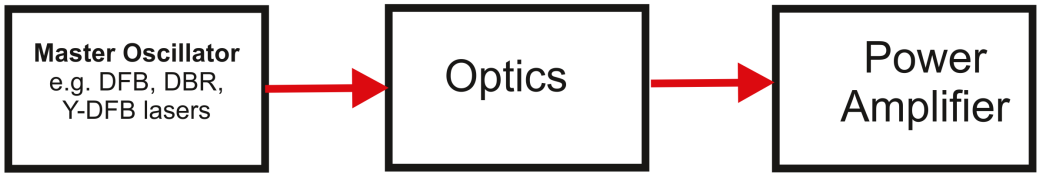

Figure 3.2: Schematic diagram of hybrid MOPA system

line width below 10 pm are needed. For this, a single-mode operation in lateral as well as in vertical direction is prerequisite. A stabilized wavelength at a specific wavelength can be applied for $LIDAR$ systems where a certain position is selected. In $DIAL$ application, a continuous tuning for scanning over the absorption lines or a dual wavelength for switching between on and off of an absorption line, respectively can be used.

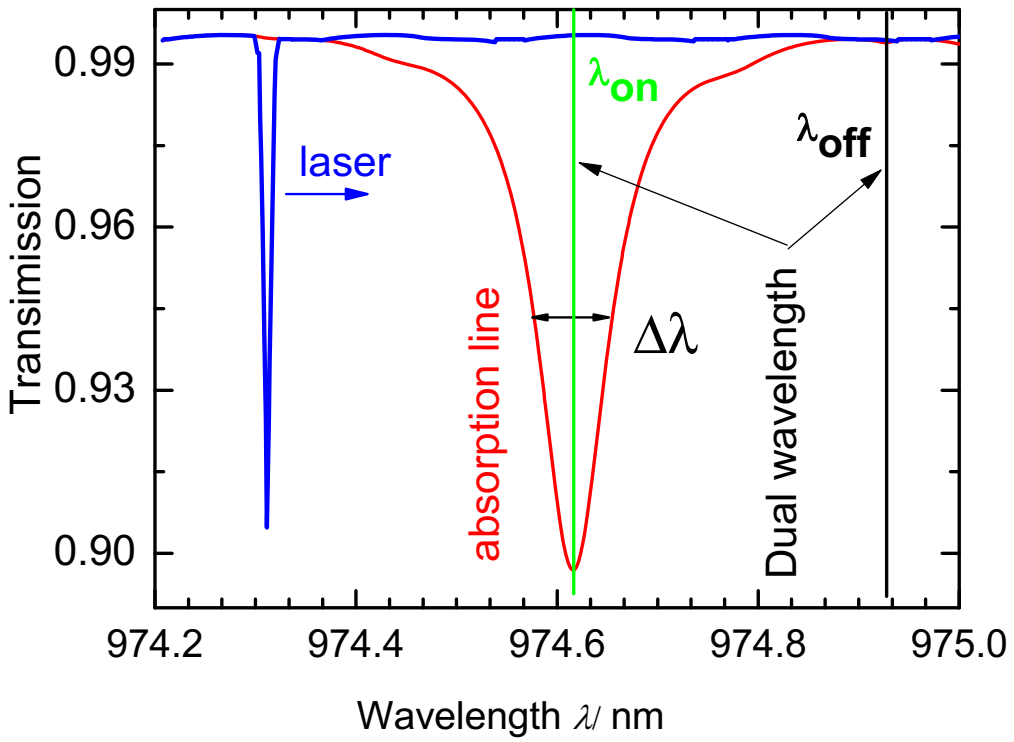

Figure 3.3: The sketch of principle of scanning over absorption lines or switching between on/off of an absorption line

Fig. 3.3 shows the sketch of principle of the scanning over absorption line or switching between on/off of an absorption line. An example of an absorption line (red color) of the water vapor, a laser line (blue color) and a dual wavelength for on/off (green and black color) absorption line are given. A continuously tuning laser emission should be scanned over at least an absorption line. This allows to measure the profile of an absorption line therefore the broader or narrower absorption line, effected by pressures or temperatures can be determined. In other case, the laser tuning range can scan over several absorption lines, it is possible to select a wavelength at an absorption line having suitable strength for the atmospheric condition. For switching between on/off of an absorption line, it needs two wavelengths, one is located at the center of the absorption line and another is located outside of the absorption line, as shown in Fig. 3.3. The concentration of the water vapor then can be determined by the equation 2.2 given in the previous chapter. In this work, the diode laser based $MOPA$ systems suitable for these applications are expected.

The MO should offer a single mode operation together with a wavelength stabilization and a continuously tuning wavelength or dual wavelength emission. In case of stable and continuous tuning wavelength, a distributed feedback (DFB) or a distributed Bragg reflector (DBR) laser can be applied. For dual wavelength a $Y - branch - DFB$ laser can be used.

Due to in DBR laser the Bragg grating is located in the rear side of the cavity. Thus, the currents are only injected into the gain section, therefore the DBR section acts purely as a mirror. However, DBR lasers suffer from the periodic non-linearity in the light-current characteristics due to longitudinal mode hopping.

In contrast DFB lasers the Bragg grating is spread over the entire cavity. Thus the current is injected through the grating. The DFB lasers can operate in the same longitudinal mode over a large current range which leads to linear light-current characteristics and a continuously tunable wavelength [61]. Therefore, $RW - DFB$ and $Y - branch - DFB$ lasers are selected as master oscillator in this work.

3.2.1.1 RW-DFB laser as master oscillator

$RW-DFB$ lasers generate a single longitudinal mode oscillation due to a Bragg grating along the path of propagation. The periodic grating is created by a periodic variation of the material compositions and therefore the refractive index. A $RW-DFB$ laser is combined a conventional $Fabry-Perot$ laser with a Bragg grating throughout the cavity length at the ridge wave-guide layers. It acts as a wavelength selective element and provides the feedback, reflecting light back into the cavity to form the resonator, so that only frequency (wavelength) components close to the Bragg frequency will be coherently reinforced. Other frequency (wavelength) terms are effectively cut off as a result of destructive interference [34, 61]. In other words, single longitudinal mode operation in the DFB laser is achieved due to the wavelength selection of the Bragg condition. The Bragg condition can be expressed as [61]

$$\Lambda = \frac{m\lambda_B}{2n_{eff}}. \tag{3.1}$$

where Λ is the grating period, n_{eff} is the mode effective index, and the integer m represents the order of Bragg diffraction. Depending on the targeted wavelength emission, the grating period, the order of the Bragg diffraction and the refractive index of the material have to be considered. For instance, a grating period of $\Lambda = 150\,\text{nm}$ for a first-order Bragg grating and a refractive index of about 3.25 result in lasing at 975 nm. A period of $\Lambda = 324\,\text{nm}$ with a second-order grating and a refractive index of about 3.28 emit at 1064 nm [62–67].

Due to the effective refractive index dependence on the temperature and the injected carrier density, changing the temperature causes a change in refractive index, leading to a alteration the wavelengths. An inverse effect to changing temperatures, the refractive index also depends on carriers density or injection currents. A tunable single mode laser in DFB lasers therefore is achieved by fine tuning the refractive index which can be controlled by changing the temperature and carrier density. More detail theory of changing refractive index by temperature and carrier density of DFB lasers can be read in refs [35, 61].

A narrow spectral line width can be obtained when both vertical and

lateral directions operate in single mode. The vertical single mode is achieved by the design of the vertical wave-guide structure. The material layers with the different refractive index and the band gap are used to confine carriers and wave-guiding. The wave-guiding layers above and below the active region with a refractive index higher than the cladding layers and lower than the active region are used. Materials with a lower refractive index are typically also exhibiting a larger band gap. This is an important feature since light is not absorbed in the surrounding layers.

For lateral optical confinement, gain guided lasers or index guiding/ridge wave-guide (RW) lasers can be used. Gain guided lasers use the refractive index difference in the lateral direction due to different carrier densities in the pumping process. They are usually used for high power devices [68]. The dependence of optical confinement on the carrier density is a drawback and they typically do not provide a stable single mode operation.

In contrast, index guiding (ridge wave-guide) lasers control better and provide a tight lateral confinement of the optical field in combination with a narrow width. They enable to operate in single lateral mode.

In this work, DFB lasers with an emission at 1064 nm or 975 nm are used. Both of them are grown by metal organic vapor phase epitaxy in two-step. In Fig.3.4 a, the vertical structure of the $RW - DFB$ lasers emission at 1064 nm is given. The vertical structure is identically grown to the monolithic $MOPA$, described in section 3.1. For small vertical far-field divergence, the active region is a double quantum well (DQW) placed asymmetrically in a 4.0 μm n-$Al_{0.35}Ga_{0.65}As$ and a 0.8 μm p-$Al_{0.35}Ga_{0.65}As$ wave-guide. This structure features a vertical far-field divergence of about 15° ($FWHM$) [59, 68].

The Bragg grating is implemented into the p-$InGaP/GaAsP/InGaP$ layer sequence. The thickness of the grating layer and the distance between the active region and grating layers have to be controlled for the desired wavelength and the coupling coefficient. The period of the grating depends on the effective index of the vertical structure, which is designed for a desired emission wavelength of the laser. A grating period of 150 nm with the first order is calculated for lasing at 1064 nm

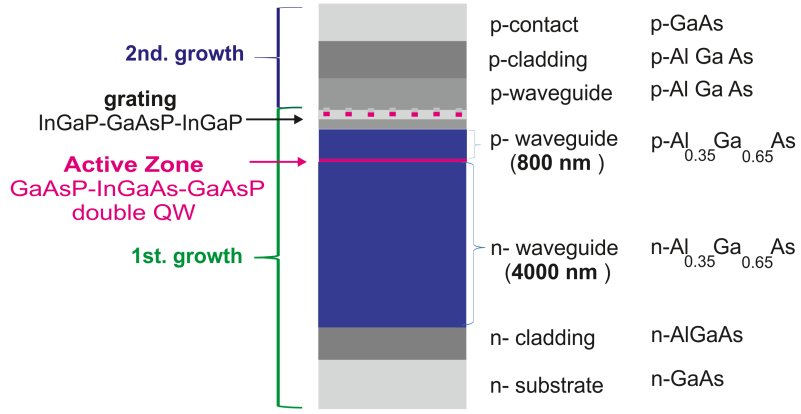

(a)

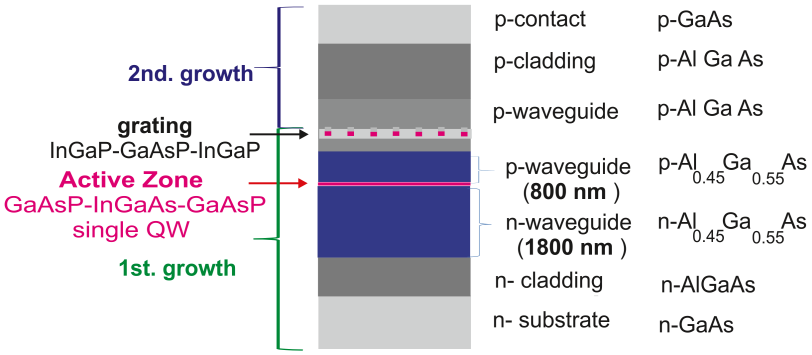

(b)

Figure 3.4: a) Epitaxial layer structure of the DFB laser emission at 1064 nm.
b) Epitaxial layer structure of the DFB laser emission at 975 nm.

wavelengths.

In Fig.3.4 b, the vertical structure of the $RW-DFB$ lasers emitting at 975 nm is shown. The first epitaxial step includes of the n-$GaAs$ substrate, the n-$AlGaAs$ cladding, the 1.8 μm broad n-$Al_{0.45}Ga_{0.55}As$ wave-guide, active region, the first part of the 0.8 μm p-$Al_{0.45}Ga_{0.55}As$ wave-guide and the p-$InGaP$-$GaAsP$-$InGaP$ grating sequence. The active zone has a compressible strained $InGaAs$ single quantum well SQW sandwiched between $GaAsP$ spacer layers. This structure features a vertical far-field divergence of about 23° ($FWHM$) [69].

The Bragg grating is implemented into an p-$InGaP$-$GaAsP$-$InGaP$ layer sequence. A grating period of 324 nm with the second order fea-

tures lasing at 975 nm wavelengths.

The second epitaxial growth for both is performed to finish the p-$AlGaAs$ cladding. Finally, the p-$GaAs$ contact layer is grown on top of the wafer.

After completing the vertical structure, the lateral structure is processed in ridge wave-guides (RW) and to metallize the electrical contacts. Following processing is similar to the description in 3.1. To ensure fundamental lateral mode propagation along the optical cavity, a RW width of about between 2.2 μm and 5 μm can be implemented for different wavelength emissions.

As the next step, several microns thick gold layer was electroplated on top of the p-metallization. After the evaporation of the n-contact, the wafer is cleaved into bars with lasers having a desired cavity length. In this case, cavity lengths of 1 mm and 3 mm are used. Then the front and rear facets are anti-and high-reflection coated, respectively. The diode lasers are then mounted on C-mount. Further details of the fabrication of the devices were described elsewhere in [62, 67, 68, 70–73]. Fig. 3.5 shows a scheme of a $RW - DFB$ laser. Here, the cavity lengths of devices have 1 mm to 4 mm, the reflectivities of about 95% and $\leq 5 \times 10^{-4}$ for the rear and front cavity are used. The Bragg grating in the p-ridge wave-guide is shown.

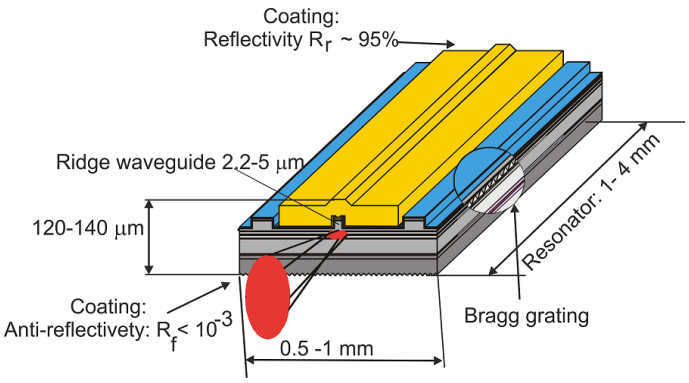

Figure 3.5: Schematic diagram of a RW DFB laser

3.2.1.2 Dual wavelength Y-branch-DFB lasers

As mentioned above, for $DIAL$ application, two wavelengths for online and offline wavelengths are needed. It can be achieved by using two

MOs for two wavelengths [21, 49, 74]. Recently, the $Y-branch-DFB$ laser emits dual wavelength was introduced [75]. It is a good selection for a laser transmitter in differential absorption $LIDAR$ ($DIAL$) application. The manufacturing of these two-wavelength lasers will be discussed in this part. Their properties will be shown in the following chapter.

The vertical structure is grown in one epitaxial step as shown in Fig.3.6 a. It is included the n-$GaAs$ substrate, the n-$AlGaAs$ cladding, the 1.6 μm broad n-$Al_{0.25}Ga_{0.75}As$ wave-guide, the $GaAsP-InGaAs-GaAsP$ active region, the 0.8 μm broad p-$Al_{0.25}Ga_{0.75}As$ wave-guide and finally p-$GaAs$ cladding. A strain compensated $GaAsP-InGaAs-GaAsP$ DQW as active region embedded in asymmetric $AlGaAs$ confinement and cladding layers is employed.

The lateral structure starts with the definition of 80^{th} order Bragg gratings in the DFB sections. The grating is calculated to obtain a coupling coefficient length product κL $= 0.3 \div 0.5$ in order to achieve a good laser performance [76], κ is grating coupling coefficient and L is length of the cavity. This corresponds to a reflectivity of a passive grating about 10 to 20%. I-line wafer stepper lithography is used to expose the Bragg grating into the resist. Reactive ion etching is used to form V-shape grooves. The Bragg grating periods of 11520.0 nm and 11567.6 nm are applied to provide two wavelengths with a distance between each other of about 4 nm. Its space is selected for two wavelengths suitable for the online and offline absorption lines, it will be seen later in the chapter seven.

In lateral structure, the ridge wave-guide in the DFB section, $Y-branch$ and common section are also etched by reactive ion etching [75]. The following steps such as deposition of the insulation layer, metallization, deposition of plated gold and cleaving, facet coating and mounting are implemented. The reflectivities at rear and front facets are about 95% and below 0.1%, respectively.

Schematic top view of a $Y-branch-DFB$ laser is shown in Fig. 3.6 b. It can be seen that the device has a 4 mm length, separately from three sections. It consists of a 2 mm length of the DFB section, a 1.6 mm length of $Y-branch$ and 0.4 mm length of the common section. The

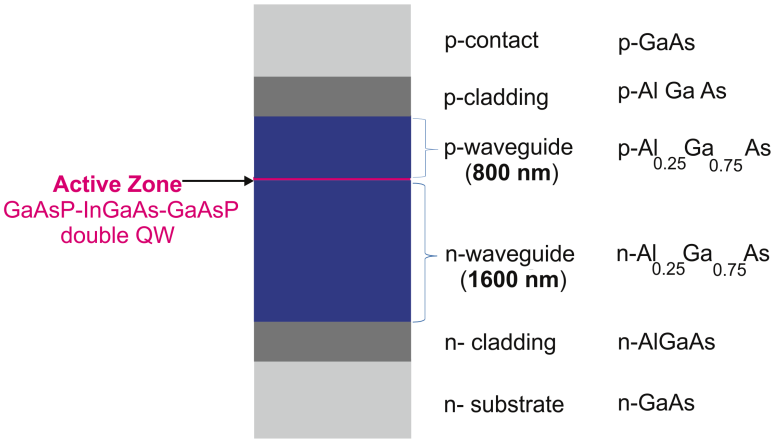

(a)

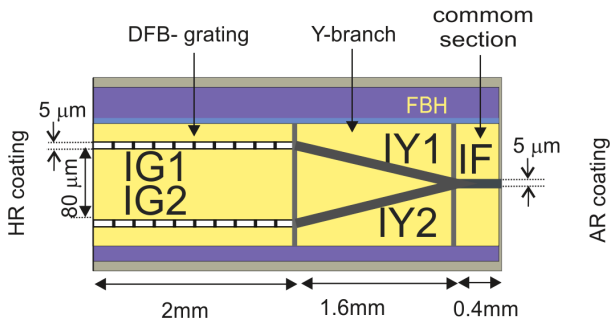

(b)

Figure 3.6: a) Epitaxial layer structure of $Y-Branch-DFB$ laser.
b) Top view of the $Y-Branch-DFB$ laser.

RW width has $5\,\mu$m and a distance between the two branches of $80\,\mu$m. The Y-branch section having S-bend shape features low the internal losses and symmetric devices for identical signals at the output of two branches.

3.2.2 Multi-section tapered power amplifiers

In contrast to laser devices, the tapered amplifier does not feature a resonator, the rear face is an anti reflection coating. It needs another devices for input signal and then amplifies the input signal by providing

optical gain. Two devices with four-section and two-section are used. The four-section device operates at 1064 nm and the other one operates at 975 nm. The function of each section will be presented in detail in the following. In this part a short description of fabricated devices is given.

3.2.2.1 Four-section tapered power amplifier

The vertical structure can be performed in one step epitaxy; It consists

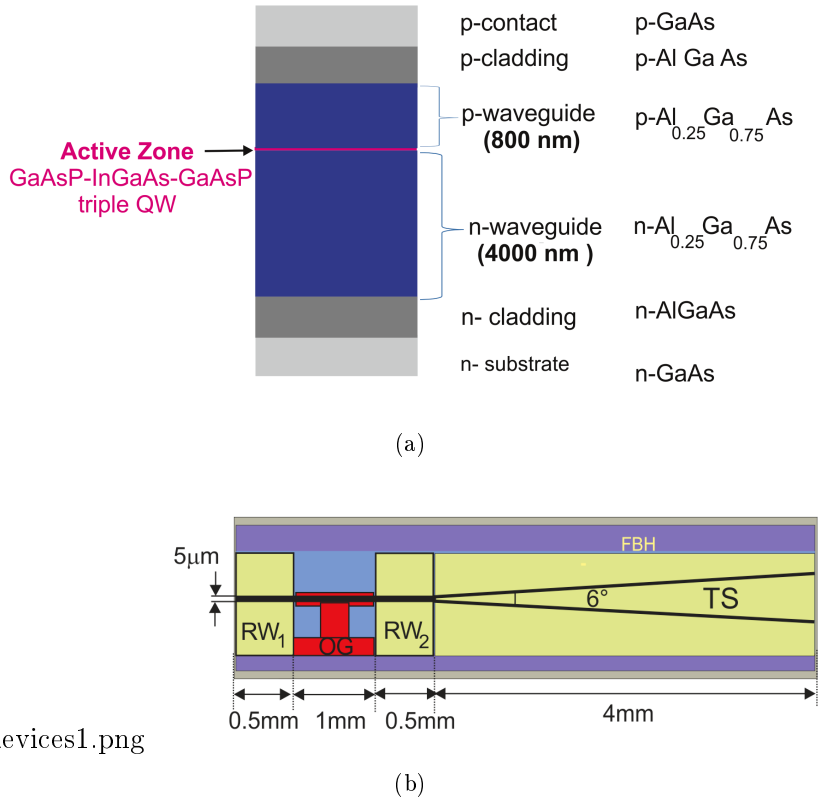

Figure 3.7: a) Epitaxial layer structure of four-section tapered amplifier.
b) Top view of a four-section tapered amplifier.

of the n-$GaAs$ substrate, the n-$AlGaAs$ cladding, the 4 μm broad n-$Al_{0.25}Ga_{0.75}As$ wave-guide, an $InGaAs$ triple quantum well as active zone, 0.8 μm p-$Al_{0.25}Ga_{0.75}As$ wave-guide and p- $AlGaAs$ cladding. The active zone also is embedded in an asymmetric $AlGaAs$ based on super large optical cavity to provide a narrow vertical divergence [33, 60]. The epitaxial layer structure is shown in Fig. 3.7 a.

After the vertical structure is finished, the process is to form the ridge wave-guide sections and tapered section. It is identical to the description in section 3.1. The device length is 6 mm and is divided into 4 sub-sections. The first and third ridge wave-guide sections (RW_1 and RW_2) have a 500 μm length and 5 μm width ridge wave-guide acting as optical filters. The second ridge wave-guide has 1000 μm long and 5 μm width acting as optical gate (OG). The output is a tapered section (TS) having a 4000 μm and a full taper angle of 6° as gain section. The front and the rear facets are passivized and anti-reflection-coated with a reflectivity of $R \leq 5 \times 10^{-4}$ in the spectral range between 1045 nm and 1065 nm. The device is mounted p-side up on a C-mount. The top view is shown in Fig. 3.7 b. All electrically separated sections can be driven individually.

3.2.2.2 Two-section tapered power amplifier

The two-section amplifier is also grown in one epitaxial step. To amplify in the 980 nm region, the active region is an $InGaAs$ double quantum well sandwiched between $GaAsP$ spacer layers. It is also embedded in an asymmetric $AlGaAs$ super large optical cavity to obtain a narrow vertical far-field divergence. The epitaxial layer structures is shown in Fig. 3.8 a. The lateral process for wave-guide section and the tapered section is performed identically to the four-section.

The top view of indicated scheme is shown in Fig. 3.8 b. The amplifier with a total length of 6 mm consists of a 2 mm long ridge wave-guide (RW) section with a 5 μm wide ridge wave-guide and a 4 mm long gain-guided tapered section (TS) with a full taper angle of 6 °. The front and the rear facets are passivized and anti-reflection coated with reflectivities of $R \leq 5 \times 10^{-4}$ in the spectral range from 965 nm to 985 nm. The device is mounted p-side up on a C-mount allowing individual excitation of the two sections.

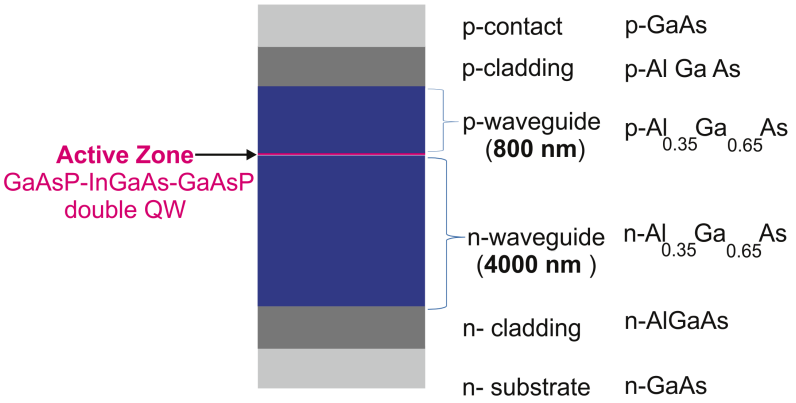

(a)

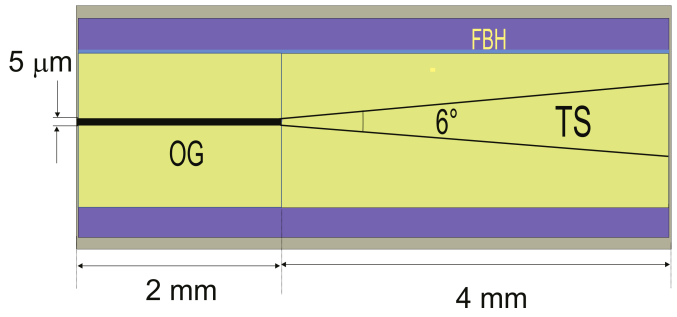

(b)

Figure 3.8: a) Epitaxial layer structure of two-section tapered amplifier. b) Top view of a two-section tapered amplifier.

4 Experimental setup

In this section, the experimental setups used for measuring the characterizations under continuous wave (CW) excitation and under the ns-pulse excitation are given.

For CW excitation, the characterized electro-optical and spectral property setups are given. The characterized electro-optical setup can be used for optical output power and junction voltage versus injection current of the diode laser measurement. It also can be measured the power amplified spontaneous emission (ASE) versus current for tapered amplifier. The second experimental setup is used to measure spectral properties of the lasers and the gain (ASE) profile of tapered section (TS).

For ns-pulse excitation, an experimental setup for optical peak powers and spectral properties measurement will be given. By using this setup, the pulse shape, peak power and spectra can be measured.

The electrical circuits for ns-pulse of optical gate (OG) and TS section is presented.

4.1 Characterization under continuous wave excitation

4.1.1 Electro-optical characterization

The optical output power and the junction voltage of the diode lasers versus forward bias current are measured by the experimental setup as shown in Fig. 4.1. From this, the threshold current, the slope efficiency ($S = {}^{\Delta P}/_{\Delta I}$), electro-optical efficiency ($\eta = {}^{P}/_{UI}$) can be determined.

The experimental setup consists of a diode laser and a diode laser mount, a laser diode driver (Model 525B), a temperature controller (350B Laser Diode Thermal-electric Temperature Controller) and the detection (Thermal Solo XLP 12-3S-H2-DO). The laser beam is directly collected into the detector.

The diameter of the active area of the thermopile Gentec $EO - XLP12 - 3S - H2 - DO$ is 12 mm. Its spectral range is 0.19 μm-20 μm. The maximum average optical power up to 3 W can be detected.

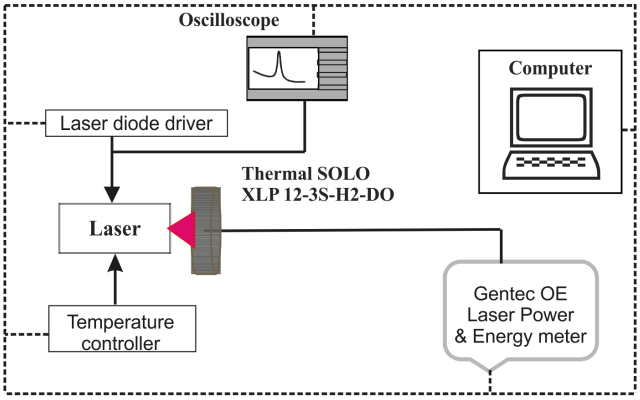

Figure 4.1: Schematic diagram of experimental setup for PUI characteristics

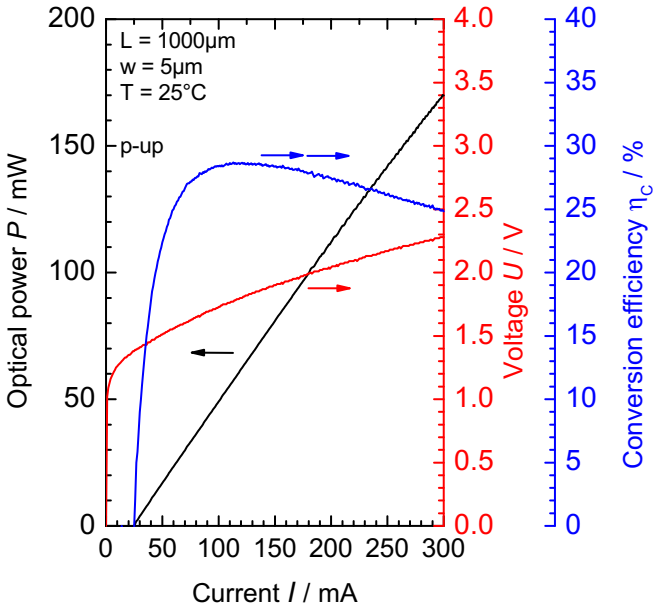

Figure 4.2: A typical example of PUI characterizations of a p-side up mount DFB laser emitting at 1064 nm at temperature of 25 °C.

The output power is obtained in Watts directly from the Gentec-SOLO monitor and is calibrated to ±2.5% of national standards. The bias voltage is measured by an oscilloscope at the two contacts of the laser mount. Note that the small voltage drops across the contacts and the bonding wires are included as well.

The laser diode driver (Model 525B) can supply currents with two

ranges of 0 mA to 1000 mA and 0 mA to 2500 mA, the resolutions of 0.1 mA to 2.5 mA, the accuracy of ± 1 mA and ± 3 mA, respectively. The temperature controller (Model 350B) features a stable temperature 0.001 °C over a broad range from -50 °C to 150 °C. The setup is controlled by a computer via $GPIB$ interfaces.

A typical example of PUI characterizations of a DFB laser emission at 1064 nm wavelength at the heat-sink temperature of 25 °C is shown in Fig. 4.2. The black, the red and the blue lines represent the PI characteristics, the UI characteristics, and the conversion efficiency as derived from the PUI characteristics, respectively. The figure illustrates that at the heat-sink temperature of 25 °C, the device has a threshold current of about 26 mA, and at an injection current of 300 mA, an output power of $P = 170$ mW is obtained at a forward voltage drop of 2.3 V, leading to a conversion efficiency of 24.5%. The slope efficiency determined slightly above threshold current is 0.62 W/A. A maximum conversion efficiency of about 28% is obtained at 110 mA.

4.1.2 Spectral properties

The experimental setup is sketched in Fig. 4.3. The entrance port of the OSA is compatible with FC/PC-terminated fiber patch cables. Therefore, the laser beam has to be focused in an optical fiber. An aspheric lens (352330B/C-Thorlabs) (focal length $f = 3.1$ mm, Numerical aperture $NA = 0.69$) is used to collimate the laser beam. An optical isolator (Thorlabs $IO-980-5-HP$, 40 dB or Qioptiq $FI-1060-TI$, 60 dB isolation) is used to avoid unwanted feedback to the laser. Then an another aspheric lens ($f = 3.3$ mm, $NA = 0.47$) is employed to collimate light into the entrance of a single mode optical fiber. This is connected to the entrance port of the (OSA).

In this work, the optical spectrum analyzer (OSA) (Advantest Q8384) having a spectral resolution of 10 pm and a dynamic range of 60 dB is used.

As mentioned above, the targets are to demonstrate the light sources offering a narrow spectral line width, a stable wavelength, a continuously tunable wavelength and a dual wavelength. It is necessary to understand

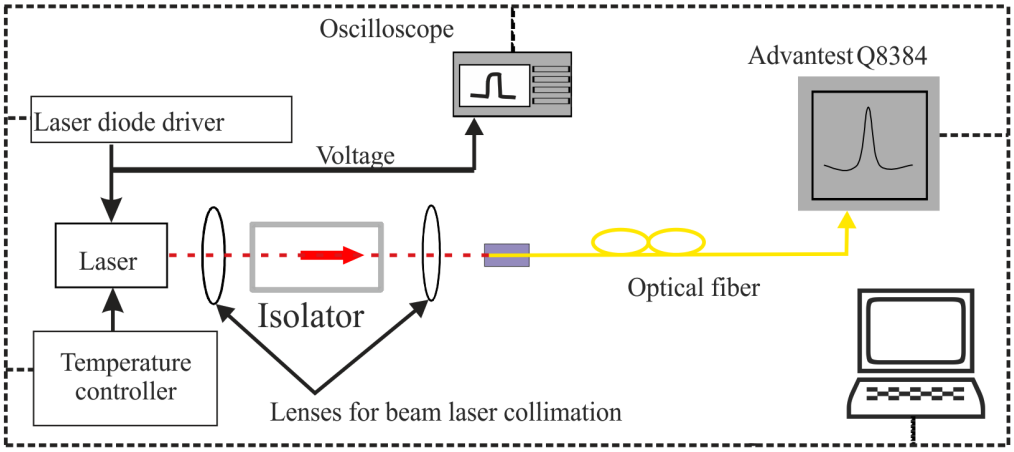

Figure 4.3: Schematic diagram of experimental setup for measurement of spectral properties.

the behavior of spectral properties of the lasers under changing the injection current and the temperature. Moreover, it also used to determine the experimental conditions for further investigation.

Using this setup to measure the spectra, the center emission wavelength, the single longitudinal mode operation, the side mode suppression and the dependence of these quantities on the diode laser injection current and the diode laser (mount) temperatures can be estimated. The corresponding data can be displayed in a color-mapping, with the axes corresponding to wavelength, current and intensity. This analysis allows extraction of the wavelength shift of the laser versus the operating current.

The dependence of the laser emission spectrum on the temperature is also measured. This provides useful information for the analysis of spectral properties, for example measurement of center wavelength instability under fluctuation of surrounding temperature. Moreover, it enables to measure the gain medium or amplified spontaneous emission of optical amplifiers.

A typical example of spectra of a DFB laser emission at 1064 nm is shown in Fig. 4.4 at an output power of 30 mW (80 mA) at 25°C. It is seen that a single mode laser emission at the wavelength of 1063.5 nm with a spectral line width below 10 pm and the side mode suppression

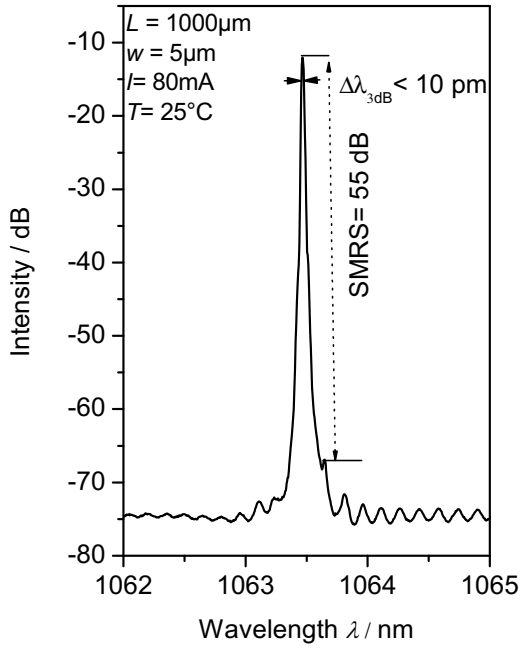

Figure 4.4: Optical spectrum at an output power of 30 mW (80 mA) at 25°C.

ratio ($SMSR$) of about 55 dB are determined.

Fig. 4.5 is an example of color-scale mapping of the optical spectra in dependence of the currents at temperature of 25°C. It shows a single mode operation with a continuously tuning range of about 1.3 nm by varying current from 40 mA to 300 mA (corresponding to 5.0 pm/mA) at temperature of 25°C.

A typical example of the color-scale mapping of the optical spectrum in dependence on temperatures at the current of 50 mA is given in Fig. 4.6. The wavelength shifts from 1062.7 nm to 1065.4 nm when the laser mount temperature increases from 15°C to 50°C (corresponding to 73.0 pm/K) at current of 50 mA.

4.2 Characterization under ns-pulsed excitation

In principle, power current characterization and spectral properties operation in ns-pulsed region can be identically performed to experimental setups under CW excitation. However, the ns-pulse excitation

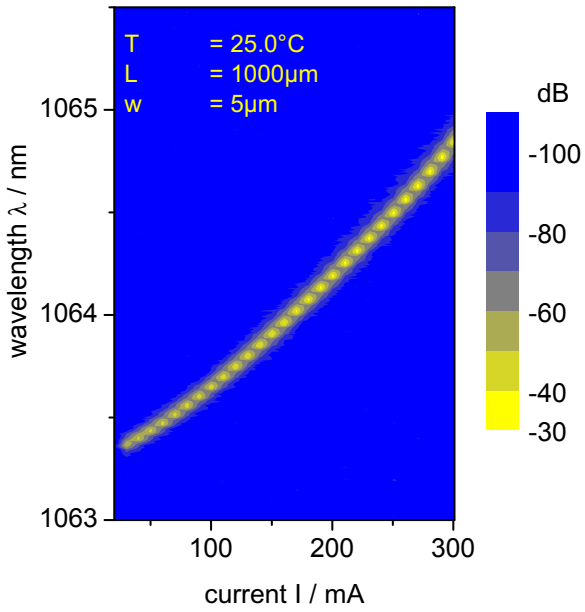

Figure 4.5: Color-scale mapping of the optical spectra in dependence on the currents at temperature heat sink of 25°C.

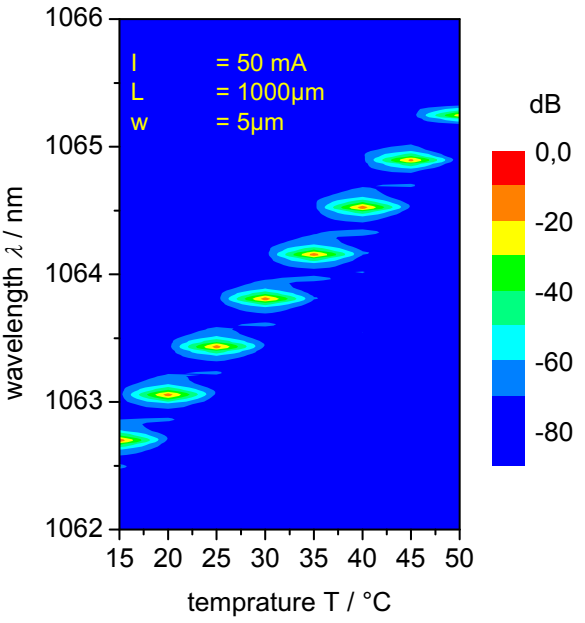

Figure 4.6: Color-scale mapping of the optical spectra in dependence on temperatures at current of 50 mA at about 15 mW.

is applied, and therefore the average values of the optical power and the temporal pulsed shapes have to be measured. The measuring process has two main steps.

Firstly, the full temporal pulsed shape of a single pulse is measured by fast photo-diode, displayed pulse shape on the screen of the oscilloscope and recorded by both the computer and the oscilloscope. The average power versus pulse currents is measured by the thermopile Gentec EO-XLP12-3S-H2-DO as similar to the experimental setup under CW excitation.

Secondly, combining the pulsed shape and the averaged power, the optical peak power as a continuous function of time can be calculated as following.

The optical peak power is then calculated by

$$P(t) = \frac{\phi(t) * P_{avg} * T}{\int \phi(t)dt} \tag{4.1}$$

where $\phi(t)$ is the temporal shape of the optical pulse, P_{avg} is the average power, and T is the period ($T = 1/f$, f is the repetition rate).

The experimental setup under ns-pulse excitation is shown in Fig 4.7. It consists of light sources ($MOPA$), the optical components (lenses, isolator, mirrors, optical fibers) for coupling the laser beam, power supplies (the electrical circuits, current supplies, temperature controllers) for modulation and computer for recorded database.

To measure the optical peak power, fast photo-diodes either the $InGaAs$ pin photo-diode (New Focus 1434) or the high speed $InGaAs$ PIN photo-diode (C30617BH EXCELITAS) are used. Collimation of the laser beam have to be considered for accurate measurement. More details of the optical collimation, electric modulation and fast detectors will describe as follows.

Firstly, the collimation of the laser beam from the MO into the RW section of the power amplifier is given. Two aspheric lenses (**L1** and **L2**, $f = 3.1\,\text{mm}$, $NA = 0.69$) and an optical isolator ($IO - 980 - 5 - HP$ 40 dB or $FI - 1060 - TI$ 60 dB isolation) for 975 nm and 1064 nm, respectively are used. The emitted light from the MO is collimated by the first lens (**L1**), passing an optical isolator and is then focused by another aspheric lens (**L2**) into the RW section of the power amplifier.

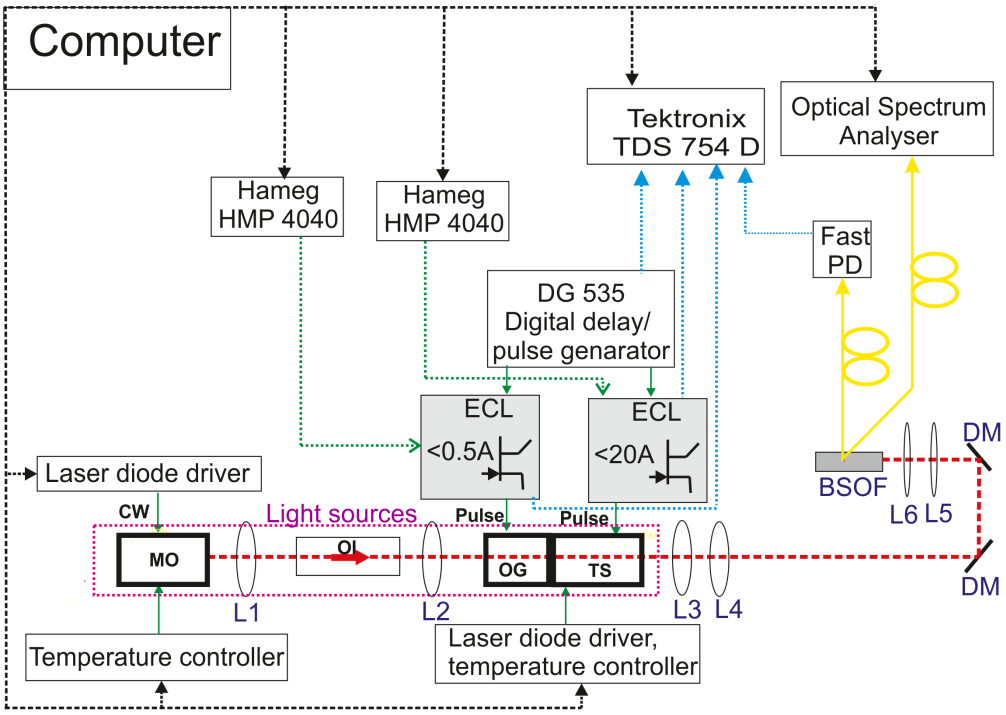

Figure 4.7: The experimental setup for optical peak power and spectra in ns- pulse excitation. Light sources (MOPA): MO, **L1**,**L2** (352330-C/B), $f = 3.1mm, NA = 0.69$, optical isolator (OI) and tapered amplifier with integrated optical gate (OG+PA); Aspheric lens **L3** (352330-C/B) $f = 3.1mm, NA = 0.69$; Cylindrical lens **L4** (LJ1477L1-B/C), f= 70 mm; Bi convex lenses **L5**, (LB1471-B/C) f= 50 mm; Aspheric lens **L6** (A414TM- B/C)(f= 3.3 mm, NA= 0.47; Broadband dielectric mirrors (BB1-E03), **DM**; Beam splitter optical fiber 1×2, **BSOF**).

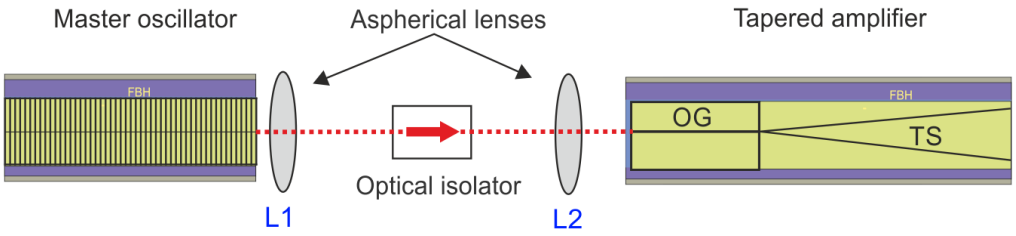

Figure 4.8: Schematic showing the coupling of the collimated laser beam from the MO into the RW section of the power amplifier.

A scheme of collimation laser beam from the MO into the RW section of the power amplifier is sketched in the Fig. 4.8.

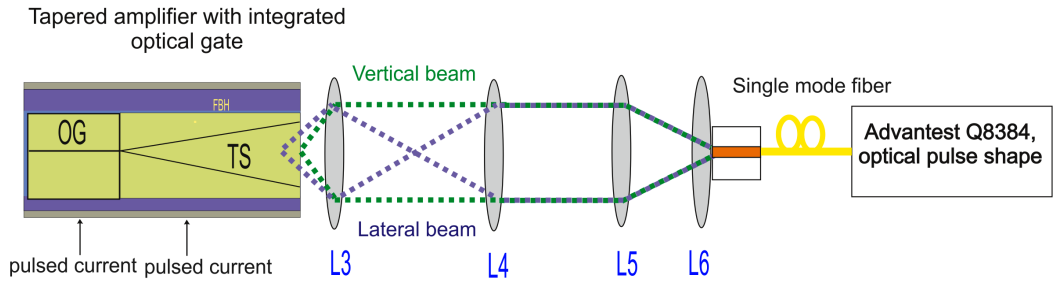

Figure 4.9: Schematic showing the collimated beam of the tapered amplifier with the out-coupling optics to compensate the astigmatism

Secondly, the collimation laser beam coming out of the hybrid $MOPA$ is shown in Fig 4.9. The lenses used, the positions of lenses, the beam waist and the far-field distribution should be calculated by the available software "WinABCD" at the FBH written by Eppich [77]. The aspheric lens (**L3**, $f = 3.1\,\text{mm}$, $NA = 0.69$) is used to collimate the vertical detection and the cylindrical lens (**L4**, $f = 70\,\text{mm}$) is used to collimate the lateral direction the laser beam. The astigmatism of (-1.4 mm) is approximately estimated. The laser beam coming out after the lens (**L4**) having the vertical diameter of 10.1 mm and the lateral diameter of 1.41 mm is calculated. With this beam the average power can be measured by using the Gentec Solo2 $EO - XLP12 - 3S - H2 - DO$ (the diameter of the active area of 12 mm).

In order to measure the spectra the entrance port of the OSA is a single mode optical fiber. It is necessary to focus the laser beam into a single mode optical fiber. A bi convex lens ($f = 50\,\text{mm}$, **L5**) and another aspheric lens ($f = 3.3\,\text{mm}$, $NA = 0.47$, **L6**) are used. A vertical diameter of $6.27\,\mu\text{m}$ and lateral diameter of $8.85\,\mu\text{m}$ are simulated. These diameters are sufficient to enter a single mode fiber with a diameter about of $9\,\mu\text{m}$. A beam splitter optical fiber 1×2 is used to split into two parts for the measurement of both spectra and optical pulse shape.

For pulsed shape, it is used either the $InGaAs$ pin photo-diode (New Focus 1434) or the high speed $InGaAs$ PIN photo-diode (C30617BH EXCELITAS). The entrance port of the New Focus 1434 is a single mode optical fiber, it can measure at the second part of the splitter optical fiber

as used in measurement of spectra. Another photo-diode (C30617BH EXCELITAS) has a useful area of 100 μm. It can be measured behind the fifth lens (**L5**), where a vertical diameter of 31.3 μm and a lateral diameter of 44.4 μm are calculated.

Both fast photo-diodes have high speed performance up to 25 GHz. The output impedance is 50 Ω. The rise/fall time is 7-14 ps. The spectral range is from 550 nm$\pm$1630 nm. The optical pulse shapes are displayed on the screen of the oscilloscope.

Now we discuss the electrical circuits, power supplies, temperature controllers and oscilloscope used in this setup. The laser diode driver and temperature controller for MO as the experimental setup under CW are used.

As far as the CW currents into the ridge wave-guide sections in the case of the four-section tapered amplifier, the laser diode driver (Model 525B) is used to drive the CW current. The temperature controller (Model 3040, Newport) is used for the tapered amplifier.

A digital pulse and delay generator (Stanford $DG645$) is used to control the delay time between the pulses of optical gate and tapered section. It provides precisely defined pulses at repetition rates up to 10 MHz and can control the timing in 5 ps resolution over the broad range from 0 s to 2000 s. In this work, it is used to control the pulse widths for optical gate and tapered section, and the delay time between each other with an adjustable resolution of 500 ps.

The $TDS754D$ having 500 MHz bandwidth or the 70 GHz sampling scope ($LeCroy\ NRO$ 9000) is used.

Two Hameg HMP 4040 Programmable 4 Channel High Performance Power Supplies are used to supply the DC current for the electrical circuits. The pulse width and amplitude of the current into the tapered section and optical gate can be adjusted by changing the voltage, therefore the current, in these power supplies.

During the measurement of the relevant parameters, i.e. the CW current (set at the diode laser controller), the pulse current (set at the Hameg HMP 4040), delay time (set at the delay generator), the optical output power, the spectra, the pulse shape are measured and recorded by the computer. The software performs all the measurement and plots

in the computer.

4.3 Electrical circuit for high current at ns-pulses regime

The electrical circuits providing ns-pulse currents are developed by Liero et al [65, 78]. For *OG*, an electrical circuit featuring pulse widths of between 0.5 ns and 10 ns and amplitude currents of below 0.5 A is used.

Due to the low input impedance of the diode laser, it is not possible to use impedance-matched transmission lines as interconnections between the diode and the electronic driver. Thus the absolute inductance has to be minimized to keep the parasitic of interconnections.

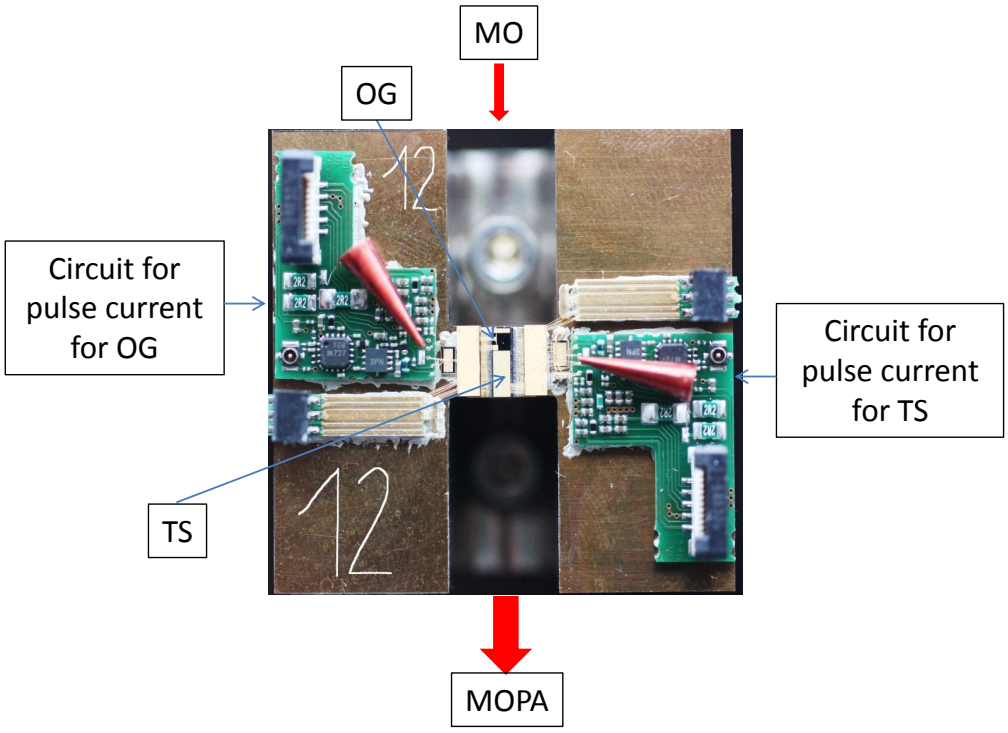

Figure 4.10: The photograph of pulsed driver for optical gate and tapered section

A high frequency *GaN* high-electron mobility transistor is placed as close as possible to the optical gate to ensure fast switching behavior. Additionally, to optimize the load capacitance, the directly bonded chips

to the board (see Fig. 4.10) are close nearby the optical gate.

The electrical circuit used to apply the pulse current for the tapered section is similar to the *OG*. However, it has pulse widths of between 2 and 20 ns and amplitude currents up to 20 A. Therefore, three high-electron mobility transistors are used to amplify the pulse current. It is also needed to minimize interconnection parasitics. Thus it is placed as close as possible to the tapered section, see in Fig. 4.10. More details can be read in ref [78].

5 Wavelength stabilized diode laser based ns-MOPA

In the previous chapters, the motivation of this work and the structure of devices as well as the experimental setups were discussed. In this chapter, the experimental results of high-power diode lasers generating spectral stable, narrow spectral line width operation in the nanosecond range and small amount of the ASE will be shown.

For the monolithic $MOPA$, the (P-I) characteristics and spectra of the tapered section in the ns-pulse regime will be analyzed in order to gain information about the amplified spontaneous emission in the system. To avoid thermal fluctuations and therefore achieve a stable and narrow spectral line width, the MO is driven in CW mode. Optical pulses are then generated by injecting pulsed currents into the OG and TS. Subsequently the time delay adjustment between the pulses of the tapered section and optical gate is discussed, targeting high peak powers and a low amount of ASE. Thereafter the spectral properties of the overall monolithic $MOPA$ will be shown.

Consequently, the hybrid $MOPA$ system the same working principle and time modulation scheme are applied. In the following, both the power-current-voltage characteristics and the spectra are studied for the $RW - DFB$ laser and the tapered section, separately. In order to provide comparability to the monolithic $MOPA$, a corresponding analysis is performed to gain the respect of the need for application.

5.1 Monolithic MOPA

The top view of the monolithic $MOPA$ with the investigated modulation parameters for each section is given in Fig. 5.1.

The DFB section acting as the MO operates in CW mode offering a stable and narrow spectral line width. The second section, the ridge wave-guide section is modulated in pulse mode to transform the CW operation of the DFB section into optical pulses. It acts as an optical gate (denoted OG). The tapered section (denoted TS) is used to amplify the optical pulses. It is operated in pulse mode with a high amplitude and a short width pulse to provide a high intensity and a low amount

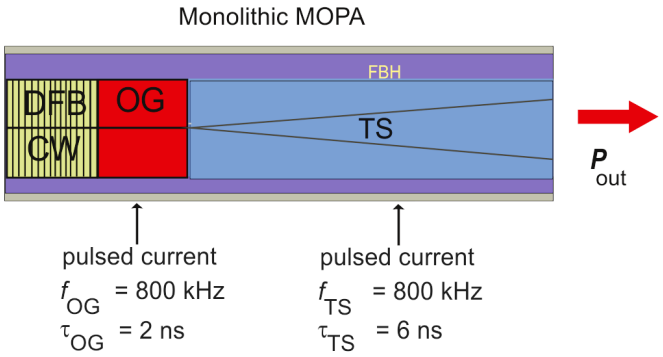

Figure 5.1: Top view of the monolithic $MOPA$ with the investigated modulation parameters for each section

of ASE.

In this section, the amplified spontaneous emission characteristics of the tapered section will be shown. The timing scheme for a high power and a low amount of ASE as well as the spectral properties will be discussed.

5.1.1 Characterization of the tapered section without seeding

At a heat sink temperature of 25°C, no currents are injected into the DFB and RW sections. The injected pulse current into the tapered section (TS) has a pulse length of $\tau_{TS} = 6\,\text{ns}$ and a repetition rate of $f = 800\,\text{kHz}$. The same conditions are used later in the $MOPA$ experiments. The average power depending on the pulsed currents is measured using the experiment setup in Fig. 4.7 and shows in Fig. 5.2 a. It is obvious that two ranges can be distinguished. In the low currents $I_{TS} \leq 4\,\text{A}$ the average power is small, mostly spontaneous emitted photons. The lasing starts at current about 4 A. At above this current, the slope of the output power abruptly increases and at a current of $I_{TS} = 14.5\,\text{A}$, an average output power of 20 mW is obtained.

The spectrum is measured using an optical spectrum analyzer mentioned in section 4.1.2. Fig. 5.2 b shows the spectral behavior of the tapered section at currents of $I_{TS} = 12.5\,\text{A}$, 13.5 A and 14.5 A and resulted in average powers of about 18 mW, 19.5 mW and 20 mW, respectively. The positions in the average power-current characteristic are remarked

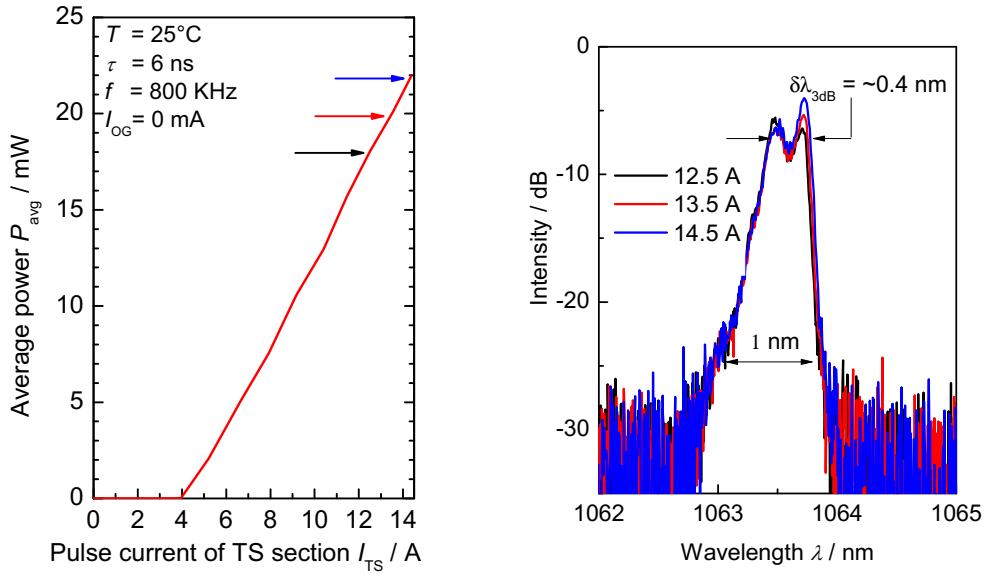

(a) (b)

Figure 5.2: a) Power-current-characteristic for the tapered amplifier at $T = 25°C$ under pulsed operation with $\tau_{TS} = 6\,\text{ns}$ and f =800 kHz.
b) Optical spectrum for the tapered section at $T = 25°C$ under pulsed operation with $I_{TS} = 12.5\,\text{A}$, $13.5\,\text{A}$ and $14.5\,\text{A}$, $\tau_{TS} = 6\,\text{ns}$ and $f = 800\,\text{kHz}$.

with arrows in Fig. 5.2 a. It can be seen that at -3 dB, the full width at half maximum ($FWHM$) in power scale, of the spectrum of about 0.4 nm and the whole range (95%) of about 1 nm are observed.

In fact, when only injected current into the tapered section, a small reflectivity from the DFB section and the RW section is excited by the ASE from the TS section, the device can work as a DBR laser. This leads to a narrow spectrum. The peak wavelength of 1063.5 nm is approximately determined. No saturation was observed.

5.1.2 Timing scheme for high power and low amplified spontaneous emission

After the characterization of the tapered section, now all sections of the $MOPA$ are operated. The target now is to find out the optimal condition with the criteria of a narrow spectral line width, a stabilized

wavelength, a high peak power and a small amount of ASE.

As mentioned earlier the spectral properties of the $MOPA$ systems depend mainly on the spectral properties of the MO. A continuous wave (CW) current is applied into the DFB section for a narrow spectral line width and a stabilized wavelength. The temperature of the heat sink is set at $T = 25°C$ and a current of 150 mA is used.

The optical gate section is used to transform the optical beam in CW mode of the DFB section into optical pulses. It operates in pulse mode. It absorbs the coupled CW beam of the DFB section when no current is injected. When a current pulse with defined width τ_{OG} and amplitude I_{OG} are injected, the OG becomes transparent and during this current pulse the optical beam of the DFB section can pass.

In this experiment, a optical pulsed width of 2 - 3 ns is the target. Therefore a pulse width of 2 - 3 ns is applied into the OG section. The amplitude of the current pulse is selected so that this section becomes transparent. This current depends on the structure of devices and the material of the wave-guide. Here a current amplitude of $I_{OG} = 140$ mA is defined.

In order to obtain a high peak power and a small amount of ASE, the pulse width τ_{TS} has to be carefully selected. It is larger compared to τ_{OG}, but not too long to prevent the generation of amplified spontaneous emission after the wanted optical pulse. Since the time needed to create an inversion population in the upper level, relative to the lifetime of the carriers, i.e, 2 - 3 ns, and the target pulse length is an optical pulse length of about 2 - 3 ns. To allow for this change up time and for the actual pulse length of another 2 - 3 ns, a pulse width $\tau_{TS} = 6$ ns is chosen. Pulse current amplitudes of up to $I_{TS} = 14.5$ A are injected into the TS. The $I_{TS} = 14.5$ A is limited by the available current supply. The electrical circuits for ns pulse currents for both optical gate and tapered section are described in section 4.3.

To find out the best adjustment delay time between τ_{TS} and τ_{OG}, the criteria are a high peak power with an ideally top-hat-like laser pulse shape and a small value of ASE. The repetition rate f of the current pulses injected into both sections (OG and TS) is set to 800 kHz.

The timing scheme is given in Fig. 5.3. At $\tau = \tau_0$ the current pulse

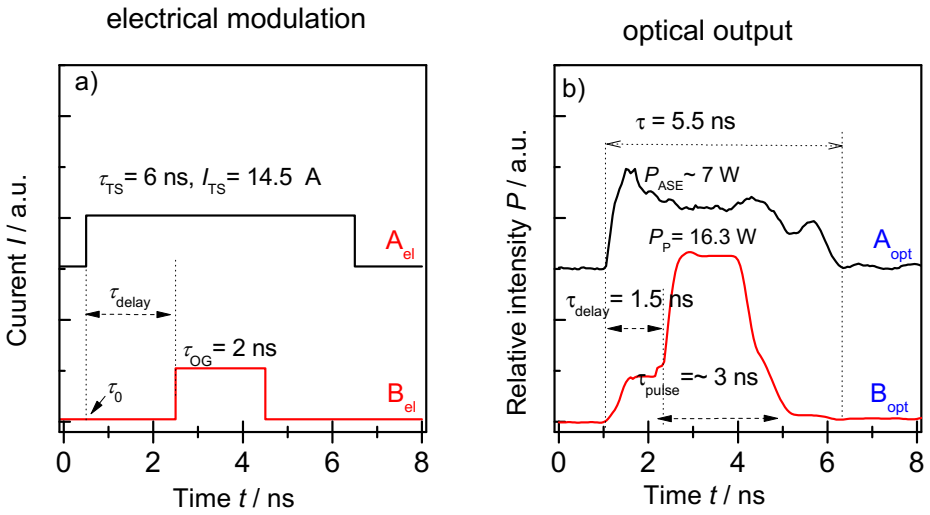

Figure 5.3: Schematic diagram of the electrical modulation of optical gate and tapered section;
a) Electrical modulation, A_{el} shows the pulse current through TS, B_{el} shows the pulse current through OG.
b) Optical output, A_{opt} is optical pulse power without seeder and B_{opt} is optical pulse power with seeder.

with a length of $\tau_{TS} = 6\,\text{ns}$ is injected into the TS. At $\tau = \tau_0 + \tau_{delay}$ the current pulse (B_{el}) with the length $\tau_{OG} = 2\,\text{ns}$ is injected into the OG. The delay time between τ_{TS} and τ_{OG} is varied in 500 ps steps from delay time $\tau_{delay} = 0\,\text{ns}$ to $\tau_{delay} = 2.5\,\text{ns}$. In the upper trace ($A_{opt}$) of Fig. 5.3 b, the dependence of the pulse emission as a function of time without seed laser is shown. The optical pulse is delayed due to cable and optical path lengths. In the case with seed laser, the laser pulse (B_{opt}) is also delayed with respect to the current pulse OG and slightly broadened by about 1 ns due to the time constants of the electronics.

The optical peak power is calculated according to equation 4.1. The behaviors of optical peak power with the different delay time between OG and TS are given in Fig. 5.4. The optical pulse generated by the 6 ns long current pulses with an amplitude of $I_{TS} = 14.5\,\text{A}$ without injected current into the DFB laser and without supplied current into the OG is shown in Fig. 5.4 a. The rise time is about 0.5 ns, the fall time is $\sim 1\,\text{ns}$.

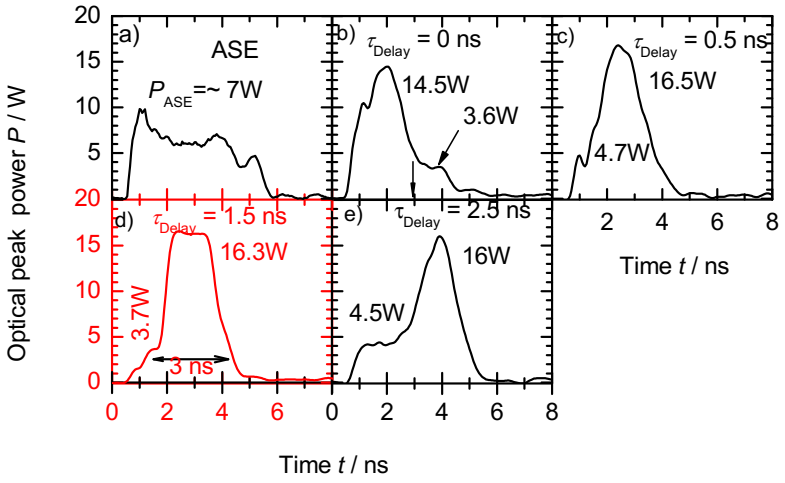

Figure 5.4: The temporal shape of the optical output pulse power without input signal (τ_{TS} = 6 ns, I_{TS} = 14.5 A, I_{DFB} = 0 mA I_{OG} = 0 mA)(a) and with input signal at different delay times τ_{Delay} indicated (b-e) for I_{DFB} = 150 mA, τ_{OG}= 2 ns, I_{OG} = 140 mA, τ_{TS} = 6 ns, I_{TS} = 14.5 A, f = 800 kHz and T = 25°C.

The peak power of 7 W is approximately determined. Figs. 5.4 (b-e) show the optical output pulses when a current of 150 mA is injected into DFB section and the delay time is varied between 0 ns and 2.5 ns. It can be seen that the pulse shape and peak power change significantly for different delay times. For the shortest delay time ($\tau_{Delay} = 0$), a pulse width of about $\tau_{Pulse} = 2$ ns, the peak power was $P_p = 14.5$ W. At the trailing edge of the pulse up to 3.6 W of ASE is observable.

Increasing the delay time to 0.5 ns, the peak power increases to 16.5 W with a length of about 2.5 ns. At the leading edge of the pulse an amount of ASE of 4.7 W is generated. An increase of τ_{Delay} to 1.5 ns leads to a further reduction of ASE to 3.7 W. Moreover, the pulse has now a top hat profile with a pulse length $\tau_{Pulse} = 3$ ns and a nearly plateaued power of 16.3 W. An even longer delay time of $\tau_{Delay} = 2.5$ ns occurs the peak power reduces to 16 W and there is a pronounced emission of ASE at the leading edge of 4.5 W.

If we assume that inside the optical pulse is only emission at the seed wavelength and outside of the pulse is only ASE. Then separate integration inside and outside the optical pulse allows the distinction

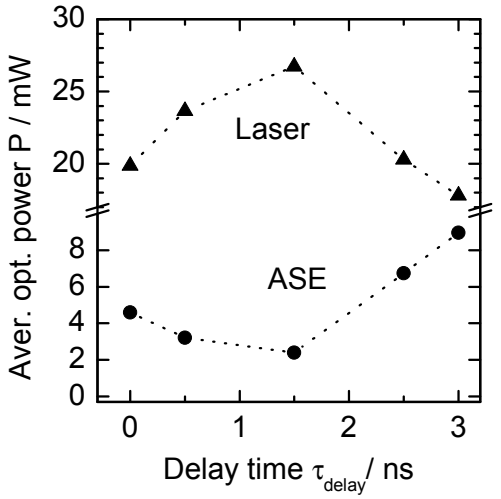

Figure 5.5: Average optical power versus electronic delay time τ_{Delay} for a $\tau_{OG} = 2\,\mathrm{ns}$

between the laser emission and the ASE. Fig. 5.5 shows the dependence of the average pulse power P_{ave} and the ASE power on the delay time. The delay time $\tau_{Delay} = 1.5\,\mathrm{ns}$ is found to deliver the highest average power with $P_{ave} = 26.7\,\mathrm{mW}$ together with the smallest average ASE power $P_{ASE} = 2.4\,\mathrm{mW}$. A percentage of the amount of ASE of about 9% with respect to laser emission can be determined.

It can be explained that for this delay time the maximum excess carrier density in the TS is reached, which results in a maximum amplification of the injected laser pulse. After the passage of the pulse the carrier density is depleted and approaches the transparency carrier density, so that only a small amount of ASE can be generated. When the optical gate pulse occurs too early, the maximum carrier density is not reached and the amplification is reduced. Furthermore, after the passage of the pulse more ASE can be generated (see in Fig. 5.4 b-c). If the optical gate pulse is too late, the ASE is generated already at the beginning of the TS pulse (see in Fig. 5.4 e). Based on these results, it can be stated that the delay time between the OG and the TS of $\tau_{Delay} = 1.5\,\mathrm{ns}$ is best choice for the high peak power, the top hat profile optical pulse and small ASE.

The optical powers at different injected pulse currents of the TS

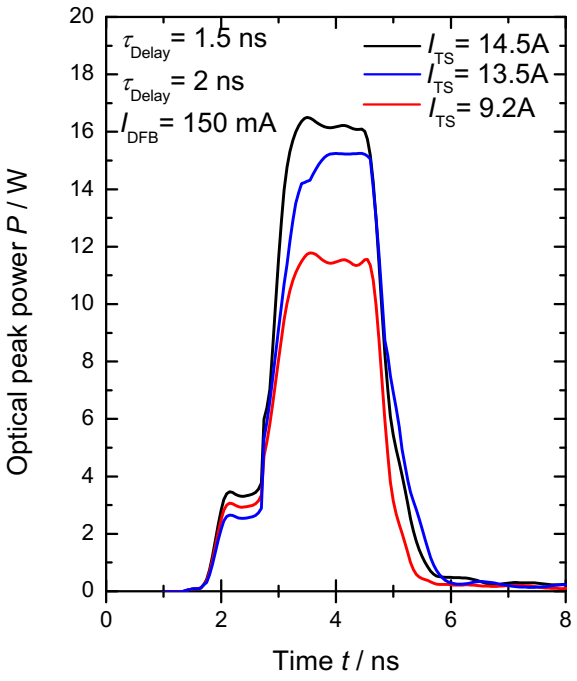

Figure 5.6: The optical powers at the different injected pulse currents into the TS section at $\tau_{Delay} = 1.5\,\text{ns}$, $I_{DFB} = 150\,\text{mA}$, $\tau_{OG} = 2\,\text{ns}$, $I_{OG} = 140\,\text{mA}$, $\tau_{TS} = 6\,\text{ns}$, $f = 800\,\text{kHz}$ and $T = 25°\text{C}$

section are shown in Fig.5.6. Here, it is fixed of $I_{DFB} = 150\,\text{mA}$, $\tau_{Delay} = 1.5\,\text{ns}$, $\tau_{OG} = 2\,\text{ns}$, $I_{OG} = 140\,\text{mA}$, $\tau_{TS} = 6\,\text{ns}$, and $f = 800\,\text{kHz}$. At three pulse currents of 9.2 A, 13.5 A and 14.5 A the optical peak powers of 11.5 W, 15.2 W and 16.3 W, respectively are measured. No saturation can be observed.

5.1.3 Spectral properties

At the delay time of $\tau_{Delay} = 1.5\,\text{ns}$, the optical spectra are measured with increasing the pulse currents of the I_{TS}. A color-scale mapping of the optical spectra of the monolithic $MOPA$ in dependence of the amplitude of the pulsed current injected into the TS section in steps of about 1 A for a fixed $\tau_{Delay} = 1.5\,\text{ns}$, $I_{DFB} = 150\,\text{mA}$, $\tau_{Pulse} = 3\,\text{ns}$, $I_{OG} = 140\,\text{mA}$, $\tau_{TS} = 6\,\text{ns}$, $f = 800\,\text{kHz}$ and $T = 25°\text{C}$ is shown in Fig.5.7.

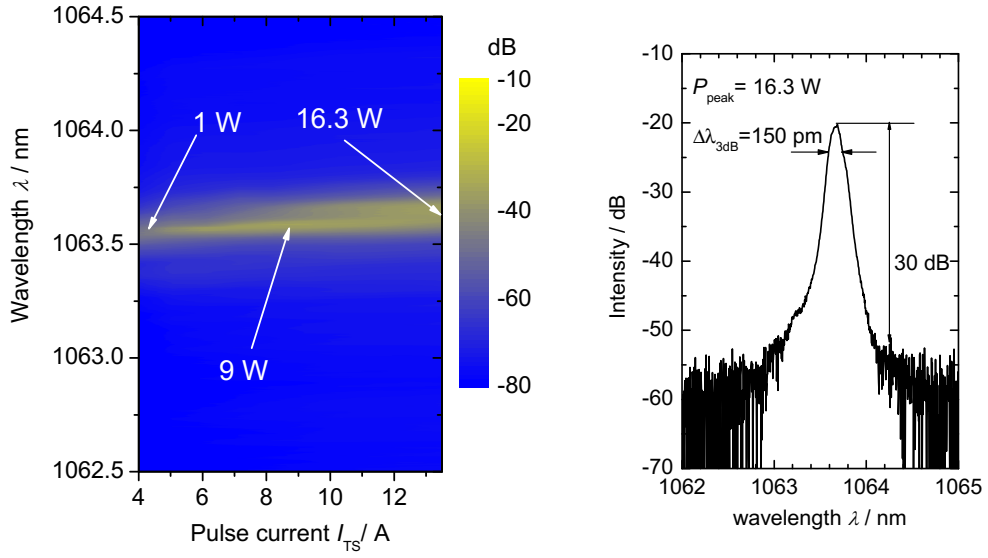

(a) (b)

Figure 5.7: a) Color-scale mapping of the optical spectra of the MOPA in dependence of the amplitude of the current pulses injected into the TS for a fixed DFB laser current of $I_{DFB} = 150\,\text{mA}$, $\tau_{Delay} = 1.5\,\text{ns}$, $\tau_{Pulse} = 3\,\text{ns}$, $I_{OG} = 140\,\text{mA}$, $\tau_{TS} = 6\,\text{ns}$, $f = 800\,\text{kHz}$, and $T = 25°\text{C}$.
b) An optical spectrum of the MOPA system at peak power of 16.3 W

The DFB laser is set at $I = 150\,\text{mA}$ and herewith the seeding peak wavelength is fixed. The spectral width is slightly broader by about 50 pm from 100 pm at the pulse current of 4 A to 150 pm at the pulse current of 14.5 A. At a pulse current of 14.5 A, the spectrum with 16.3 W peak power is given in Fig. 5.7 b. The spectral line width at (-3 dB) is about 150 pm and is smaller than the spectral line width of the tapered section (400 pm) as in Fig. 5.2 b.

The slightly broader emission spectra of the $MOPA$ when increasing the pulsed current of tapered section and the narrow gain profile of TS section can be explained. Without the separation between their sections of the device, the influence of each section to another section can not be prevented. Typically, the tapered section can work as a DBR laser without the injected current into the DFB and OG sections. In this case, the RW can be excited by optical pumping from TS section. Thus the light emission from the TS section can pass to the DFB section,

acting as a Bragg grating to create a resonator and results as a DBR laser.

In refs [79, 80], an identical effect was found. The unstable spectra could be resulting in the uncontrollable optical feedback and coupling of the light emission from the amplifier to the oscillator. The same results in refs [81–83], it was reported that it is difficult to optimize independently due to the integration of both components on one single chip. The optical and thermal coupling could not be prevented. It leads to a fairly complicated dynamic behavior.

A short summary of the monolithic $MOPA$ is that an optical operation in ns-pulse is generated at 1064 nm with the monolithic $MOPA$. The timing delay between the optical gate and tapered section is investigated. The best delay time between the TS and the OG is found. In this case, a peak power of 16.3 W at a pulse width of 3 ns with the top-hat profile is observed. A ratio of the power of the ASE and the laser of 9% is achieved. The spectral line width of 150 pm is obtained. These properties are met the requirement for aerosols detection as mentioned in section 2.1.

To detect the absorption lines of gases, e.g. water vapor, the spectral line width had to be smaller than 10 pm as discussed in section 2.2. Therefore, this spectral line width is not sufficient the requirement. To overcome this problem, a hybrid $MOPA$ concept is demonstrated and presented in the next section.

5.2 Hybrid MOPA concepts

The schematic diagram of the hybrid $MOPA$ system with the investigated modulation parameters for each section is shown in Fig. 5.8. The $RW-DFB$ laser as MO operates in CW, the pulse operation is applied for optical gate and tapered sections. A CW current is injected to make the RW_1 and RW_2 sections transparent, then they work as the optical filters. The characterization of the $RW-DFB$ laser, the tapered section and $MOPA$ system will be presented in the following.

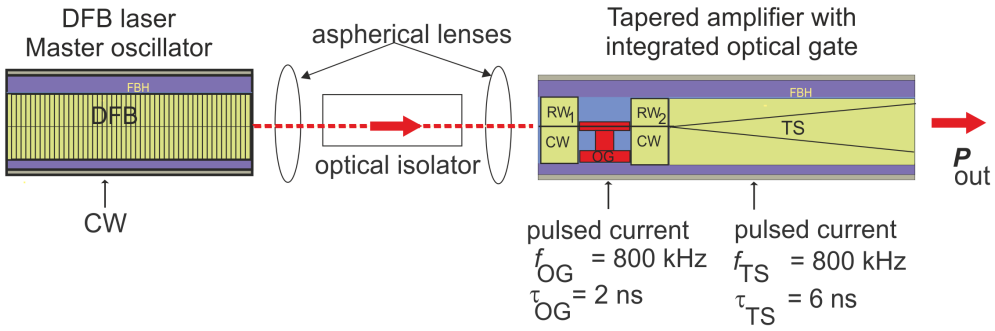

Figure 5.8: Schematic diagram of the hybrid $MOPA$ set-up at 1064 nm.

5.2.1 RW-DFB laser characterization

As mentioned above, the main spectral properties of the $MOPA$ are determined by the MO. The hybrid $MOPA$ system achieves a narrow spectral line width and stabilized wavelength only if the MO provides a narrow spectral line width and a stabilized wavelength. Such properties can be obtained by applying the CW for the $RW-DFB$ laser.

The power-voltage-current PUI characteristics are measured using the setup given in section 4.1.1. Optical output power versus injection current, $P(I)$, and voltage drop across the device versus injection current, $U(I)$, are plotted in the same graph together with the conversion efficiency ($\eta_c(\%)$). Fig. 5.9 a shows $P(I)$, $U(I)$ and $\eta(I)$ of the DFB laser at a temperature of 20°C. The threshold current is $I_{th} = 25\,\text{mA}$. The slope efficiency determined slightly above threshold current is $S = 0.61\,\text{W/A}$. The maximum conversion efficiency is

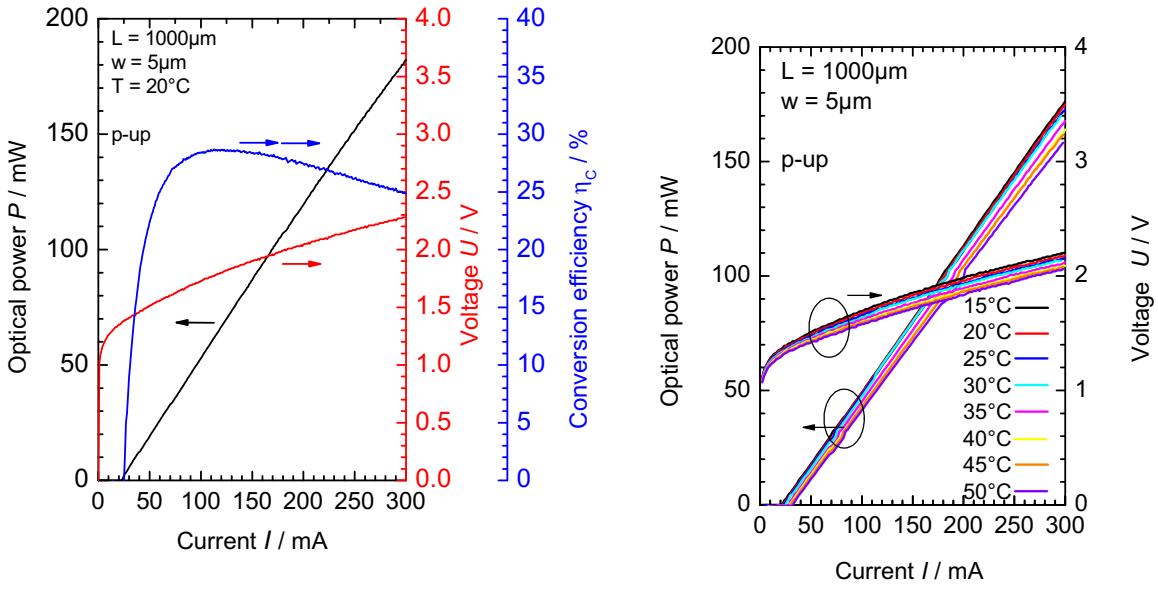

(a) (b)

Figure 5.9: a)Power-voltage-current characteristics for the DFB laser at $T = 20\,°C$. b)Power-voltage-current characteristics for the DFB laser at different temperatures (from $T = 15\,°C$ to $50\,°C$).

29%. A linear increase (PI) of the power versus the current from above threshold current up to 300 mA can be observed. At an injection current of 300 mA the output power is $P = 175\,mW$.

At different temperatures $T = 15 - 50\,°C$, the $PUIs$ are given in Fig. 5.9 b. The threshold currents increase from $I_{th} = 23\,mA$ to 33 mA, the slope efficiency S determined slightly above threshold current varies from $S = 0.62\,W/A$ to $0.59\,W/A$ when changing temperature from $15\,°C$ to $50\,°C$ respectively. At an injection current of 300 mA the output powers are $P = 176\,mW$ at $15\,°C$ and $P = 158\,mW$ at $50\,°C$.

The spectral properties are performed by the experimental setup in section 4.1.2. A color scale mapping of the optical spectra of the DFB laser in dependence on the current at a temperature of 20°C is shown in Fig. 5.10 a. It can be seen that the device operates single mode with a spectral line width below 10 pm for the whole range of current from 30 mA to 300 mA. An optical spectrum measured at $P = 20\,mW$ ($I_{DFB} = 55\,mA$) is given in Fig. 5.10 b. At this output power, later used for

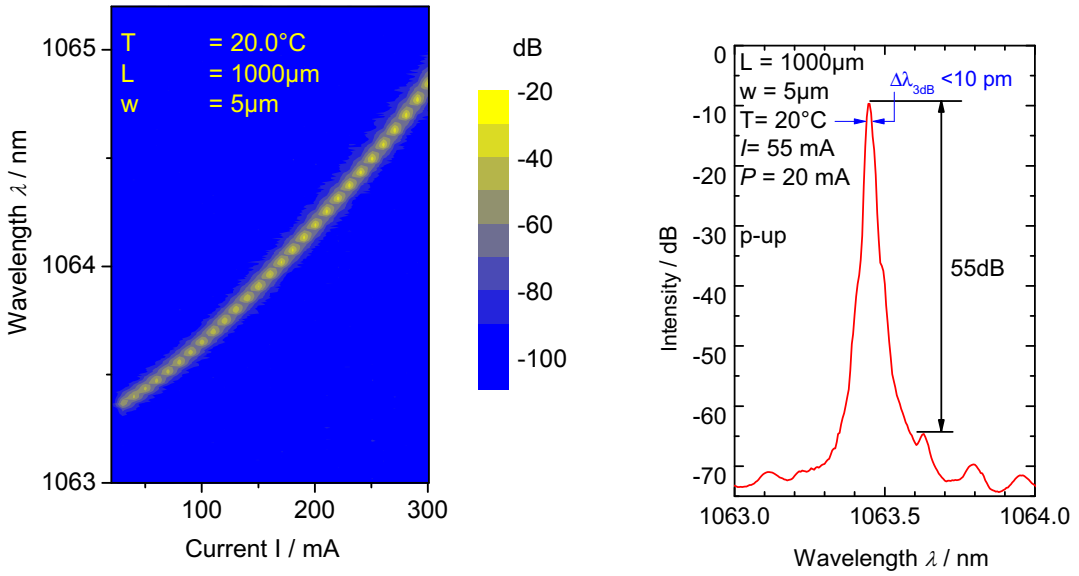

(a) (b)

Figure 5.10: a) Color scale mapping of the optical spectra of the DFB laser in dependence of the current at 20 °C.
b) An optical spectrum of the diode laser at an output power of 20 mW (55 mA)

seeding the tapered amplifier, a $SMSR$ of 55 dB and a spectral line width below 10 pm limited by the spectrum analyzer are observed.

5.2.2 Characterization of the tapered power amplifier under ns-pulse excitation

To compare the hybrid with monolithic $MOPA$ directly, the tapered section (TS) is operated with an electrical pulse width of $\tau_{TS} = 6$ ns and a repetition rate of $f = 800$ kHz. No currents are injected into the RW sub-sections. The power-current-characteristic of the tapered amplifier at heat sink temperature of 25 °C is given in Fig. 5.11 a.

The same conditions are used later in the $MOPA$ experiments. It can be seen that at a current of $I_{TS} = 13.5$ A, an average output power of 7.5 mW is obtained. It is only about 30% when compared to the averaged power of tapered section in monolithic $MOPA$, discussed in 5.1. The same structure of the tapered section (4 mm long gain-guided tapered

section (TS) with a full taper angle of 6°), the same material and the vertical structure of devices are used. From this, it can be supposed that the tapered section of monolithic $MOPA$ could work as a DBR laser, leading to a higher averaged power and a narrow spectrum, as discussed above.

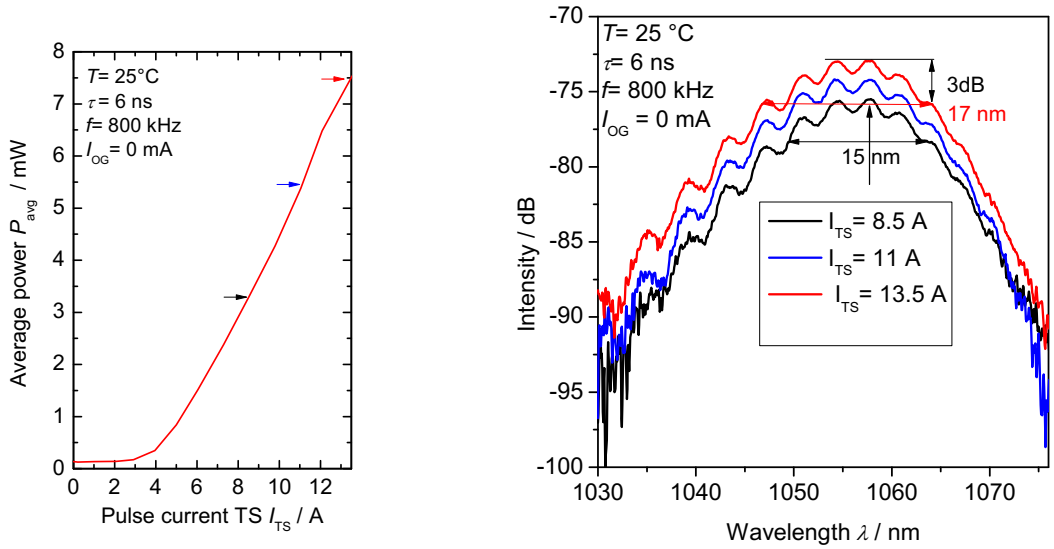

(a) (b)

Figure 5.11: a) Power-current-characteristics for the tapered amplifier at $T = 25\,°C$ under pulsed operation with $\tau_{TS} = 6\,ns$ and $f = 800\,kHz$.
b) Optical spectra of the tapered amplifier from Fig. 5.11 a at $T = 25\,°C$ under pulsed operation with three different currents ($I_{TS} = 8.5\,A$, $I_{TS} = 11\,A$ and $I_{TS} = 13.5\,A$), $\tau_{TS} = 6\,ns$ and $f = 800\,kHz$.

Fig. 5.11 b shows the ASE spectral behavior of the PA at a current $I_{TS} = 8.5\,A$, $11\,A$ and $13.5\,A$ corresponding to the average powers of $3.3\,mW$, $5.4\,mW$ and $7.5\,mW$ as denoted positions by arrows respectively in Fig. 5.11 a.

The ripples in the spectra seen in Fig. 5.11 b are caused by the coupling of the lasing modes to the substrate modes due to the finite thickness of the n-cladding layer. The simulated periodicity of the ripples of $3.3\,nm$, calculation by model developed by Hans Wenzel, agrees quite well with the periodicity seen in the figure of about $3.65\,nm$. The peak wavelength of the ASE spectrum determined from a polynomial fit is

1056.5 nm and indicted with an arrow. No lasing modes are observed. The full width at half maximum (at -3 dB) of the gain profile increases from 15 to 17 nm without shifting the peak wavelength when varying injection current from 8.5 A to 13.5 A. No saturation is observed.

5.2.3 The behavior of optical power and amplified spontaneous emission under delay time

In order to compare the hybrid $MOPA$ with the monolithic $MOPA$, the experiments keep all parameters identical to the previous investigation of the monolithic $MOPA$. To provide a narrow spectral line width and stabilized wavelength, the MO operates at a fixed CW current and temperature. The DFB laser is set at $I_{TS} = 55\,\mathrm{mA}$ and $T = 20\,^{\circ}\mathrm{C}$, leading a power of 20 mW.

The four sections of the tapered amplifier with the integrated optical gate is given in Fig. 5.8. There are three subsections of the ridge waveguide (RW). The first and the third RW sections are denoted RW_1 and RW_2 and used as optical filters. To control the input signal from the MO into the optical gate (OG) section, the RW_1 section is driven with a CW current of about 10 mA. This current makes this section transparency for the laser beam from MO and to avoid large reabsorption in OG section. The same current through the RW_2 section can be assumed transparently for the laser beam from the MO and prevent the light coming from the TS towards the OG section.

The second RW serves as an optical gate denoted OG. It transforms the optical beam in CW mode of the $RW-DFB$ laser to optical pulses. The OG absorbs the coupled CW beam of the DFB laser when no current is injected into this section. And it becomes transparent when sufficient current is applied. The current amplitude to reach transparency depends on the structure of the device and the material of the waveguide. Here, a current amplitude of $I_{OG} = 270\,\mathrm{mA}$ is selected. During the current pulse the optical beam from the MO can pass. The targeted pulse width is 2 - 3 ns, a current pulse width of $\tau_{OG} = 2\,\mathrm{ns}$ is injected into the OG section. For the TS section, a pulse width of $\tau_{TS} = 6\,\mathrm{ns}$ is selected, as above mentioned. It is larger compared to τ_{OG}, but not too

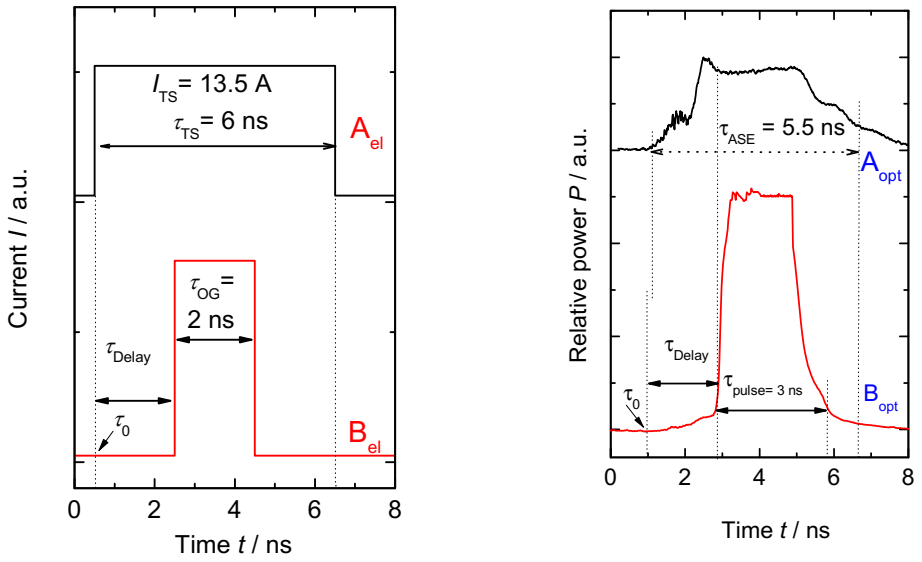

(a) (b)

Figure 5.12: a) Schematic diagram of the electrical modulation of optical gate and tapered section; A_{el} is the current through TS, B_{el} is the current through OG.
b) Resulting optical pulse traces, A_{opt} is the ASE without seeder, B_{opt} is the laser pulse.

long to prevent the generation of amplified spontaneous emission after the desired optical pulse.

Pulses with the amplitudes $I_{TS} \leq 13.5\,\mathrm{A}$ are injected into the TS. The delay time between τ_{TS} and τ_{OG} is varied to find the best adjustment between population of the upper state and laser relaxation. The criteria for the adjustment are a high peak power with a rectangular shape of the laser pulse and a small value of ASE. The repetition rate f of the current pulses injected into both sections (OG and TS) is 800 kHz.

A scheme of the temporal behavior of the electrical pulses is sketched in Fig. 5.12 a. At $\tau = \tau_0$ the current pulse (A_{el}) with a length of about $\tau_{TS} = 6\,\mathrm{ns}$ is injected into the TS. And at $\tau = \tau_0 + \tau_{delay}$, the current pulse ($B_{el}$) with the length τ_{OG} is injected into the OG. The delay time τ_{delay} between the OG and the TS is also varied in 500 ps steps between $0\,\mathrm{ns} \leq \tau_{delay} \leq 3\,\mathrm{ns}$.

The temporal profiles of the optical output pulses were measured by the

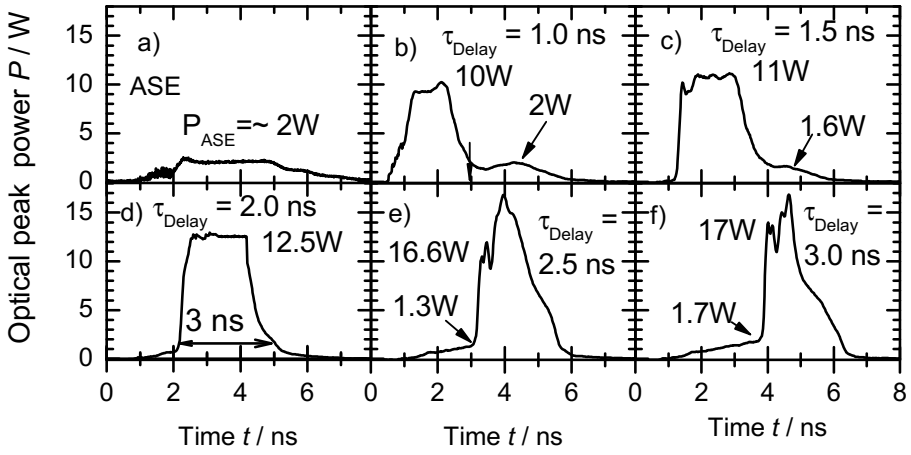

Figure 5.13: The temporal shape of the optical output pulse power without input signal (a) and with input signal ($P_{in} = 20\,\mathrm{mW}$) at different delay times τ_{Delay} indicated (b, c, d, e, f) for $\tau_{OG} = 2\,\mathrm{ns}$, $I_{OG} = 270\,\mathrm{mA}$, τ_{TS}= 6 ns, $I_{TS} = 13.5\,\mathrm{A}$ and f =800 kHz

70 GHz sampling scope (*LeCroy NRO* 9000) as mentioned in section 4.2. In the upper trace (A_{opt}) of Fig. 5.12 b the dependence of the ASE as a function of time without seed laser is shown. In the case with the seed laser, the laser pulse (B_{opt}) is delayed with respect to the current pulse OG and slightly broadened by about 1 ns due to the time constants of the electronics.

As mentioned in the section 4.2, the optical output pulse powers are calculated by the combination of the average power measured by the power meter (*GentecSOLO*2) and the optical output pulse detected by the 25 GHz photo diode (New Focus 1434). The time dependence of the optical output pulse power is calculated by equation 4.1.

Typical temporal shapes of the optical pulses emitted by the $MOPA$ system are given in Fig. 5.13.

Fig. 5.13 a shows the ASE generated by the 6 ns long current pulses with an amplitude of $I_{TS} = 13.5\,\mathrm{A}$ without an input signal from the $RW - DFB$ laser. The rise time is about 0.5 ns, the fall time is about

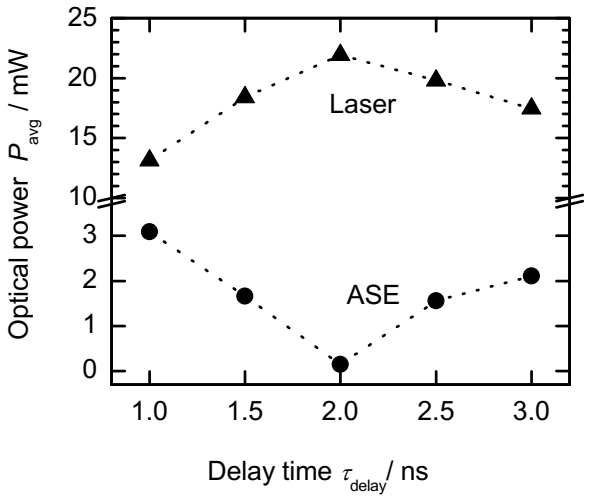

Figure 5.14: Average optical power versus electronic delay time τ_{Delay} for a $\tau_{OG} = 2\,\text{ns}$.

1 ns. The peak power of the ASE is about 2 W. Figs. 5.13 (b-f) show the optical output pulses when the beam from the MO was coupled into the RW section of the PA. The delay time is varied between 1 ns and 3 ns.

It can be seen that for the shortest delay time, the pulse width is $\tau_{Pulse} = 1.5\,\text{ns}$, the peak power is $P_P = 10\,\text{W}$, and at the trailing edge of the pulse up to 2 W of ASE is observable. Increasing the delay to 1.5 ns, the pulse shape becomes more top-hat-like with a length of 2.0 ns. At the trailing edge of the pulse still a large amount of ASE is generated. An increase of τ_{Delay} to 2 ns leads to a further reduction of ASE. Moreover, the pulse has now a top hat profile with a pulse length $\tau_{Pulse} = 3\,\text{ns}$ and a plateau power of 12.5 W. An even longer delay time of $\tau_{Delay} = 3\,\text{ns}$ increase the peak power up to 17 W but there is a pronounced emission (1.7 W) of ASE at the leading edge of the pulse.

The ASE can be calculated with two approaches. As identical to monolithic $MOPA$, it is assumed that inside the optical pulse is only emission at the seed wavelength and outside the pulse is only ASE. From the integrated areas inside and outside of the optical pulses, the average power can be calculated for the laser and the amount of ASE.

Fig. 5.14 shows the dependence of the average power for laser (P_{Laser})

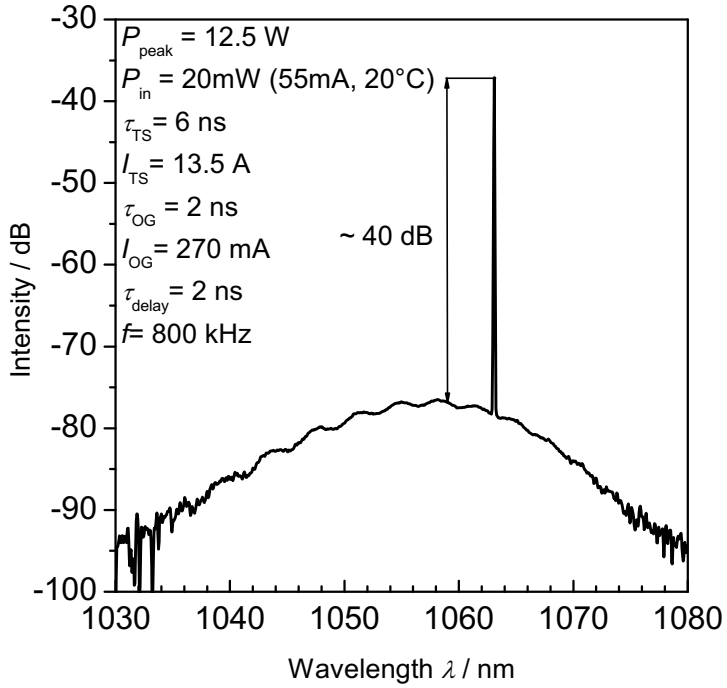

Figure 5.15: Spectrum of the $MOPA$ at peak power of 12.5 W ($P_{in} = 20\,\mathrm{mW}$) at different delay times $\tau_{Delay} = 2ns$, $\tau_{OG} = 2\,\mathrm{ns}$, $I_{OG} = 270\,\mathrm{mA}$, τ_{TS}= 6 ns, $I_{TS} = 13.5\,\mathrm{A}$ and f =800 kHz (Fig. 5.13d) in the range between 1030 nm and 1080 nm.

and the average power for ASE (P_{ASE}) on the time delay. The delay time $\tau_{Delay} = 2\,\mathrm{ns}$ is found to deliver the highest average power measured with $P_{ave} = 22\,\mathrm{mW}$ (corresponding to about 27 nJ pulse energy) together with the smallest average ASE power $P_{ASE} = 0.15\,\mathrm{mW}$. The ratio is $P_{laser}/P_{ASE} = 0.15/22 = 0.007$. It means that the amount of ASE is suppressed to 0.7%. In this delay time the maximum excess carrier density in the TS is reached, which results in a maximum amplification of the injected laser pulse.

After the passage of the pulse the carrier density is depleted and approaches the transparency carrier density, so that only a small amount of ASE can be generated. When the pulse of the OG occurs too early, the maximum carrier density is not reached and the amplification is reduced. Furthermore, after the passage of the pulse more ASE can be generated (see Fig. 5.13 b and c). If the OG is too late, ASE is generated already at the beginning of the TS pulse (Fig. 5.13 e and f).

Within the studied parameter range, a $\tau_{TS} = 6\,\text{ns}$ and $\tau_{Delay} = 2\,\text{ns}$ for $\tau_{OG} = 2\,\text{ns}$ can be assumed as the best choice (Fig. 5.13 d).

Another approach to calculate the amount of ASE is based on spectral profile. In our case, a spectrum was measured in the range between 1030 nm and 1080 nm for the whole range of the gain profile (see in Fig. 5.15). The resolution was 50 pm. It is sufficient to determine the amount of broad band ASE by integration over the whole spectral range. Due to the limited spectral resolution together with the narrow linewidth of the DFB laser of about 1 pm, the same measurement cannot be directly used to determine the amount of laser radiation by integration. The area below the emission line is underestimated. To correct the value one had to assume a certain spectral width of the emission caused mainly by the stability of the set-up. In our case a width of about 1 pm was assumed. Using this estimation an ASE amount below 1% can be deduced for $\tau_{Delay} = 2\,\text{ns}$. This matched well with the estimation based on the pulses shape analysis.

An investigation of different pulse widths of the injected currents into the OG is performed. The peak power and pulse energy in dependence of the optical pulse width τ_{Pulse} for pulses with a top hat profile and minimized ASE (see e.g. Fig. 5.13 d) is shown in Fig. 5.16.

The widths of the optical output pulses are varied by adjusting the width of the current pulses injected into the OG in the range $1\,\text{ns} \leq \tau_{OG} \leq 3\,\text{ns}$. In all cases the delay time is set at $\tau_{Delay} = {}^{(\tau_{TS}-\tau_{OG})}/_{2}$, $\tau_{TS} = 6\,\text{ns}$. The optical gate section is switched transparent when nearly the full population of the excited state is reached. The section is closed shortly before the end of the current pulse at the TS. Using shorter optical gate $\tau_{OG} \leq 2\,\text{ns}$, a slightly higher population of the excited state can be reached and therefore the obtained peak power is higher, as shown in Fig. 5.16.

Nevertheless, the longer times without opening OG section leads to an increase of the ASE up to 1.3%, see in the lower trace of Fig. 5.16. In the case of longer OG pulses $\tau_{OG} \geq 2\,\text{ns}$ the population of the excited level is not completed and therefore the optical power is smaller compared to $\tau_{OG} = 2\,\text{ns}$, and the ASE amount is smaller. The integrated optical pulse powers, corresponding to pulse energy is given. The pulse energy

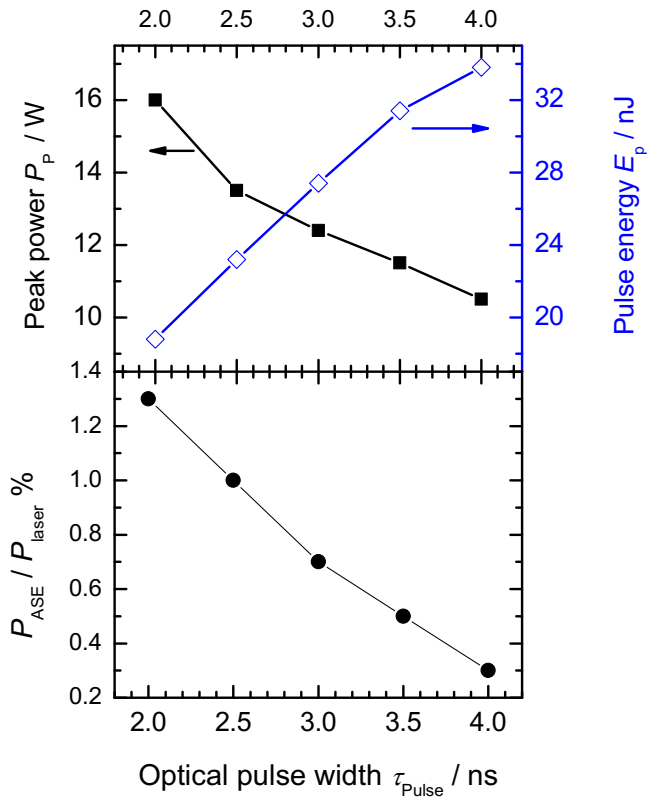

Figure 5.16: Peak power P_p (left axis), pulse energy E_p (right axis) and the ratio of amount of ASE and laser versus pulse width τ_{Pulse} for $I_{OG} = 270\,\text{mA}$, $\tau_{TS} = 6\,\text{ns}$, $I_{TS} = 13.5\,\text{A}$, $f = 800\,\text{kHz}$.

increases from 19 nJ to 34 nJ as shown in the right axis in Fig. 5.16.

In all experiments, the current pulse amplitude through the tapered section is limited to 13.5 A. Up to this current amplitude no saturation of the output power is observed. From the measured power-current characteristics a further increase of the output power seems to be possible if the current (both the amplitude and the pulse width) could be increased.

5.2.4 Spectral properties

The optical spectra of the DFB laser at the power of 20 mW and the $MOPA$ system at the delay time of $\tau_{Delay} = 2\,\text{ns}$, $\tau_{OG} = 2\,\text{ns}$,

$I_{OG} = 270\,\text{mA}$, $\tau_{TS} = 6\,\text{ns}$, $I_{TS} = 13.5\,\text{A}$, $P_{in} = 20\,\text{mW}$, $f = 800\,\text{kHz}$ are compared in Fig. 5.17 a, measured at the same range and the same resolution.

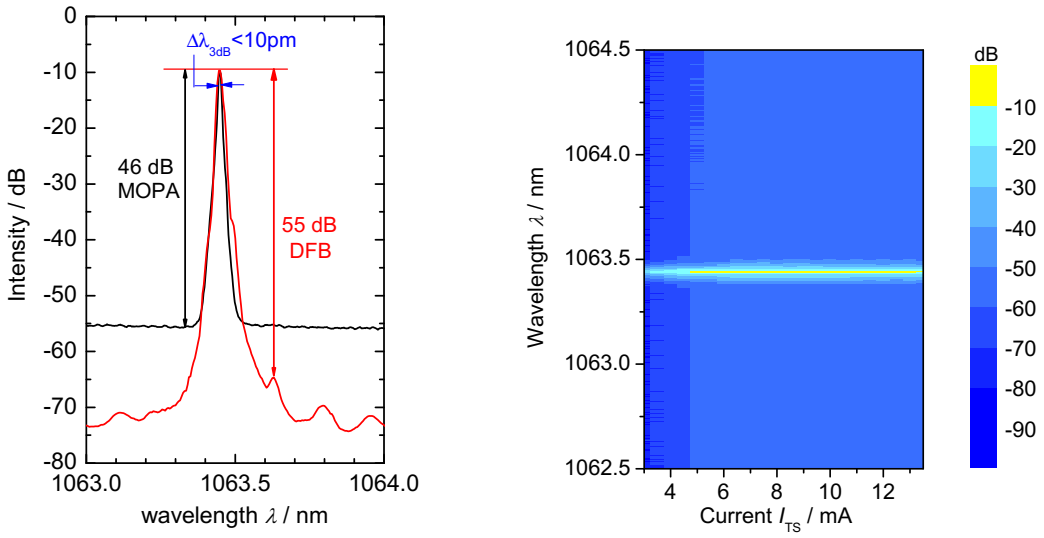

(a) (b)

Figure 5.17: a) Optical spectra of the DFB laser (CW, $P = 20\,\text{mW}$) and the $MOPA$ system at for $\tau_{Delay} = 2\,\text{ns}$, $\tau_{Pulse} = 3\,\text{ns}$, $I_{OG} = 270\,\text{mA}$, $\tau_{TS} = 6\,\text{ns}$, $I_{TS} = 13.5\,\text{A}$, and $f = 800\,\text{kHz}$.
b) Color-scale mapping of the optical spectra of the $MOPA$ in dependence of the amplitude of the current pulses injected into the TS for a fixed input power DFB (CW, $P = 20\,\text{mW}$) ($I_{DFB} = 55$ mA, $T_{DFB}= 20\,°\text{C}$) and $\tau_{Delay} = 2\,\text{ns}$, $\tau_{Pulse} = 3\,\text{ns}$, $I_{OG} = 270\,\text{mA}$, $\tau_{TS} = 6\,\text{ns}$, $I_{TS} = 13.5\,\text{A}$, and $f = 800\,\text{kHz}$.

The peak wavelength of $\lambda = 1063.45\,\text{nm}$ and the measured spectral full width maximum (at - 3 dB) of 10 pm given by the resolution limit of the optical spectrum analyzer coincides for the DFB laser and the $MOPA$. The DFB laser has a side mode suppression ratio ($SMSR$) of 55 dB whereas the $SMSR$ of the $MOPA$ is deteriorated to 46 dB indicating the ASE contribution.

The dependence of the optical spectra on the current I_{TS} as a color-scale mapping is shown in Fig. 5.17 b. The DFB laser is operated at $I = 55\,\text{mA}$, $T_{DFB}= 20\,°\text{C}$ and herewith the seeding peak wavelength is fixed. Over the whole range of TS currents the peak wavelength of the

$MOPA$ does not vary and the spectral width remains $\leq 10\,\mathrm{pm}$.

5.3 Conclusion

It can be shortly summarized, that nanosecond optical pulses at a wavelength of about 1064 nm are generated by a monolithic and a hybrid $MOPA$ system. The monolithic $MOPA$ provides a stable wavelength and a peak power of 16.3 W with a nearly rectangular pulse shape at a pulse width of 3 ns and a repetition rate of 800 MHz, by adjusting the time delay between OG and TS. At this peak power, a spectral line width of about 150 pm is observed. A ratio between the powers of the ASE and the Laser of 9% is estimated. These properties fulfill the requirements for detection of aerosols, however the spectral line width is not sufficient for the detection of absorption line of the gases, e.g water vapor. In order to achieve even narrower spectral line widths the hybrid $MOPA$ system with separated chips for the MO and the PA had to be used.

Hybrid $MOPA$ systems offers a stable, spectral line width of below 10 pm and a side mode suppression ratio ($SMSR$) larger than 46 dB. A peak power of 16 W at a pulse width of 3 ns is achieved at a repetition rate of 800 MHz. An amount of ASE smaller than 1%, a high spectral purity is guaranteed, which provides a decreased error in measurements. This system features a drastic improvement in terms of spectral line width and the amount of ASE which are now sufficiently narrow for the detection of absorption lines of molecular species under atmosphere condition. To detect the absorption line of water vapor the spectral regions needs to be considered for targeted measured range. In next chapter, an identical hybrid $MOPA$ system transfers to another wavelength, where the absorption lines of water vapor located will be presented.

6 Tunable wavelength ns-MOPA diode lasers

In the previous chapter, the hybrid $MOPA$ systems with stabilized wavelength emission wavelength at 1064 nm were presented. In this chapter, a hybrid $MOPA$ system operates at wavelength of 975 nm, where a potential spectral region of water vapor is located.

The challenges now are not only to obtain a spectral line width below 10 pm and a peak power of more than 10 W, but also a continuous tunable emission wavelength for scanning over some absorption lines of the water vapor.

A continuously tunable light source can allow the access to some water vapor absorption lines with different strengths. This is particularly important for concentration calibration, adjusting the working points and the selection of suitable absorption lines.

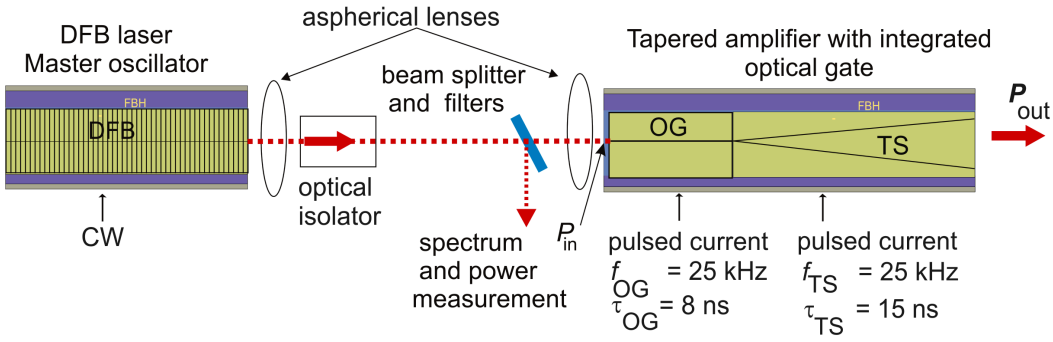

Figure 6.1: Schematic diagram of the hybrid $MOPA$ set-up operation at 975 nm with the studied modulation parameters for each section.

As mentioned above the repetition rate and pulse width determine the measured range and resolution of $LIDAR$ systems. A repetition rate of 25 kHz, i.e., a time between two pulses of 40 μs corresponds to a measuring range of 6000 m. A response time of 8 ns corresponds to a resolution of 1.2 m. Therefore, a repetition rate of 25 kHz and a pulse width of 8 ns are now applied. The scheme of the hybrid $MOPA$ setup with the studied modulation parameters for each section is given in Fig. 6.1. The $RW - DFB$ laser used as MO was operated in CW mode. Two section tapered amplifier consists of OG and TS sections

and both of them are driven in pulse currents.

Characterization of the $RW-DFB$ laser such as the power-current-voltages and the spectral properties will be given. The properties of amplified spontaneous emission of the tapered section will be pointed out. Then the dependence of the output powers on input power as well as the spectral properties of the hybrid $MOPA$ system will be discussed. Finally, a specific stabilized wavelength with a constant spectral line width at an online water vapor absorption line will be shown.

6.1 Tunable RW-DFB laser

In order to provide a light source with a narrow spectral line width, single mode operation and possible tuning, the MO should be operated in single mode emission and can be tuned by either current or temperature. For this target, the $RW-DFB$ laser having a cavity

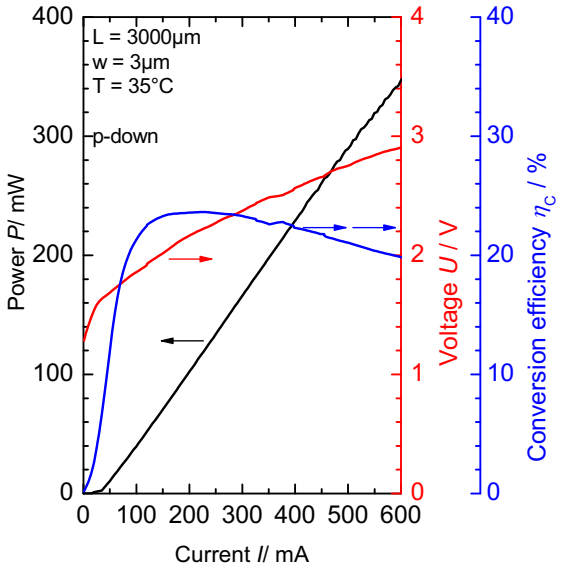

Figure 6.2: The power-current-voltage characteristics of the DFB laser at $T = 35\,°\mathrm{C}$.

length of $L = 3\,\mathrm{mm}$ and a ridge width of $w_{RW} = 3\,\mu\mathrm{m}$ is used. It is mounted p-side down on a C-mount for better heat dissipation and operated in CW mode. The power-voltage-current characteristics are shown in Fig. 6.2 at $T = 35\,°\mathrm{C}$. This temperature is set to provide the explicit

tuning range, where the water vapor absorption lines are located. The scanning over several absorption water vapor absorption lines will show later. At this temperature, the threshold current is about 40 mA. At an injection current of 600 mA an output power of $P = 340$ mW is emitted. The slope efficiency S determined slightly above threshold current is $S = 0.62$ W/A. A maximum conversion efficiency of 24% is obtained at 200 mA.

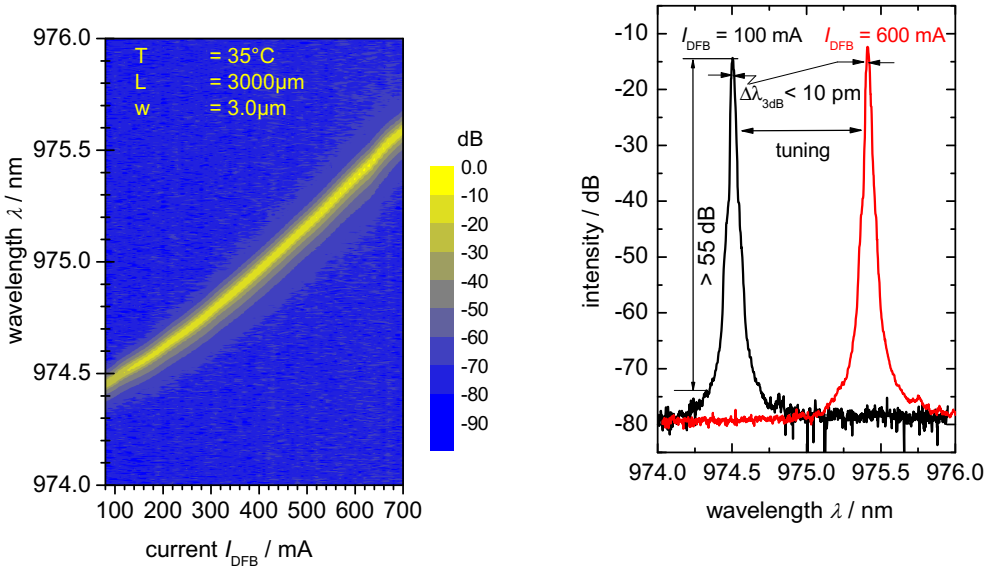

(a) (b)

Figure 6.3: a) Color scale mapping of the optical spectra of the DFB laser in dependence of the current at the temperature of $T = 35\,°C$.
b) Optical spectra at two operating points ($I_{DFB} = 100$ mA and 600 mA).

The optical spectra are also measured with the spectrum analyzer (*Advantest Q*8384). The dependence of the optical spectra on the injection current is shown in Fig. 6.3 a as a color scale mapping. It can be seen that a single mode operation without mode hopping is obtained over a tuning range of about 1.3 nm by varying the current from 80 mA to 700 mA. Two spectra at 100 mA (40 mW) and 600 mA (340 mW) at $T = 35\,°C$ are shown in fig. 6.3 b. The peak wavelengths are 974.50 nm and 975.40 nm respectively. This tuning range is used for $MOPA$ system, which covers some absorption lines of the water vapor. It will be shown

later. The side mode suppression ratio exceeds 55 dB in both cases. The DFB laser operates in single mode with a spectral line width smaller than 10 pm. The spectral line width remained below 10 pm and is limited by the resolution of the spectrum analyzer. Its properties are suitable for further experiments as a seed laser, which offers a continuously fine tuning.

6.2 Amplified spontaneous emission under ns-pulse excitation

The structure of the two-section tapered amplifier is given in Fig. 3.8. Now the spectral properties and power behavior under ns-pulse excitation is given.

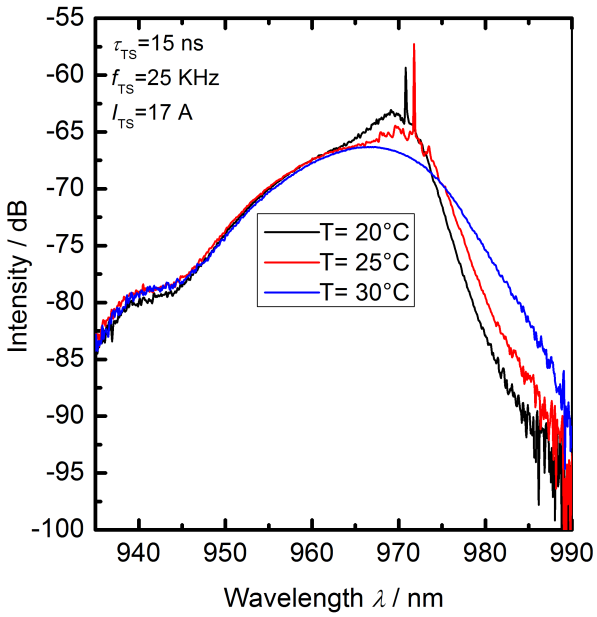

Figure 6.4: The ASE spectra of the TS section at I_{TS}= 17 A, τ_{TS} = 15 ns, f = 25 kHz at different temperatures (T = 20 °C, T = 25 °C and T = 30 °C).

The pulse width of τ_{TS} = 15 ns and a repetition rate of f = 25 kHz are selected for the TS section. The ASE spectra of the TS section at different temperature of the heat sink are measured. In Fig. 6.4 shows the ASE spectra of the TS section at I_{TS}= 17 A, τ_{TS} = 15 ns, f = 25 kHz at different temperatures (T = 20 °C, T = 25 °C and T =

30 °C). It is seen that at the current of I_{TS}= 17 A, τ_{TS} = 15 ns, f = 25 kHz, the self-lasing is obvious at the temperatures of $T \leq 25$ °C. At the temperature of $T = 30$ °C, the ASE spectrum does not appear the self-lasing. To avoid the self-lasing, further investigation a heat sink temperature of 30 °C is set.

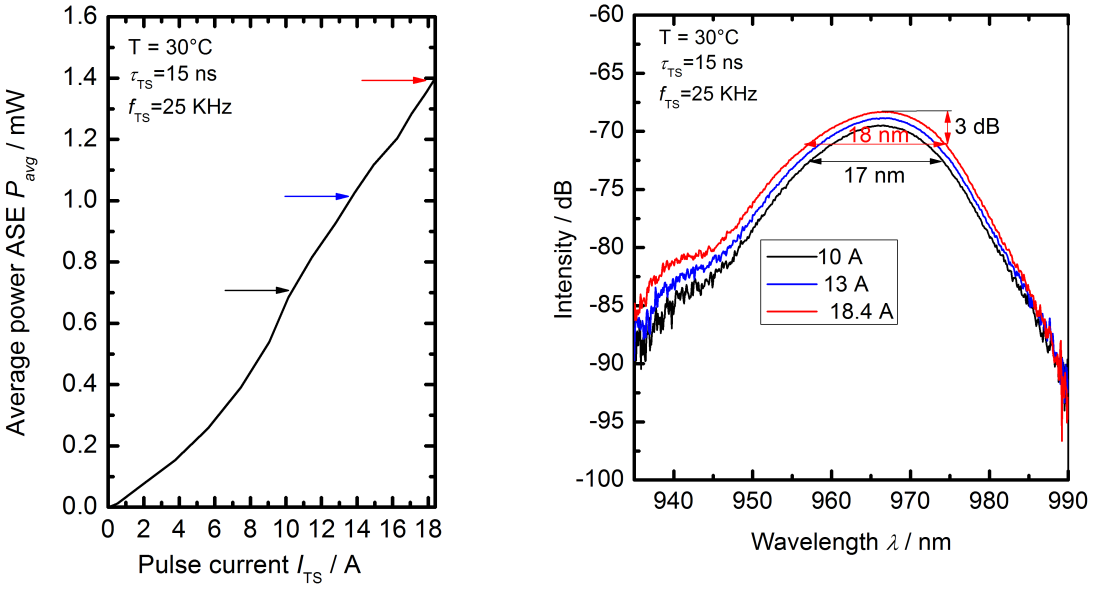

(a) (b)

Figure 6.5: a) Power-current characteristic for the tapered section of the amplifier at T = 30 °C under pulsed operation with τ_{TS} = 15 ns, f = 25 kHz.
b) Spectra of the amplified spontaneous emission at I_{TS}= 10 A, 13 A and 18.4 A, τ_{TS} = 15 ns, f = 25 kHz.

The heat sink temperature is set to 30 °C. The power current characteristic is given in Fig. 6.5 a. A maximal average output power of 1.40 mW is obtained at an amplitude of I_{TS} = 18.4 A with a length of τ_{TS} = 15 ns, a repetition rate of f = 25 kHz.

At the pulsed currents of 10 A, 13 A and 18.4 A leading in average powers of 0.60 mW, 0.95 mW and 1.40 mW, respectively are obtained. The position in the power current characteristic are marked with arrows in Fig. 6.5 a. The respective ASE spectra are given in Fig. 6.5 b. The peak wavelength of the ASE spectrum is constant at about λ = 969 nm. The full width half maximum (-3 dB) of the spectra increases slightly

from 17 nm to 18 nm when increasing the current from 10 A to 18.4 A, a higher current circuits compared with the previous chapter. No lasing modes are observed.

6.3 Dependence of output powers on input powers, saturation behavior

In the previous section, the MO laser and the TS section of the tapered amplifier were characterized, both of them are suitable for further investigate. Now, the hybrid $MOPA$ system is studied. As mentioned above, the MO is driven by the CW current. The OG and TS are applied by pulse currents. A pulse width of 8 ns and a repetition rate

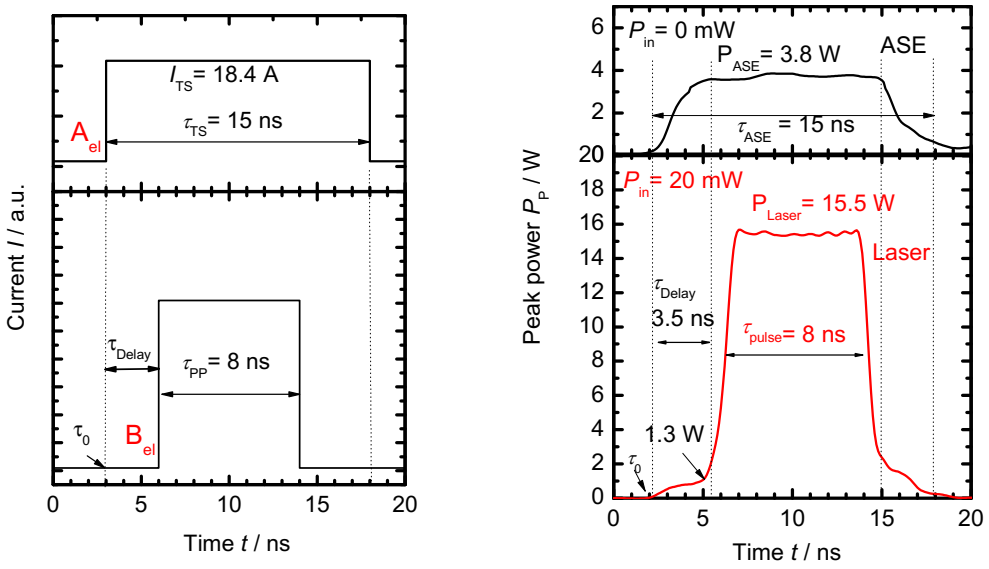

(a) (b)

Figure 6.6: Schematic diagram of the electrical modulation of optical pulse and tapered section;

a) The symbol A_{el} represents the current through TS and the B_{el} is current through OG.

b) Temporal shape of the optical output pulse power for P_{in} = 20 mW, τ_{Delay} = 3.5 ns , τ_{OG} = 8 ns, I_{OG}= 100 mA, τ_{TS} = 15 ns, I_{TS}= 18.4 A and f = 25 kHz.

of f= 25 kHz are targeted as mentioned above. Thus, the pulses with a width of 8 ns at a repetition rate of 25 kHz are applied for the OG.

The pulsed current amplitude of the OG is set at the current where this section becomes transparent and then the laser beam from the MO can pass. This amplitude depends on the structure of devices and the material of the wave guide. A current amplitude of $I_{OG} = 100\,\mathrm{mA}$ is defined.

As the target is a high optical power laser and a low amount of ASE, the pulse width of the TS section has to be considerated. As the previous chapter mentioned that the pulse of the TS section has to long enough for building up the inversion population in the upper level and short to prevent the generation of the ASE after the wanted optical pulse. A pulse width of $\tau_{TS} = 15\,\mathrm{ns}$ is selected. In the upper trace in the Fig. 6.6 b, the measured ASE power at an amplitude current of 18.4 A and a pulse width of $\tau_{TS} = 15\,\mathrm{ns}$ is plotted. It can be seen that it needs about 3.5 ns to reach the steady carrier state density, related to the carrier lifetime [84], and the same time for depopulation the carrier density can be observed. This means that a pulse width of 15 ns is reasonable for a high peak power and a low amount of ASE. An optical peak power of about 15.5 W at 8 ns pulse width with a repetition rate of 25 kHz is obtained, as shown in fig. 6.6 b (in the lower trace).

Therefore, in further experiments, the pulse width of $\tau_{TS} = 15\,\mathrm{ns}$ for the TS, the pulse width of $\tau_{OG} = 8\,\mathrm{ns}$ with the current amplitude of $I_{OG} = 100\,\mathrm{mA}$ for the OG and the delay time between the TS and the OG of $\tau_{Delay} = 3.5\,\mathrm{ns}$ are used.

The transient shapes of the optical output power at different input powers are shown in Fig. 6.7. The optical pulse without the input (ASE) has a pronounced plateau with a pulse width of about 11 ns and a power amplitude of 3.8 W. The rise and fall times determined from 10% and 90% of the pulse are 2.2 ns and 2 ns, respectively (Fig. 6.7 a). Figs. 6.7 b-h show the optical output pulses at different input powers varied between 5.3 mW (Fig. 6.7 b) and 50 mW (Fig. 6.7 h). It can be seen that the optical peak power increases from 10 W to 15 W when the input power is increased from 5.3 mW to 15 mW (Figs. 6.7 b-e) and reaches a constant output power of 16.3 W for larger input power (Fig. 6.7 f-h). The pulse width as well as rise and fall times are almost unchanged. A small ripple observed at the top of the optical pulse may be caused by unwanted

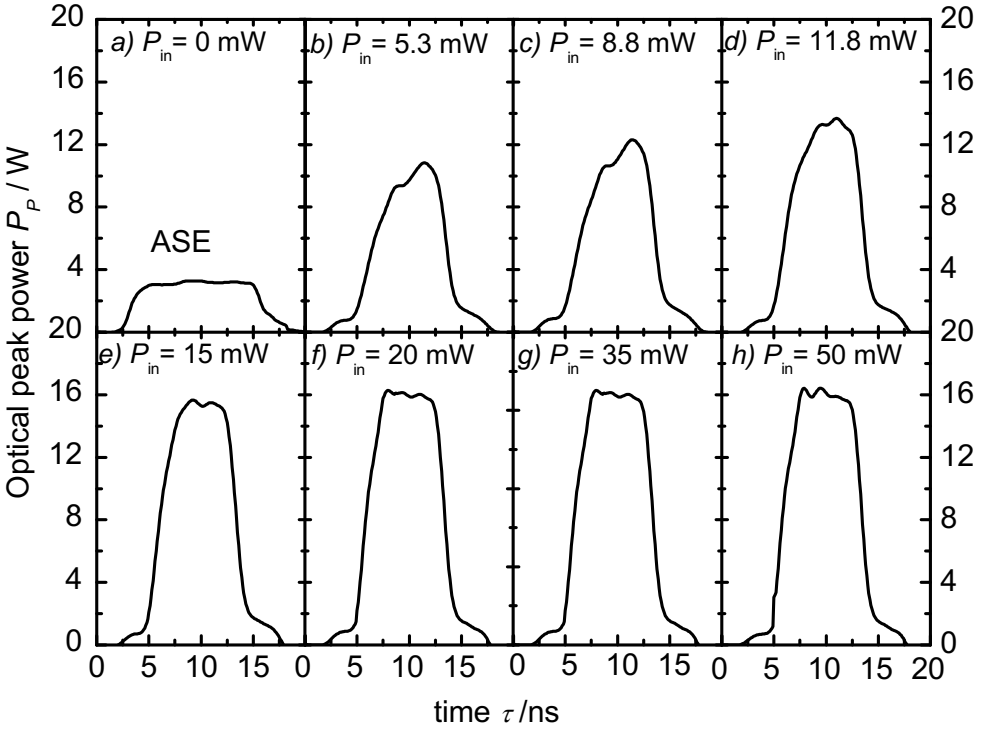

Figure 6.7: Temporal pulse shapes emitted by the $MOPA$ when the MO is turned off (a) and for different input powers (P_{in}= 5.3 mW (b), 8.8 mW (c), 11.8 mW(d), 15 mW (e), 20 mW (f), 35 mW (g) and 50 mW (h), for τ_{Delay} = 3.5 ns, τ_{OG} = 8 ns, I_{OG}= 100 mA, τ_{TS} = 15 ns, I_{TS}= 18.4 A and f = 25 kHz.

feedback effects. At the beginning and the end of the amplifier pulse the pedestals indicate contributions due to ASE.

The dependence of output power on input power can be tested by changing the injected current into the $RW-DFB$ laser. It can be seen in Fig. 6.2 that the input power from the MO increases from 40 mW at 100 mA to 340 mW at 600 mA. They are too large which saturate the tapered section. Neutral density filters are used to reduce the input power. And a beam splitter 50:50 (Thorlabs, $BS014$) is used to divide the beam into two parts. One part is focused into the RW section (P_{in}). Another part is sent to a power meter or an optical spectrum analyzer (OSA) for monitoring the power and spectrum, respectively.

The dependence of the output power on the input power with different injected currents into the TS is measured. Fig. 6.8 shows the dependence

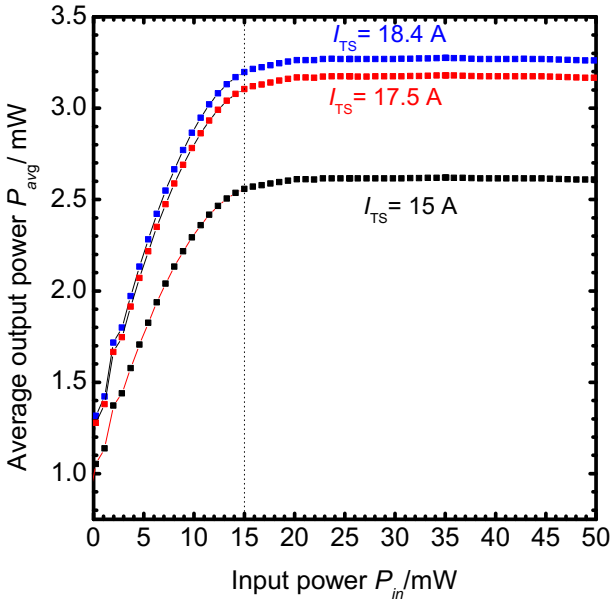

Figure 6.8: The dependence of the average power on the input power.

of the average output power on the input power at three different currents into the TS section. It can be seen that the average output powers increase with the input powers in the range of $0\,\mathrm{mW} \leq P_{in} \leq 15\,\mathrm{mW}$. Above 15 mW the output powers saturate with only a marginally increase in average optical output power when increasing the input power from 15 mW to 50 mW. At three different currents into the TS section, a similar behavior of the dependence of the output power on the input power is observed. A higher average output power can be achieved at a higher current into the TS. For reliability of the devices, a maximal pulse current of $I_{TS} = 18.4\,\mathrm{A}$ is applied. At this pulsed current, the maximum average power of 3.26 mW can be observed, corresponding to an optical peak power of 16.3 W.

In order to calculate the amount of ASE, in the previous chapter based on the measured optical powers it was assumed that inside the pulse is the optical laser emission and outside of the pulse is the ASE. Now, we use the model developed by Ulm *et al.* [66, 85] to determine of the amount of ASE. The measured results of the dependence of the optical output power on the input power at the pulse current of 18.4 A of the TS section is plotted as black circles in Fig. 6.9. It is the total

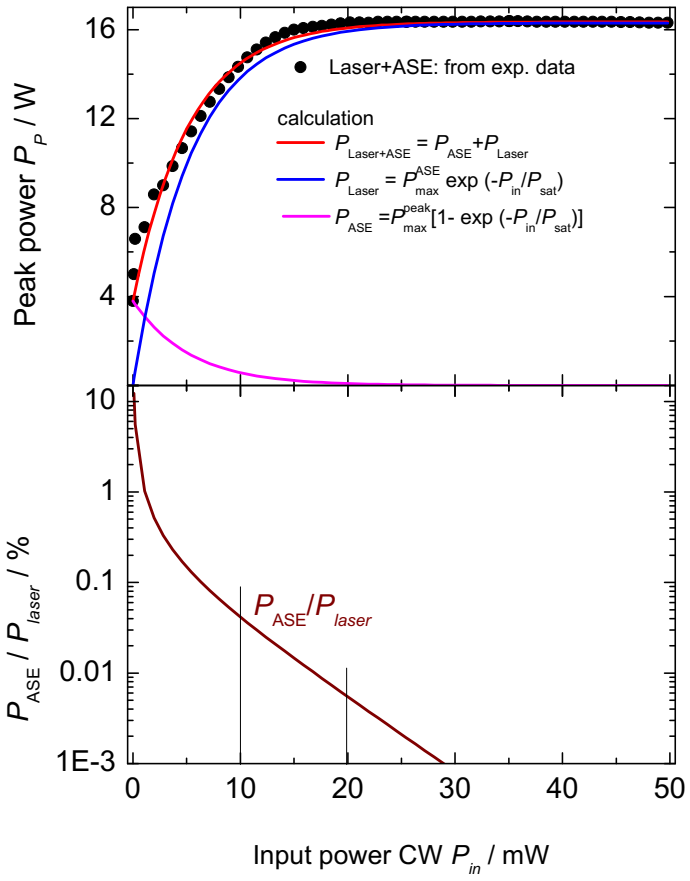

Figure 6.9: Optical peak power versus input power for $\tau_{Delay} = 3.5\,\text{ns}$, $\tau_{OG} = 8\,\text{ns}$, I_{OG}= 100 mA, $\tau_{TS} = 15\,\text{ns}$, I_{TS}= 18.4 A and $f = 25\,\text{kHz}$ from the experimental results (black circle); The calculated databases by using equations 6.1, 6.2 and 6.3 for curve fitting for both laser and ASE (red curve), the ASE (magenta curve), the laser (blue curve) and the ratio of amount ASE and laser (wine curve) are given.

optical power included of the laser power and the ASE. The saturation power P_{sat} can be determined by using the following formula [66, 85].

$$P_p = P_{max}^{ASE} \cdot \exp\left(-P_{in}/P_{sat}\right) + P_p^{max} \cdot \left[1 - \exp\left(-P_{in}/P_{sat}\right)\right] \qquad (6.1)$$

Where $\mathrm{P}^{\mathrm{ASE}}_{\mathrm{max}}$ is the experimental result shown in Fig. 6.7 a (= 3.8 W) without seed laser and the saturated output power of 16.3 W with seed laser is used. This leads to a saturation input power of $P_{sat} = 5.3\,\text{mW}$.

And the ASE power decreases with increasing input power according to

$$P_{ASE} = P_{max}^{ASE} \cdot \exp\left(-P_{in}/P_{sat}\right) \tag{6.2}$$

Whereas the laser power increases as

$$P_{Laser} = P_{p}^{max} \cdot \left[1 - \exp\left(-P_{in}/P_{sat}\right)\right] \tag{6.3}$$

In the upper trace of the Fig. 6.9, the red, the magenta and the blue curves are plotted based on the calculation using equation 6.1 for the total power (both the laser power emission and the ASE), using equation 6.2 for the amount of ASE and using equation 6.3 for the laser power emission, respectively. Then the ratio between the amount of ASE and the power of laser emission is plotted in the lower trace. It can be seen that above input powers of 10 mW an amount of the ASE is below 0.1%. In the previous chapter two methods for calculating of the amount of the ASE are used. One method is based on the spectra and another method assumed that inside the pulse is the optical laser emission and outside of the pulse is the ASE. At the input power of 20 mW, the ratio between of ASE and laser is 0.7%. Now, its ratio is 0.1%. Both values are smaller than 1% and agree very well. It is the proof to approve the previous assumption.

6.4 Spectral tuning properties

The optical spectra of the $RW-DFB$ laser and of the hybrid $MOPA$ are measured for various injected currents into the $RW-DFB$ laser. Here it is fixed values of τ_{Delay} = 3.5 ns, τ_{OG} = 8 ns, I_{OG}= 100 mA, τ_{TS} = 15 ns, I_{TS}= 18.4 A and f = 25 kHz. In Fig. 6.10, a comparison of the optical spectra of the MO (lower graph) and the $MOPA$ system (upper graph) are given. Here, the injected currents of the $RW-DFB$ laser increase from 100 mA to 600 mA for both cases. The input powers change from 5.3 mW to 50 mW.

In the case of hybrid $MOPA$, the optical output power of 16.5 W is approximately constant over the tuning range. The peak wavelengths tune from 974.50 to 975.40 nm and the measured spectral full widths at 3 dB of 10 pm given by the limited resolution of the optical spectrum

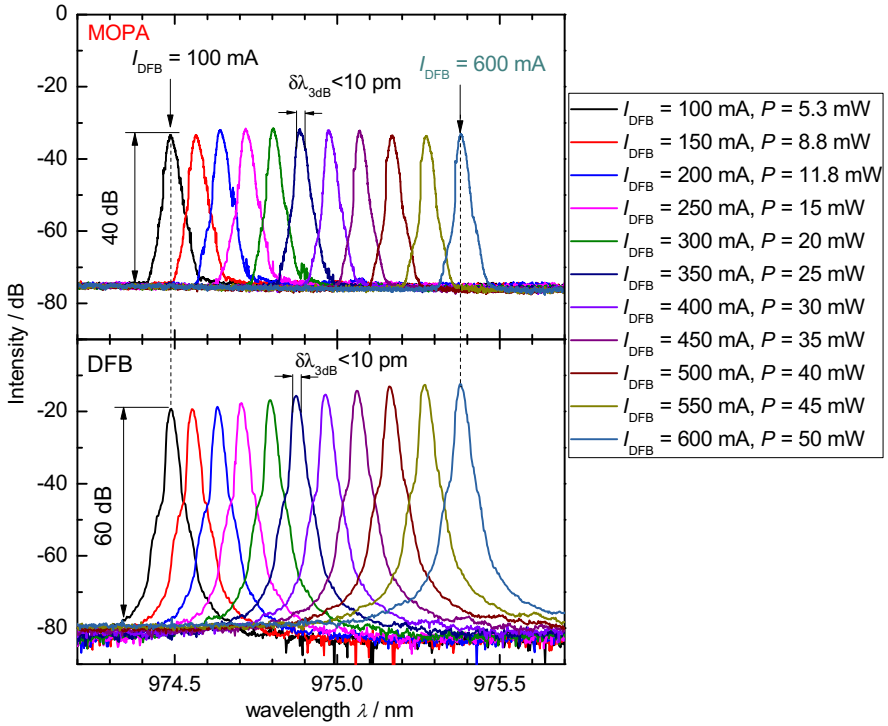

Figure 6.10: The upper graph: Emission spectra of the hybrid $MOPA$ for varying the MO input power with a constant of the optical output power of 16.5 W(I_{DFB}= 100 mA÷600 mA, in steps of 50 mA, responding to the input power from 5.3 mW to 50 mW, respectively) (at τ_{Delay} = 3.5 ns , τ_{OG} = 8 ns, I_{OG}= 100 mA, τ_{TS} = 15 ns, I_{TS}= 18.4 A and f = 25 kHz).
The lower graph: The MO spectra for comparison, the I_{DFB}= 100 mA÷600 mA, in steps of 50 mA, with power from 5.3 mW to 50 mW, respectively.

analyzer coincide for the $RW-DFB$ laser and the $MOPA$. The $RW-DFB$ laser has a side mode suppression ratio ($SMSR$) of 60 dB whereas the $SMSR$ of the $MOPA$ is deteriorated to 40 dB indicating the ASE contribution in the whole $RW-DFB$ injected current range.

The dependence of the optical spectra of the hybrid $MOPA$ on the current I_{DFB} as a color-scale mapping is shown in Fig. 6.11 for the fixed τ_{Delay} = 3.5 ns , τ_{OG} = 8 ns, I_{OG}= 100 mA, τ_{TS} = 15 ns, I_{TS}= 18.4 A and f = 25 kHz. Single mode operation without mode hopping is observed. The emission wavelength tunes over 0.9 nm with the spectral width remaining <10 pm when varying the injected current of the DFB

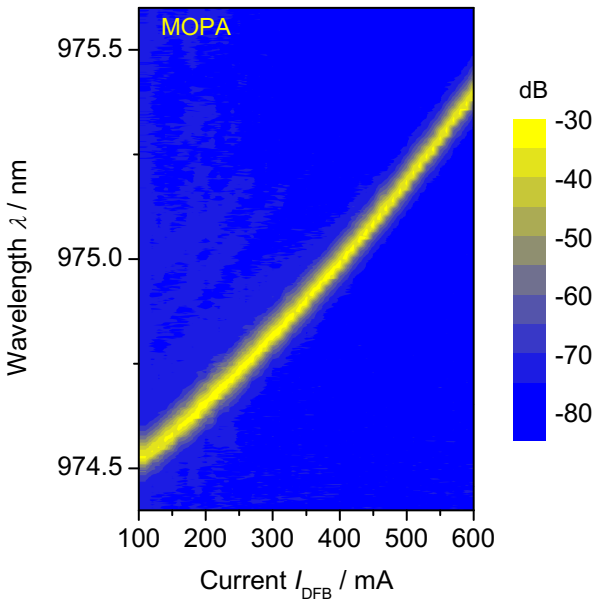

Figure 6.11: Color-scale mapping of the optical spectra of the $MOPA$ in dependence of the amplitude of the current injected into the $RW - DFB$ laser for a fixed τ_{Delay} = 3.5 ns , τ_{OG} = 8 ns, I_{OG}= 100 mA, τ_{TS} = 15 ns, I_{TS}= 18.4 A and f = 25 kHz.

laser from 100 mA to 600 mA.

The dependence of the optical peak power on the wavelength is given in Fig. 6.12. In the wavelength range from 974.50 nm to 974.66 nm the peak power rises with increasing wavelength due to the low input power. In the wavelength range from 974.66 nm to 975.40 nm, the output power remains constant with the maximum peak power of P_P = 16.3 W.

In this tuning range, a calculated water vapor spectrum in this region is also plotted (blue color). Here a path length of 1000 m and a relative humidity of 25% at 25 °C are applied by the $HITRAN$ database [45]. It can be seen that there are two strong absorption lines and five weaker lines of the water vapor. Using these tuning properties of the DFB laser it would be possible to scan over some absorption of the water vapor. It can be used to adjust the $DIAL$ measurement according to the current concentration of H_2O in the atmosphere. The strong lines are preferable for low concentrations, the weaker one for higher concentrations. It

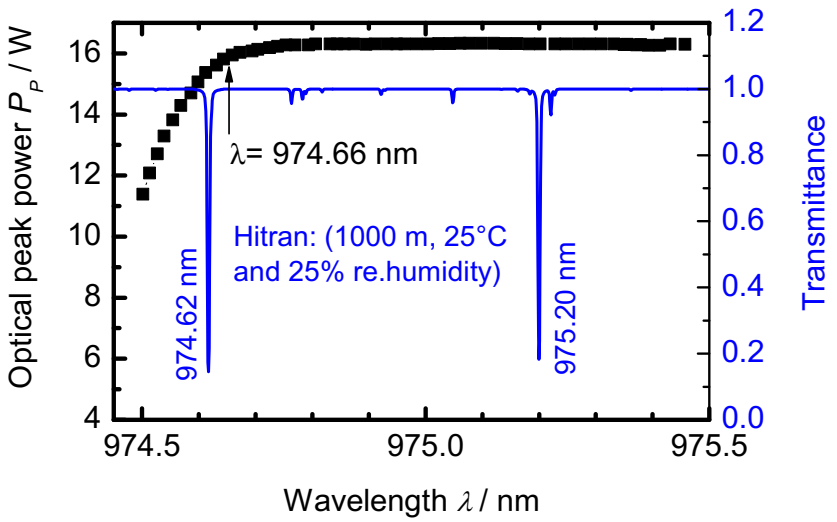

Figure 6.12: Optical peak power of the $MOPA$ in dependence on the input wavelength where the current injected into the $RW-DFB$ laser is varied (black squares). And a calculated spectrum based on the $HITRAN$ data compilation [45] for a path length of 1000 m and a partial pressure of 0.0069 atm (25% rel. humidity at 25 °C(blue line).

should be noted that a change of the operating temperature of the $RW-DFB$ laser would allow larger spectra coverage up to about 5 nm to 10 nm.

It should be mentioned that a fine tuning is possible to select a specific wavelength at an located absorption line of water vapor. A selected temperature of the DFB of $T = 35\,°C$ and a current of I_{DFB}= 270 mA are set for emission at wavelength 974.62 nm. The input power is set to 20 mW to reach an output power of 16.3 W. The emission wavelength is coincident with one of the strong absorption lines of water vapor (see in the Fig. 6.12). The spectra are measured in dependence of pulse currents of the TS section when keeping the $\tau_{Delay} = 3.5\,ns$, $\tau_{OG} = 8\,ns$, I_{OG}= 100 mA, $\tau_{TS} = 15\,ns$ and $f = 25\,kHz$. The color-scale spectral mapping in dependence on the current of the TS is shown in Fig. 6.13. It can be seen that over the whole current range of the TS the peak wavelength of the $MOPA$ does not vary and the spectral width remained below 10 pm, limited by resolution of OSA.

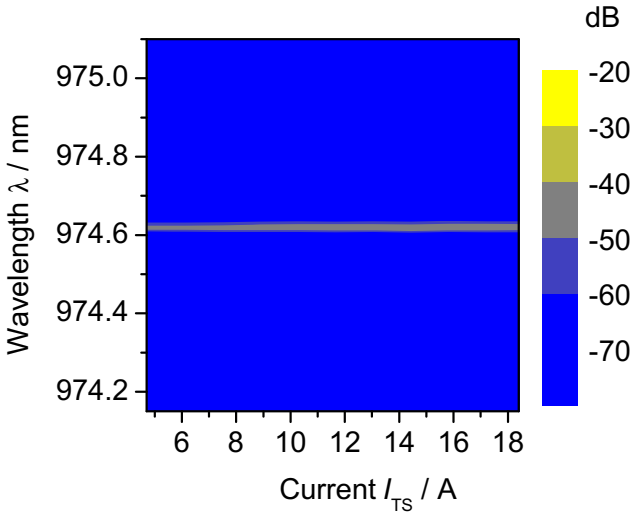

Figure 6.13: Color-scale mapping of the optical spectra of the $MOPA$ in dependence of the amplitude of the current pulses injected into the TS for a fixed DFB laser current, temperature and input power of 20 mW, $\tau_{Delay} = 3.5$ ns, $\tau_{OG} = 8$ ns, I_{OG}= 100 mA, $\tau_{TS} = 15$ ns and $f = 25$ kHz.

6.5 Conclusion

Nanosecond optical pulses at a wavelength of about 975 nm of hybrid $MOPA$ system was investigated. An optical peak power of 16.3 W with a pulse width of 8 ns is obtained. The ASE power amounts to less than 1% in comparison to the laser power. The emission wavelength could be tuned over 0.9 nm from 974.50 nm to 975.40 nm when varying the current of the $RW - DFB$ laser. The spectral width is smaller than 10 pm and the $SMSR$ is 40 dB.

In this tuning range, there are two strong and several weak absorption lines of the water vapor. It would be possible to adjust the $DIAL$ measurement according to the current concentration of H_2O in the atmosphere. The strong lines are preferable for low concentrations, the weaker one for higher concentrations. A change of the operating temperature of the heat sink would allow larger spectra coverage. A specific wavelength was selected as working point for an online resonance of an absorption line of the water vapor. In this case, the spectral properties

were measured in the whole range of the current into the TS section. The emission wavelength and the spectral line width of below 10 pm remained constant at all output power levels of the $MOPA$ system. The $SMSR$ amounts to 40 dB.

These parameters meet the demands of a light source for the measurement of absorption lines of molecular species such as H_2O under atmospheric conditions. For switching between on/off absorption line, two wavelengths are needed. Thus, in the next chapter a dual wavelength suitable for on/off absorption line will be given.

7 Dual wavelength diode laser based MOPA systems

In the previous chapters, the light sources offering a stabilized wavelength and a tunable wavelength were investigated. In this chapter, it is focused on a light source providing two wavelengths, one of which locates at the center of an absorption line for the online wavelength and the other is outside the absorption line for the offline wavelength. They are needed for $DIAL$ application.

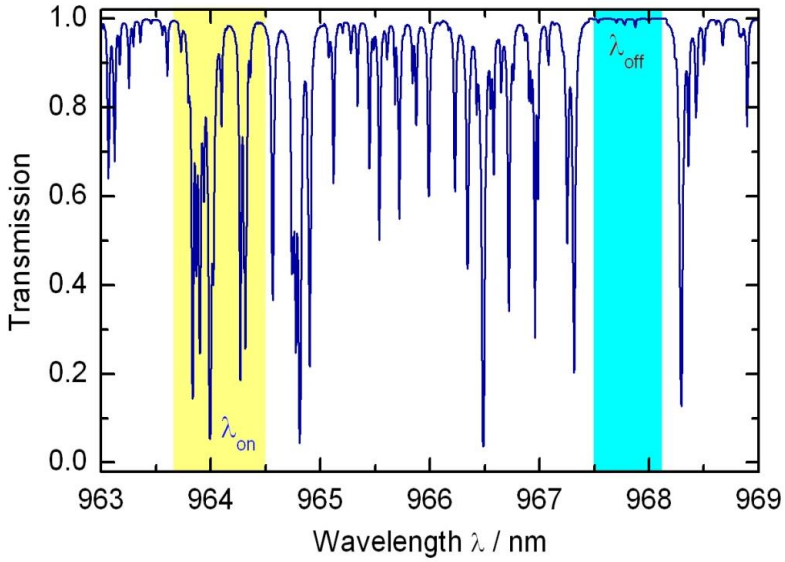

Figure 7.1: Calculated transmission spectrum for water vapor in air based on the line data from the $HITRAN$ data base, where a path length L=1000 m, a partial pressure P_{H_2O}=0.0069 atm, total pressure P_{total}= 1 atm at T= 296 K, (relative humidity of 25%) are used.

In order to select a pair wavelength for an on/off line of the water vapor absorption line, the $HITRAN$ database [45] can be used. It is compiled based on the line positions, line strength, line broadening, line shift coefficients and others. An absorption spectrum of H_2O near infrared between 963 nm and 969 nm is given in Fig. 7.1. Here a path length L=1000 m, a partial pressure P_{H_2O}=0.0069 atm, total pressure P_{total}= 1 atm at T= 296 K, (relative humidity of 25%) are used.

It is obvious that in the spectral range between 967.4 nm to 968.20 nm only weak absorption lines occur. This region is therefore preferable as region for the off line wavelength λ_{off}. The on line wavelength λ_{on} as mentioned in the section 2.2 should be selected based on the line parameters relevant for the DIAL application, e.g., the temperature dependence of the absorption and the pressure dependence of the line position. Due to the available master oscillator, in this part the potential window for λ_{on} was selected between 963.60 nm and 964.50 nm.

A combination of a short pulse width, a high peak power, a narrow spectral line width and dual wavelength in this range will be presented. A short description of $Y-branch-DFB$ laser, power voltage current characteristics for two branches and the spectral properties of the alternative two wavelengths will be presented. Then the spectral properties and peak power of hybrid $Y-branch-DFB-MOPA$ system will be discussed. Finally a conclusion will be given.

7.1 Dual wavelength Y-branch-DFB laser as master oscillator

First of all, the power-voltage-current characteristics at different temperatures of the heat sink of the $Y-branch-DFB$ laser, see in Fig.3.6 are measured. The injection current at the common section is set to I_F = 10 mA whereas the current at the $Y-branch-DFB$ section is set to I_Y = 0 mA to avoid cross talk between both resonators. The optical power and the voltage versus the injection current I_{G1} (DFB_1) and I_{G2} (DFB_2) at temperatures between T = 20 °C and 35 °C are shown in Fig. 7.2 a, respectively. It can be seen that laser operation starts at 67 mA and 72 mA, and reach powers between of P = 96 mW and 90 mW at 250 mA, respectively. In the second branch, the laser operation starts at 67 mA and 81 mA, and reach powers between of P = 90 mW and 86 mW, respectively at 250 mA in CW operation. A slope efficiency of two branches of about 0.55 W/A is reached. In the hybrid $MOPA$ system, the input power of the seed laser needs about 20 mW. It can be easily reached with this device.

The spectrum analyzer (*Advantest Q*8384) with a resolution of 10 pm and a dynamic range of 60 dB is used to measure the optical spectra.

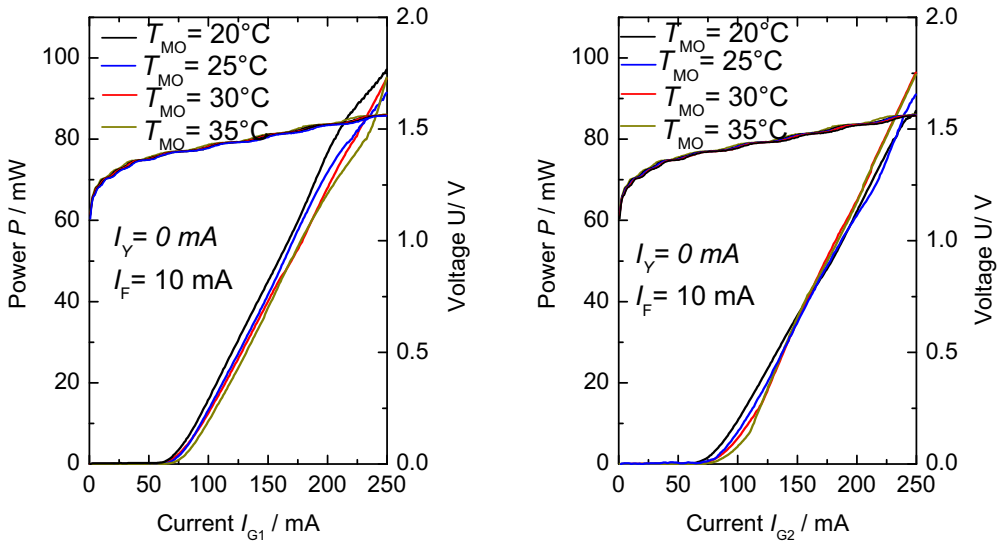

(a) (b)

Figure 7.2: Power voltage current characterization of two branches (I_{G1} - a) and (I_{G2} - b) when fixed current of $I_F = 10\,\mathrm{mA}$, $I_{Y1} = I_{Y2} = 0\,\mathrm{mA}$ at different temperatures between $T = 25\,^{\circ}\mathrm{C}$ and $35\,^{\circ}\mathrm{C}$.

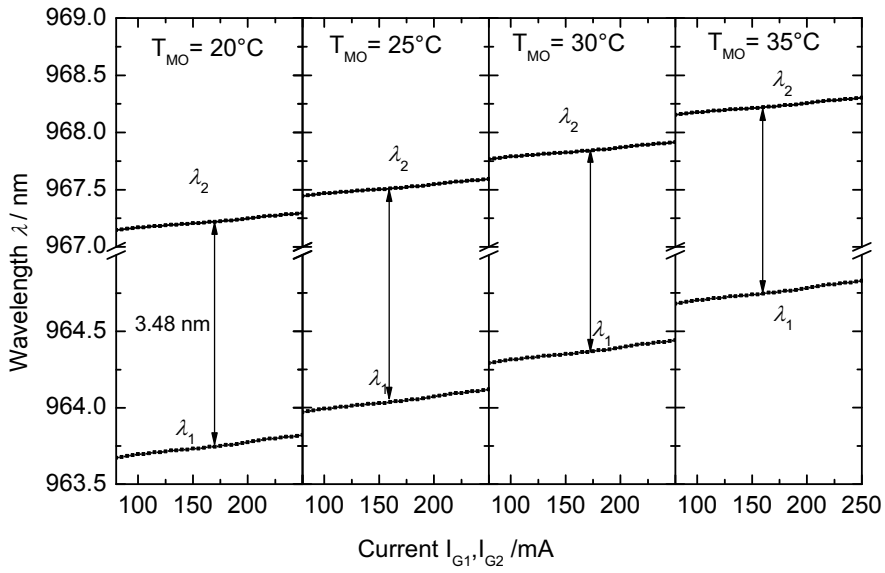

Figure 7.3: Shifting wavelength by current into two branches at different temperatures (T= 20 °C, 25 °C, 30 °C, 35 °C) with fixed current of $I_F = 10\,\mathrm{mA}$, $I_{Y1} = I_{Y2}$= 0 mA.

The peak wavelength tuning rates by temperature and injected current are $70\,^{pm}/_{K}$ and $0.89\,^{pm}/_{mA}$, respectively. Fig. 7.3 shows the measured tuning peak wavelength by varying injected current into two branches of $Y-branch-DFB$ laser at different temperatures (T= 20 °C, 25 °C, 30 °C and 35 °C) with fixed current of I_F = 10 mA, $I_{Y1} = I_{Y2}$ = 0 mA. A stable distance between two wavelengths of 3.48 nm is observed.

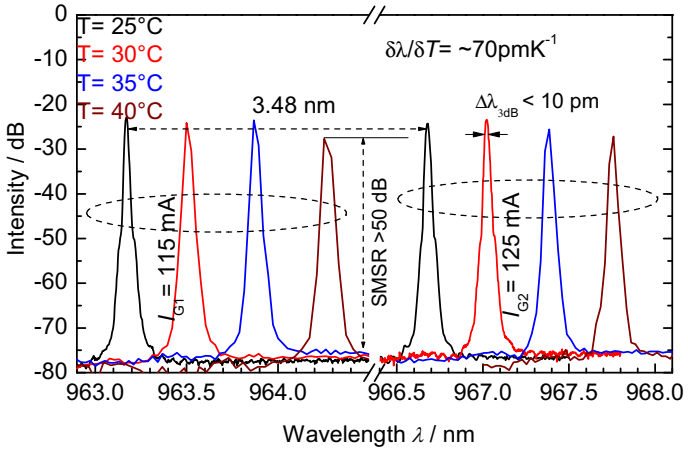

Figure 7.4: Dependence of the peak wavelength on the heat sink temperature for the two branches of the Y-branch-DFB laser fixed currents I_F = 10 mA, $I_{Y1} = I_{Y2}$ = 0 mA, I_{G1} = 105 mA and I_{G2} = 115 mA at heat sink temperatures of T = 25 °C, 30 °C, 35 °C, 40 °C with the fixed power of 20 mW.

In comparison with the water vapor absorption spectrum in Fig. 7.1, it is visible that in the tuning range of branch one (λ_1: from 963.67 nm to 964.83 nm), the yellow range in Fig. 7.1, there are some absorption lines. In contrast, within the tuning range of branch (λ_2: from 967.40 nm to 968.30 nm), the blue range in Fig. 7.1, only weak absorption lines occur. This is a good solution as a master oscillator for water vapor profile measurement in $DIAL$ application.

The optical spectra measured at I_F = 10 mA, $I_{Y1} = I_{Y2}$ = 0 mA, I_{G1} = 105 mA and I_{G2} = 115 mA corresponding to a power of about 20 mW at the different heat sink temperatures are given in Fig. 7.4. A side mode suppression ratio of more than 50 dB with a spectral line width of 10 pm, limited by spectrum analyzer, is observed for all spectra.

7.2 Amplified spontaneous emission under ns-pulse excitation

The wide gain profile of the tapered amplifier with integrated optical gate used in the previous chapter covers well this wavelength range (see Fig. 6.5 b). Therefore, it is also used in this chapter. The modulated conditions of the OG and TS are identical with the previous chapter. The ASE power at T= 30 °C, a current pulse with a length of τ_{TS} = 15 ns, a repetition rate of f = 25 kHz and an amplitude of I_{TS} = 18.4 A is injected into the TS, the ASE of 1.4 mW, average power or 3.8 W peak power was reached. The peak wavelength of the ASE spectra of about λ = 969 nm and the 3 dB full width of the spectrum of 18 nm were obtained. More details can be read in section 6.2

7.3 Optical power and spectral properties of MOPA system with dual wavelength

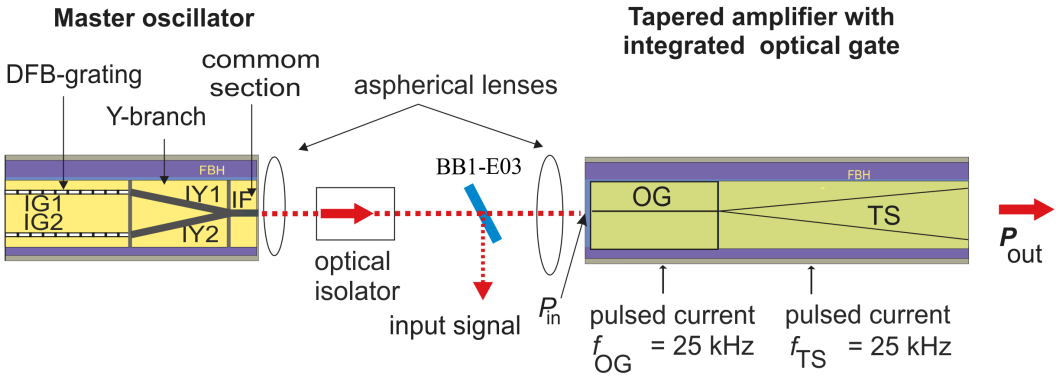

Figure 7.5: Schematic diagram of hybrid $Y-branch-DFB-MOPA$ system.

A scheme of hybrid $Y-branch-DFB-MOPA$ system is given in Fig. 7.5. The operation conditions of the MO and PA are identical to the previous chapter. As the DFB laser used in previous chapter, the $Y-branch-DFB$ laser operates at CW current. The RW section of the tapered amplifier serves as an optical gate (OG) and the tapered section works as gain section, both operate at pulsed currents. A current pulse amplitude of I_{OG} = 100 mA and the pulse width of 8 ns are

injected into OG section. The pulsed width of the TS is 15 ns. A delay time between the pulses of the TS and the OG of 3.5 ns is used. The repetition rate f of the current pulses injected into both sections (OG and TS) is 25 kHz.

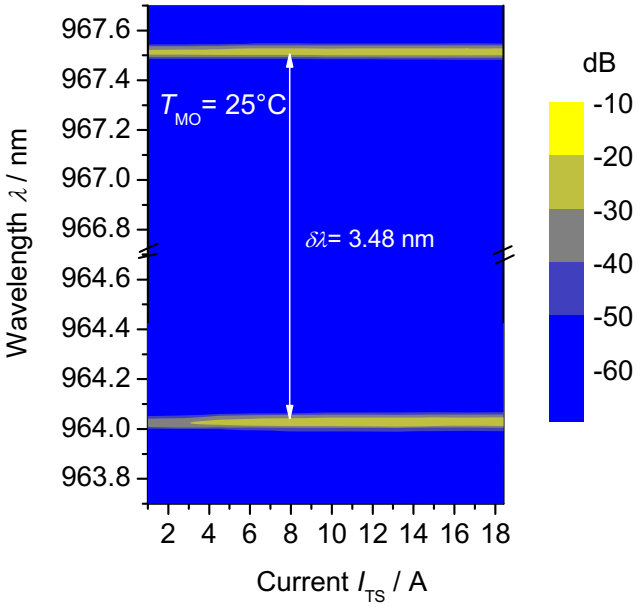

Figure 7.6: Color-scale mapping of the optical spectra of the $MOPA$ in dependence of the amplitude of the current pulses injected into the TS for a fixed input power (20 mW) for each branch at τ_{Delay} = 3.5 ns, τ_{Pulse} = 8 ns, I_{OG}= 100 mA, τ_{TS} = 15 ns, f = 25 kHz at T_{Y-DFB} = 25 °C.

The MO is the $Y-branch-DFB$ laser, which operates in CW mode. The input power is set at 20 mW for each branch and the desired pair wavelength are set by adjustment of the currents and temperatures. The dependence of optical spectra on the pulsed current into the TS then are measured.

In Fig. 7.6, a color-scale mapping of the optical spectra of the $MOPA$ in dependence of the amplitude of the current pulses injected into the TS is given. Here, the input power (20 mW) for each branch of $Y-branch-DFB$ laser and τ_{Delay} = 3.5 ns, τ_{Pulse} = 8 ns, I_{OG} = 100 mA, τ_{TS} = 15 ns, f = 25 kHz at T = 25 °C are fixed. The MO is operated at I = 130 mA for each branch and T= 25 °C. Therefore the seeding peak wavelength is fixed. Over the whole range of TS currents the peak

wavelength of the $MOPA$ did not vary.

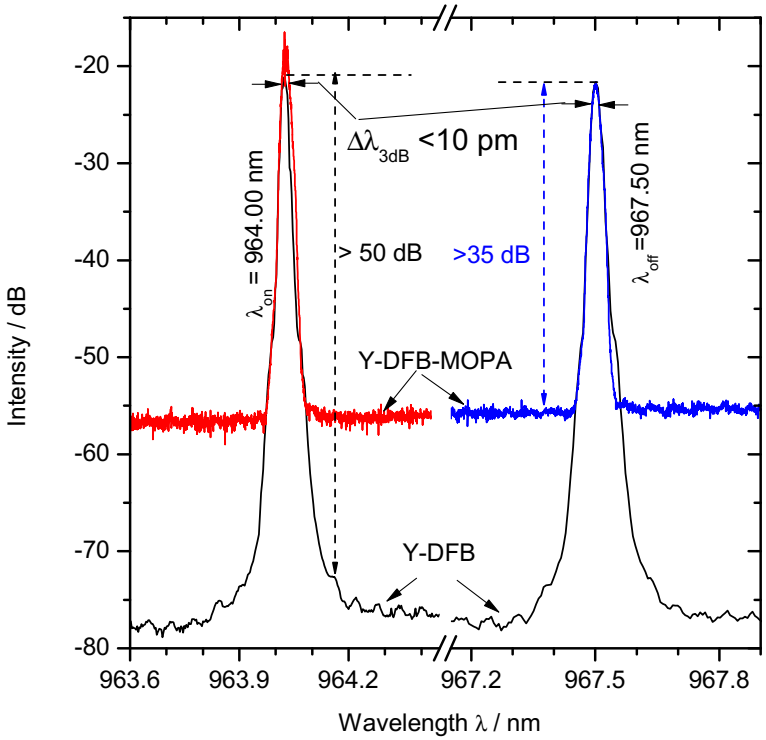

Figure 7.7: Optical spectra of the $Y-Branch-DFB$ or each branch are fixed the input power (20 mW) and optical spectra of the $Y-Branch-DFB-MOPA$ at P_{in} = 20 mW, τ_{Delay} = 3.5 ns, τ_{Pulse} = 8 ns, I_{OG}= 100 mA, τ_{TS} = 15 ns, f = 25 kHz at T_{Y-DFB} = 25 °C.

Optical spectra of input (P_{in}= 20 mW for each branch) and the output of the $MOPA$ system at peak power of 16.3 W for each branch (P_{in}= 20 mW, τ_{Delay} = 3.5 ns, τ_{Pulse} = 8 ns, I_{OG} = 100 mA, τ_{TS} = 15 ns, f = 25 kHz at T = 25 °C) are measured at the same range and resolution of the OSA. A comparison between the optical input and output of the hybrid $MOPA$ system is shown in Fig. 7.7. Two peak wavelengths 964.00 nm and 967.50 nm with a $SMSR$ of about 50 dB and larger than 35 dB for input and output of the $MOPA$, respectively, are observed. The measured spectral full width at 3 dB of 10 pm for both cases are given by the resolution limit of the optical spectrum analyzer. The wavelength 964.00 nm is located at center of an absorption line and the other 967.50 nm is located at non-absorption line, respectively.

The system can work at other dual wavelengths by changing either the heat sink temperatures or currents. At the temperature of heat sink of MO of 30 °C, two wavelengths of two branches are shifted to 964.33 nm and 967.81 nm with remained the spectral width and $SMSR$. In which, a wavelength (964.33 nm) is located at the center of an another absorption line, and another 967.33 nm is outside of absorption line, respectively.

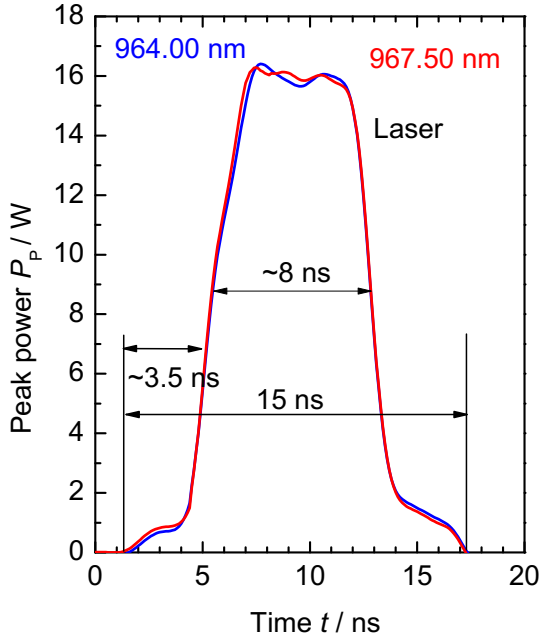

Figure 7.8: Temporal pulse shapes of optical peak power at two wavelengths (964.02 nm and 967.50 nm) at P_{in}= 20 mW and τ_{Delay} = 3.5 ns, τ_{Pulse} = 8 ns, I_{OG}= 100 mA, τ_{TS} = 15 ns, I_{TS}= 18.4 A, f = 25 kHz and $T_{Y-branch-DFB}$ = 25 °C.

The optical peak powers at two wavelengths are measured. As the previous chapter the tapered amplifier operates in saturation when the input power in the range of 15 mW and 50 mW, an approximate output optical power of 16.3 W was reached. In this experiment the input power of 20 mW is set for all wavelengths. Thus a peak power of 16.3 W is obtained. Fig. 7.8 illustrates the peak power behind the PA of two wavelengths (964.00 nm, and 967.50 nm), respectively for a pair of on/off line as remarked on the transmission of water vapor at default of T= 296 K, P= 1 atm, L= 1000 m and 25% relative humidity from $Hitran$

database in Fig. 7.1.

It can be summarized that the hybrid $MOPA$ system based $Y-branch-DFB$ laser and tapered amplifier enables not only to emit dual wavelength but also to tune wavelengths by currents and temperatures, which allows to select a desired pair wavelength for on/off line wherein the absorption coefficients are different. It is useful in $DIAL$ application when atmosphere condition changes rapidly. These properties meet the demands as laser transmitter in $DIAL$ system for detection of water vapor absorption lines.

7.4 Conclusion

Nanosecond optical pulses emitting at two distinct wavelengths at about 964 nm and 968 nm are generated. The hybrid $MOPA$ system consists of a $Y-branch-DFB$ laser and a two-section tapered amplifier. The $Y-branch-DFB$ laser operates in CW mode. The optical gate generates the optical pulse which is then subsequently amplified by the tapered section. An optical peak power of 16.3 W with a pulse width of 8 ns at a repetition rate of 25 kHz was obtained. The spectral line widths of below 10 pm, limited by spectrum analyzer, remained constant at all output power levels of the $MOPA$ system. A $SMSR$ of more than 35 dB was observed. These properties are suitable for the measurement of absorption lines of water vapor under atmospheric conditions in $DIAL$ application.

The system can emit alternatively at two wavelengths. They can be tuned by current and temperature, leading an opportunity to select a pair wavelength for on/off line of the water vapor absorption line for $DIAL$ applications. The different strengths of line are suitable for different atmospheric conditions. It is useful in the case of a rapidly changing atmosphere. In the future, this system should be applied in experiments for differential absorption water vapor measurement.

8 Conclusion and outlook

8.1 Conclusion

The scope of this work was the realization and the analysis of the potential of all-diode laser light sources for $MPLs$ application. The challenges are combining a narrow spectral line width with a high optical peak power in the ns-pulse regime, containing a small amount of AES. The specifications of the light source were derived based on the need coming from the application, i.e., aerosol and gas measurements. To meet the demand, the light sources are performed in the ns-pulse regime at a repetition rate of 25 kHz, leading to a resolution in the m range in an altitude of 6 km. As mentioned in the motivation, for the gas absorption line measurement, a spectral line width of 10 pm is required, whereas for aerosols a spectral line width of 300 pm is sufficient. A high optical power provides a higher amount of backscattered photons reaching the receiver, so that a large signal-to-noise ratio can be achieved. In the literature of $MPLs$ optical peak powers of 10 W were achieved with a typical amount of ASE of larger than 17.6%. Peak powers of more than 16.3 W and an amount of ASE smaller than 1% in the hybrid $MOPA$ is reached in this work, which guarantees a high spectral purity and therefore a high accuracy in the measurements.

Two $MOPA$ concepts were investigated, namely monolithic and hybrid systems.

The monolithic $MOPA$, where MO and PA are integrated on one single chip, operates at a wavelength of 1064 nm. This system is compact. No optical components and adjustment of system are needed. Disadvantageous is that the interaction of MO and PA can not be controlled due to its integration on a single chip. The uncontrollable optical feedback and thermal coupling cause broader spectral line widths and unstable spectra. A spectral line width of about 150 pm with a $SMSR$ of 30 dB was observed. A ratio between the ASE and the laser of 9% was estimated. These spectral properties fulfill the requirements for aerosol detection. However, the spectral line width is not sufficient for absorption line of the gasses, e.g., water vapor.

In contrast to monolithic $MOPA$, the hybrid $MOPA$ systems have separated chips for MO and PA. It allows adjusting and controlling or even changing the MO and PA individually for the desired purposes. Three different hybrid $MOPA$ systems were investigated, offering a stabilized wavelength at 1064 nm, a continuously tunable wavelength around 975 nm and a dual wavelength around 964 nm. Common for all hybrid $MOPA$ systems, a spectral line width below 10 pm, for both MO and $MOPA$, respectively, limited by the resolution of the spectrum analyzer. A $SMSR$ better than 50 dB for the MO and of larger than 35 dB for the whole $MOPA$ was reached. These spectral properties are well suited for measurements of molecular species in the atmosphere, e.g., water vapor.

The stabilized light source at a specific wavelength was realized to enable a MPL for the detection of a well defined absorption line. The second system, featuring 0.9 nm continuous tunable wavelength, showed sufficient properties to scan over two strong and several weak absorption lines of the water vapor. This configuration can be applied to the concentration calibration of water vapor. The dual wavelength system proofed the capability of tuning the two emitted wavelengths into the center and the outside region of an absorption line, respectively. This can be used for switching between on/off line in $DIAL$ applications.

The calculation method for the amount of ASE was studied and led to a model which is in good agreement to a former model developed by Ulm. An amount of ASE of the hybrid $MOPA$ systems below 1% is obtained due to optimized delay time between the OG and TS. In order to make sure that the carrier density in the excited state and therefore optical gain reaches its maximum before the optical pulse is transmitted by the OG, the delay time has to be in the range of the order of 1 ns.

Since the tunable wavelength hybrid $MOPA$ was realized by changing the injection current of the DFB laser which again leads to a variation in the input power, the dependence of output power on input power was investigated. It was shown that the output power remained constant in a large range of input powers from 15 mW to 50 mW. This allows constant power operation also when varying the injected current or the temperature to change the wavelengths. The hybrid $MOPA$ works stable over

a wide spectral range.

In summary, the diode laser based $MOPA$ systems in this work were proven to provide all spectral properties required for detection of atmospheric gases such as aerosol and water vapor. Pulse widths in the ns-range with a peak power of 16.3 W, corresponding to an energy in the nJ-range, were achieved, which enabled a drastic increase in spatial resolution. Moreover, no saturation in optical peak power was seen. It is possible to achieve higher output power by using higher pulsed injection currents.

8.2 Outlook

The monolithic $MOPA$ and the three different hybrid $MOPA$ systems presented here meet the spectral requirements for aerosols and water vapor detection. They are ready for water vapor absorption spectroscopy measurements under different pressure or concentration to determine the detector limits and the spectral resolution of the systems.

To obtain higher optical peak power, experiment with higher current supply sources should be performed to determine the limitation of the tapered amplifier.

For further application in a real $DIAL$ system, it is very important to have information about the beam quality under the pulse excitation. It helps to calculate the size of the field of view of the telescope, which mainly serves for the suppression of both background light and scattered laser light from the short range.

Miniaturization of the system to a compact module should be performed, which integrates the electrical circuit and all components on the micro bench.

Last but not least, a transfer to other wavelengths should be performed to address other species of trace gases or aerosols.

List of Abbreviations and Symbols

The following abbreviations and symbols are widely used within this work.

Abbreviations

Al	Aluminum
As	Arsenide
ASE	Amplified spontaneous emission
CW	Continuous wave
Cr	Chromium
DM	Direct modulation
DQW	Double quantum well
DBR	Distributed Bragg reflector
DFB	Distributed feedback
DIAL	Differential absorption LIDAR
ECDL	External cavity diode laser
ECL	Emitter-couple-logic
HITRAN	High-resolution transmission
FWHM	Full width at half maximum
Ga	Gallium
LIDAR	light detection and ranging
In	Indium
MPL	Micro pulse LIDAR system
MPLs	Micro pulse LIDAR systems
MPE	maximum permissible exposure
NASA	National aeronautic and space administration
MO	Master oscillator
MOPA	Master oscillator power amplifier

Nd	Neodym
OG	Optiacal gate
P	Phosphorus
PA	Power amplifier
PG	Pulse generation
PUI	The power voltage current
TS	Tapered section
TPA	Tapered power amplifier
RW	Ridge wave-guide
S	The slope efficenncy
SQW	Single quantum well
Si	Silicon
SMSR	Side mode suppression ratio
SOA	Semiconductor optical amplifier
YAG	Yttrium aluminium garnet
c	Vacuum speed of light
f	Frequency
T	Period of time
T	Temperature
τ	Pulse width
E_p	Pulse energy
f(t)	Temporal shape of the optical output pulse
P(t)	Temporal optical peak power
τ_{TS}	Width of the pulse current through tapered section
τ_{OG}	Width of the pulse current through optical gate
τ_{delay}	Timing delay between the optical gate and tapered section
P_p	Peak optical power
R_f	Reflectivity of front facet
R_r	Reflectivity of rear facet

Symbols

$\Delta\lambda$	Spectral linewidth
λ	Wavelength
$T(R)$	Transmission tern at distance R
$\Delta\alpha_{mol,abs}$	The differential molecular absorption cross section
$\Delta\sigma_{mol,abs}$	The differential absorption cross section
$\beta(R)$	Back-scatter coefficient at distance R
β_{mol}	Molecular scatter coefficient
β_{aer}	Aerosols scatter coefficient
α_{aer}	The extinction coefficient
σ_{ext}	The extinction cross section
σ_{sca}	The extinction cross section by scattering
$\sigma_{abs}(\lambda)$	The extinction cross section by absorption
$\sigma_{j,sca}$	The scattering cross section of the scatter j
$\alpha_{mol,sca}$	The scattering extinction coefficient by molecular
$\alpha_{aer,sca}$	The scattering extinction coefficient by aerosols
$\alpha_{mol,abs}$	The absorption extinction coefficient by molecular
$\alpha_{aer,abs}$	The scattering extinction coefficient by aerosols
$T(R)$	Transmission tern at distance R
$\Delta\alpha_{mol,abs}$	The differential molecular absorption cross section
$\Delta\sigma_{mol,abs}$	The differential absorption cross section
α_{WV}	Water vapor extinction coefficient
σ_{WV}	Water vapor absorption cross section
$\sigma_{eff}(r)$	The effective absorption coefficient
N_{WV}	Number density or number concentration of water vapor
P_{on}	The back scattering intensity at wavalenth λ_{on}
P_{off}	The back scattering intensity at wavalenth λ_{off}

List of Publications

Part of this work has been previously published in following scientific publications:

Articles

- Thi Nghiem Vu, Andreas Klehr, Bernd Sumpf, Hans Wenzel, Götz Erbert, Günther Tränkle : Wavelength stabilized ns-MOPA diode laser system with 16 W peak power and a spectral line width below 10 pm, Semicond. Sci. Technol. 29 (2014) 035012 (7pp).
- Thi Nghiem Vu, Andreas Klehr, Bernd Sumpf, Hans Wenzel, Götz Erbert, Günther Tränkle: Tunable 975 nm nanosecond diode laser based master-oscillator power-amplifier system with 16.3 W peak power and a narrow spectral line width below 10 pm, Optics Letters, Vol. 39, No.17/September 1, 2014, pp. 5138-5141.
- Thi Nghiem Vu, Andreas Klehr, Bernd Sumpf, Hans Wenzel, Götz Erbert, Günther Tränkle: A dual wavelength Y-Branch-DFB laser power amplifier (MOPA) system suitable for water vapor differential absorption Lidar, in preparation for Journal of applied physics B.

Proceedings

- Andreas Klehr, Bernd Sumpf, Thi Nghiem Vu, Hans Wenzel, Götz Erbert, Günther Tränkle: 1064 nm wavelength stabilized hybrid ns-MOPA diode laser system for high peak power and low spectral width, Lasers and Electro-Optics Europe (CLEO EUROPE/IQEC), 2013 Conference on and International Quantum Electronics Conference.
- Thi Nghiem Vu, Andreas Klehr, Bernd Sumpf, Hans Wenzel, Götz Erbert, Günther Tränkle : 973 nm wavelength stabilized hybrid ns-MOPA diode laser system with 15.5 W peak power and a spectral line width below 10 pm, Proc. SPIE 9134, Semiconductor Lasers

and Laser Dynamics VI, 91340T (May 2, 2014).

- Bernd Sumpf, Andreas Klehr, Thi Nghiem Vu, Götz Erbert, Günther Tränkle: 975 nm high-peak power diode laser based MOPA suitable for DIAL applications, Proc. SPIE 9382, Novel In-Plane Semiconductor Lasers XIV, 93821K (March 10, 2015).

- Thi Nghiem Vu, Andreas Klehr, Bernd Sumpf, Thomas Hoffmann, Armin Liero, Günther Tränkle: Pulsed hybrid dual wavelength Y-branch-DFB laser tapered amplifier system suitable for water vapor detection at 965 nm with 16 W peak power, Proc. SPIE 9767, Novel In-Plane Semiconductor Lasers XV, 97670R (March 7, 2016); doi:10.1117/12.2208129.

Conference Talks

- Andreas Klehr, Bernd Sumpf, Thi Nghiem Vu, Hans Wenzel, Götz Erbert, Günther Tränkle: 1064 nm wavelength stabilized hybrid ns-MOPA diode laser system for high peak power and low spectral width, CLEO Europe/ IQEC, session Lasers and Electro-Optics Europe, Munich, Germany, May 12-16, Poster CL-P.30, 2013.

- Thi Nghiem Vu, Andreas Klehr, Bernd Sumpf, Thomas Hoffmann, Hans Wenzel, Götz Erbert, Günther Tränkle: Narrow spectral linewidth diode laser light sources with 3 ns optical pulses and up to 16 W peak power suitable for micro-LIDAR sensors for gases and aerosols, LOB, section 5.3, Berlin 18-20, March 2014.

- Thi Nghiem Vu, Andreas Klehr, Bernd Sumpf, Hans Wenzel, Götz Erbert, Günther Tränkle : 973 nm wavelength stabilized hybrid ns-MOPA diode laser system with 15.5 W peak power and a spectral line width below 10 pm, SPIE Photonics Europe, session 6, High-Performance Laser Diode, Brussels, April 15^{th} 2014, Paper 9134-28.

- Bernd Sumpf, Andreas Klehr, Thi Nghiem Vu, Götz Erbert, Günther Tränkle: 975 nm high-peak power diode laser based MOPA suitable for DIAL applications, SPIE Photonics West, Session 9, High brightness, San Francisco, 9-12^{th} Feb. 2016, Paper 9382-54.

- Thi Nghiem Vu, Andreas Klehr, Bernd Sumpf, Thomas Hoffmann, Armin Liero, Günther Tränkle: Pulsed hybrid dual wavelength Y-branch-DFB laser tapered amplifier system suitable for water vapor detection at 965 nm with 16 W peak power, SPIE Photonics West, Session 6, DFB and DBRs, San Francisco, 13-18th Feb. 2016, Paper 9767-26.

Bibliography

[1] R.J. Charlson, S. Schwartz, J. Hales, R.D. Cess, J.R.Jr. Coakley, J. Hansen, and D. Hofmann Science. "Climate forcing by anthropogenic aerosols". In: *Science* **255**.5043 (1992), pp. 423–430.

[2] K.N. Liou. "Influence of cirrus clouds on weather and climate processes. A global perspective." In: *Mon. Weather Rev.* **9348** (1986), pp. 1–10.

[3] "http://www.esrl.noaa.gov/research/themes/aerosols/". In: (2015).

[4] K. E. Trenberth, P. D. Jones, P. Ambenje, R. Bojariu, D. Easterling, A. Klein Tank, D. Parker, F. Rahimzadeh, J.A. Renwick, M. Rusticucci, B. Soden, and P. Zhai. "Observations: Surface and Atmospheric Climate Change". In: *Cambridge University Press, Cambridge, United Kingdom and New York, NY, USA.* **8241**.82410U (2007), pp. 1–10.

[5] T. Schneider, P.A. O'Gorman, and X.J. Levine. "Water vapor and the dynamics of climate changes". In: *Reviews of Geophysics* **48**.3 (2010). RG3001, pp. 8755–1209.

[6] H. Vogelmann and T.Trickl. "Wide-range sounding of free-tropospheric water vapor with a differential-absorption lidar (DIAL) at a high-altitude station". In: *Applied Optics* **47**.12 (2008), pp. 2116–2132.

[7] J. Harries. "Atmospheric radiation and atmospheric humidity". In: *Quarterly Journal of the Royal Meteorological Society* **123**.544 (1997), pp. 2173–2186.

[8] W. Kininmonth. "Clausius Clapeyron and the Regulation of Global Warming". In: *Australasian Climate Research, Melbourne, Australia* **26**.5-6 (2010), pp. 61–70.

[9] G.G. Goyer and R. Watson. "The Laser and its Application to Meteorology". In: *Bulletin of the American Meteorological Society.* **44**.9 (1963), 564Ű575.

[10] V. Wulfmeyer and G. Feingold. "On the relationship between relative humidity and particle backscattering coefficient in the marine boundary layer determined with differential absorption lidar". In: *JOURNAL OF GEOPHYSICAL RESEARCH* **105**.D4 (2000), pp. 4729–4741.

[11] P. Werlea, F. Slemra, K. Maurera, R. Kormannb, R. Mucke, and B. Janker. "Near- and mid-infrared laser-optical sensors for gas analysis". In: *Optics and Lasers in Engineering* **37** (2002), pp. 101–114.

[12] L. Fiorani. "Lidar: a powerful tool for atmospheric measurements". In: *Journal of Optoelectronics and Advanced Materials* **1**.3 (1999), pp. 1–11.

[13] A. S. Moore, K. E. Brown, W. M. Hall, J. C. Barnes, W. C. Edwards, L. B. Petway, A. D. Little, W. S. Luck, I. W. Jones, C. W. Antill, E. V. Browell, and S. Ismail. *Development of the Lidar Atmospheric Sensing Experiment (LASE) - An Advanced Airborne DIAL Instrument.* **Chapter 4**. 281-289. Springer Berlin Heidelberg, 1997.

[14] S. M. Pershin, A. N. Lyash, V. S. Makarov, K.Hamal, I. Prochazka, and B. Sopko. "Multilayers clouds monitoring by micro-Joule lidar based on photon counting receiver and diode laser". In: *Proc. SPIE 7355, 4 pages.* 2009.

[15] N. S. Higdon, E. V. Browell, P. Ponsardin, B. E. Grossmann, C. F. Butler, T. H. Chyba, M. N. Mayo, R. J. Allenand A. W. Heuser, W. B. Grant, S. Ismail, S. D. Mayor, and A. F. Carter. "Airborne differential absorption lidar system for measurements of atmospheric water vapor and aerosols". In: *Appl. Opt.* **33**.27 (1994), pp. 6422–6438.

[16] G. Ehret, A. Fix, V. Weiss, G. Poberaj, and T. Baumert. "Diode-laser-seeded optical parametric oscillator for airborne water vapor DIAL application in the upper troposphere and lower stratosphere". In: *Appl. Phys. B* **67**.4 (1998), pp. 427 –431.

[17] C. Kiemle, A. Schäfler, M. Wirth, A.Fix, and S. Rahm. "Detection and Analysis of Water Vapor Transport by Airborne Lidars". In: *in IEEE Jounal of selected topics in applied earth osbservations and remote sensing* **6** (2013), p. 3.

[18] C. R. Prasad, V. A. Fromzel, J. S. Smucz, I. H. Hwang, and W. E. Hasselbrack. "A Diode-Pumped Cr:LiSAF Laser for UAV Based Water Vapor Differential Absorption Lidar (DIAL)". In: *in IEEE Int. Geosci. Rem. Sens. Symposium,* (2000), pp. 1465 –1467.

[19] E. V. Browell, S. Ismail, and W. B. Grant. "Differential absorption lidar (DIAL) measurements from air and space". In: *Appl. Phys. B* **67**.4 (1998), pp. 399–410.

[20] S.Lehmann and J. Bösenberg. *A Water Vapor DIAL System Using Diode Pumped Nd:YAG Lasers.* **Advances in Atmospheric Remote Sensing with Lidar**. Springer Berlin Heidelberg, 1997.

[21] M. Hamilton, A. Dinovitesr, and R. A. Vincent. "Towards low cost water vapour differential absorption LIDAR". In: *Proc. 8th Int. Symp. Tropospheric Profiling, ISBN 978-98-6960-233-2, S13-002-1.* 2008.

[22] J. L. Machol. "Preliminary measurements with an automated compact differential absorption lidar for the profiling of water vapor". In: *J. Applied Optics* **43**.15 (2004), pp. 3110–3121.

[23] A. R. Nehrir, K. S. Repasky, J.L. Carsten, M.D.Obland, and J-A. Shaw. "Water Vapor Profiling Using a Widely Tunable, Amplified Diode-Laser-Based Differential Absorption Lidar (DIAL)". In: *J. Atmos. Oceanic Technol* **26** (2009), pp. 733–745.

[24] A. R. Nehrir and K. S. Repasky. "Eye-Safe Diode-Laser-Based Micropulse Differential Absorption LIDAR (DIAL) for Water Vapor Profiling in the Lower Troposphere". In: *J. Atmos. Oceanic Technol* **28**.2 (2011), pp. 131–147.

[25] M.D.Obland, K.S. Repasky, A.R.Nehrir, L.Carlsten, and J. A. Shaw. "Development of a widely tunable amplified diode laser differential absorption lidar for profiling atmospheric water vapor". In: *Jounal of Applied Remote Sensing* **4** (2010), p. 043515.

[26] A. R. Nehrir, K. S. Repasky, and J. L. Carlsten. "Micro pulse water vapor differential absorption lidar: transmitter design and performance". In: *Optics Express* **20** (2012), pp. 25137–25151.

[27] K. Repasky, D. Moen, S.Spuler, A.Nehrir, and J. Carlsten. "Progress towards an Autonomous Field Deployable Diode-Laser-Based Differential Absorption Lidar (DIAL) for Profiling Water Vapor in the Lower Troposphere". In: *Remote Sensing* **5**.12 (2013), pp. 6241–6259.

[28] S. M. Spuler, K. S. Repasky, B. Morley, D. Moen, M. Hayman, and A. R. Nehrir. "Field-deployable diode-laser-based differential absorption lidar (DIAL) for profiling water vapor". In: *Atmos. Meas. Tech* **8** (2015), pp. 1073–1087.

[29] J. D. Spinhirne. "Micro Pulse Lidar". In: *IEEE Trans. Geosci. Rem. Sens* **31**.1 (1993), pp. 48–55.

[30] A. Klehr, A. Liero, Th. Hoffmann, S. Schwertfeger, H. Wenzel, G. Erbert, W. Heinrich, and G. Tränkle. "Compact ps-pulse laser source with free adjustable repetition rate and nJ pulse energy on microbench". In: *Proc. SPIE, vol. 7953, no. 79531D.* **7953**. 79531D. 2011.

[31] S. Schwertfeger, A. Klehr, A. Liero, T. Hoffmann, H. Wenzel, and G. Erbert. "Picosecond pulses with more than 60 W peak power generated by a single stage all-semiconductor master-oscillator power-amplifier system". In: *European Conf. on Lasers and Electro-Optics and the European Quantum Electronics Conf.* CLEO Europe. Munich, Germany: EQEC 2011, 2011, CB7.4–WED.

[32] S. Schwertfeger, A. Klehr, T. Hoffmann, A. Liero, H. Wenzel, and G. Erbert. "Picosecond pulses with 50 W peak power and reduced ASE background from an all-semiconductor MOPA system". In: *Appled Physics B* **103** (2011), pp. 603–607.

[33] H. Wenzel, A. Klehr, S. Schwertfeger, A. Liero, Th. Hoffmann, O. Brox, M. Thomas, G. Erbert, and G. Tr änkle. "Compact sources for the generation of high-peak power wavelengthstabilized laser pulses in the picoseconds and nanoseconds ranges". In: *Proc. of SPIE* **8241**.82410V (2012).

[34] Amin Reza Nehrir. "development of an eye safe diode laser based micro pulse differential absorption lidar (MP-DIAL) for atmospheric water vapor and aerosol studies". PhD thesis. Montana state univesity, 2011.

[35] Claus Weitkamp, ed. *Lidar, Range-Resolved Optical Remote Sensing of the Atmosphere.* **102**. ISBN: 978-0-387-40075-4 (Print), 978-0-387-25101-1 (Online). Springer Series in Optical Sciences, 2005.

[36] F. Späth, A. Behrendt, S. Kumar Muppa, S. Metzendorf, A. Riede, and V. Wulfmeyer. "3-D water vapor field in the atmospheric boundary layer observed with scanning differential absorption lidar". In: *Atmos. Meas. Tech* **9** (2016), 1701Ű1720.

[37] V.Wulfmeyer, R. M.Hardesty, D. D. Turner, A. Behrendt, M. P. Cadeddu, P. D. Girolamo, P. Schlüssel, J. V. Baelen, and F. Zus. "A reviewof the remote sensingof lower tropospheric thermodynamic profiles and its indispensable role for the understanding and the simulation of water and energy cycles". In: *Reviews of Geophysics* **53** (2016), pp. 819–895.

[38] Syed Ismail and Edward V. Browell. "Airborne and spaceborne lidar measurements of water vapor profiles: a sensitivity analysis". In: *Appl. Opt. 28, 3603-3615 (1989* **28** (1989), pp. 3603–3615.

[39] F. Späth, A. Behrendt, S. K. Muppa, S. Metzendorf, A. Riede, and V. Wulfmeyer. "High-resolution atmospheric water vapor measurements with a scanning differential absorption lidar". In: *Atmos. Chem. Phys. Discuss.,* **14** (2014), pp. 29057–29099.

[40] Max Schiller. "A high power laser transmitter for ground based and airborne water vapor measurement in troposphere". PhD thesis. Universit"at Hohenheim, 2009.

[41] Anna-Lena Egeback, Kent A. Fredriksson, and Hans M. Hertz. "DIAL techniques for the control of sulfur dioxide emissions". In: *Appl. Opt.* **23** (1984), pp. 722–729.

[42] E. V. Browell, T. D. Wilkerson, and T. J. Mcilrath. "Water vapor differential absorption lidar development and evaluation". In: *APPLIED OPTICS* **Vol. 18**.No. 20 (1979), p. 3483.

[43] A Mendoza and C Flynn. "Handbook". In: *ARM TR-019* (2006).

[44] R. Coulter. "Micropulse Lidar (MPL) Handbook". In: *DOE/SC-ARM/TR-019* (1012).

[45] L.S. Rothman, I.E. Gordon, Y. Babikov, A. Barbe, D. Chris Benner, P.F. Bernath, M. Birk, L. Bizzocchi, V. Boudon, L.R. Brown, A. Campargue, K. Chance, E.A. Cohen, L.H. Coudert, V.M. Devi, B.J. Drouin, A. Fayt, J.-M. Flaud, R.R. Gamache, J.J. Harrison, J.-M. Hartmann, C. Hill, J.T. Hodges, D. Jacquemart, A. Jolly andJ. Lamouroux, R.J. Le Roy, G. Li, D.A. Long, O.M. Lyulin, C.J. Mackie, S.T. Massie, S. Mikhailenko, H.S.P. Müller, O.V. Naumenko, A.V. Nikitin, J. Orphal, V. Perevalov, A. Perrin, E.R. Polovtseva, and C. Richard. "The HITRAN2012 molecular spectroscopic database". In: *Journal of Quantitative Spectroscopy & Radiative Transfer* **130** (2013), pp. 4–50.

[46] A. Fix, G. Ehret, J. Löhring, D. Hoffmann, and M. Alpers. "Water vapor differential absorption lidar measurements using a diode-pumped all-solid-state laser at 935 nm". In: *Applied Physics B* **102** (2011), pp. 905 –915.

[47] J. Bösenberg. "DIAL System for high resolution water vapor measurements in the troposphere". In: *Proc. OSA Topical Meeting on Laser and Optical Remote Sensing: Instrumentation and Techniques* **paper MB 2- 1** (1987), pp. 22–25.

[48] W. B. Grant. "Differential absorption and Raman lidar for water vapor profile measure ments: a review". In: *Optical Engineering* **30**.1 (1991), pp. 40–48.

[49] A.Dinovitser, M. Hamilton, and R. Vincent. "Transmitter design for differential absorption water vapor LIDAR". In: *Proceedings of the 8th International Symposium on Tropospheric Profiling.* **255**. 5043. 2009, pp. 422–430.

[50] Kent A. Fredriksson and Hans M. Hertz. "Evaluation of the DIAL technique for studies on NO2 using a mobile lidar system". In: *Kent A. Fredriksson and Hans M. Hertz, "Evaluation of the DIAL technique for studies on NO2 using a mobile lidar system," Appl. Opt. 23, 1403-1411 (1984* **23** (1984), pp. 1403–1411.

[51] B. Sumpf, A. Klehr, T.N. Vu, G. Erbert, and G. Tränkle. "975 nm high-peak power ns-diode laser based MOPA system suitable for water vapor DIAL applications". In: *Proc. SPIE 9382, Photonics West, San Francisco, USA.* Ed. by 93821K. 93821K. 2015.

[52] Wills Ray Gregg. "Standard Atmosphere Propproper (0-86 km)". In: *report N0 147* (1976), pp. 397–409.

[53] M. D. Obland, K. S. Repasky, J. A. Shaw, and J. L. Carlsten. "Preliminary Testing of a Water-Vapor Differential Absorption LIDAR (DIAL) Using a Widely Tunable Amplified Diode Laser Source". In: *IEEE* (2006), pp. 3932–3935.

[54] M. D. Obland, K. S.Repasky, A. R.Nehrir, J. L.Carlsten, J. A Shaw, and J.L. Carlsten. "Initial results from a water vapor differential absorption lidar (DIAL) using a widely tunable amplified diode laser source". In: **6681**. Proc. SPIE 6681. 2007.

[55] F. Harth, T. Ulm, M. Lührmann, R. Knappe, A. Klehr, G. Erbert Th. Hoffmann, and J.A. L'huillier. "High power laser pulses with voltage controlled durations of 400 - 1000 ps". In: *Opt. Express* **20**.7 (2012), pp. 7002–7007.

[56] A. Klehr, T. Prziwarka, A.Liero, Th. Hoffmann, T.N. Vu, O. Brox, J. Fricke, F. Bugge, P. Ressel, A. Ginolas, H. Wenzel, H.-J. Wünsche, S. Schwertfeger, G. Erbert, and G. Tränkle. "High power picosecond and nanosecond diode laser sources in the wavelength range 650 nm to 1100 nm". In: **ISBN 978-1-4673-9177-1**. Ricoh Arena, Conventry, UK: Proc. of High Power Diode Lasers, Systems Conference (HPD), and Photonex, 2015, pp. 3–4.

[57] D. Jedrzejczyk, O. Brox, F. Bugge, J. Fricke, A. Ginolas, K. Paschke, H. Wenzel, and G. Erbert. "High-power distributed-feedback tapered master-oscillator power amplifiers emitting at 1064 nm". In: *High-Power Diode Laser Technology and Applications VIII, edited by Mark S. Zediker*. **7583**. 758317. Proc. of SPIE Vol. 2010.

[58] H. Wenzel, A. Klehr, S. Schwertfeger, A. Liero, Th. Hoffmann, O. Brox, M. Thomas, G. Erbert, and G. Tränkle. "Compact sources for the generation of high-peak power wavelengthstabilized laser pulses in the picoseconds and nanoseconds ranges". In: **8241**. 82410V. Proc. SPIE. SPIE, 2012.

[59] O. Brox, F. Bugge, A. Ginolas, A. Klehr, P. Ressel, H. Wenzel, G. Erbert, and G. Tränkle. "High-power ridge waveguide DFB and DFB-MOPA lasers at 1064 nm with a vertical farfield angle of 15$\hat{0}$". In: **7616**. 7616O. Proc. SPIE. SPIE, 2010.

[60] H. Wenzel, K. Paschke, O. Brox, F. Bugge, J. Fricke, A. Ginolas, A. Knauer, P. Ressel, and G. Erbert. "10W continuous-wave monolithically integrated master-oscillator power-amplifier". In: *ELECTRONICS LETTERS* **43**.3 (2007).

[61] H. Ghafouri Shiraz. *Distributed Feedback Laser Diodes and Optical Tunable Filters*. John Wiley and Sons Ltd, The Atrium, Southern Gate, Chichester, West Sussex PO19 8SQ, England, 2003.

[62] H. Wenzel, A. Klehr, M. Braun, F. Bugge, G. Erbert, J. Fricke, A. Knauer, P. Ressel, B. Sumpf, M. Weyers, and G. Tränkle. "Design and realization of high-power DFB lasers". In: **5595**. Proc. SPIE. 2004, pp. 110–123.

[63] H. Wenzel, J. Fricke, A. Klehr, A. Knauer, and G. Erbert. "High power 980 nm DFB RW lasers with a narrow vertical far field". In: *IEEE PTL* **18**.6 (2006), pp. 737–739.

[64] A. Klehr, H. Wenzel, S. Schwertfeger, O. Brox, A. Liero, Th. Hoffmann, and G. Erbert. "High peak-power nanosecond pulses generated with DFB RW laser". In: *Electron. Lett.* **47**.18 (2011), pp. 1039–1040.

[65] A.Klehr, A. Liero, Th. Hoffmann, S. Schwertfeger, H. Wenzel, G. Erbert, W. Heinrich, and G. Tränkle. "Compact ps-pulse laser source with free adjustable repetition rate and nJ pulse energy on microbench". In: *Novel In-Plane Semiconductor Lasers X*. **7953**. 79531D. Proc. of SPIE. SPIE, 2011.

[66] H. Wenzel, F. Bugge, M. Dallmer, F. Dittmar, J. Fricke, K. H. Hasler, and G. Erbert. "Fundamental-Lateral Mode Stabilized High-Power Ridge-Waveguide Lasers With a Low Beam Divergence". In: *IEEE Photonics Technology Letters* **20**.3 (2008), pp. 214–216.

[67] K.-H. Hasler, B. Sumpf, P. Adamiec, F. Bugge, J. Fricke, P. Ressel, H. Wenzel, G. Erbert, and G. Tränkle. "5-W DBR Tapered Lasers Emitting at 1060 nm With a Narrow Spectral Linewidth and a Nearly Diffraction-Limited Beam Quality". In: *Photonics Technology Letters, IEEE* **20**.19 (2008), pp. 1641–1650.

[68] H. Wenzel, J. Fricke, J. Decker, P. Crump, and G. Erbert. "High-Power Distributed Feedback Lasers With Surface Gratings: Theory and Experiment". In: *IEEE Journal of selected topics in quantum electronics* **21**.6 (2015), pp. 1502707–1502714.

[69] *Integrated 1060nm MOPA pump source for high-power green light emitters in display technolog*. 2008.

[70] P. Nguyen. "Investigation of spectral characteristics of solitary diode lasers with integrated grating resonator". PhD thesis. Technische Universität Berlin, 2010.

[71] B. Sumpf, A. Klehr, G. Erbert, and G. Tränkle. "Application of 940 nm high-power DFB lasers for line-broadening measurements at normal pressure using a robust and compact setupŠ". In: *Appl. Phys. B* **106**.2 (2012), pp. 357–364.

[72] J. Fricke, W. John, A. Klehr, P. Ressel, L. Weixelbaum, H. Wenzel, and G. Erbert. "Properties and fabrication of high-order Bragg gratings for wavelength stabilization of diode lasers". In: *Semicond. Sci. Technol* **27**.055009 (2012).

[73] H. Wenzel, F. Bugge, M. Dallmer, F. Dittmar, J. Fricke, K.H. Hasler, and G. Erbert. "Fundamental-Lateral Mode Stabilized High-Power Ridge-Waveguide Lasers With a Low Beam Divergence". In: *IEEE Photonics Technol. Lett.* **20**.3 (2008), pp. 214–216.

[74] A. Dinovitser, M.W. Hamilton, and R. A. Vincent. "Stabilized master laser system for differential absorption lidar". In: *APPLIED OPTICS* **49**.17 (2010), pp. 3274–3281.

[75] J. Fricke, A. Klehr, O. Brox, W. John, A. Ginolas, P. Ressel, and G. Erbert G. "Y-branch coupled DFB-lasers based on high-order Bragg gratings for wavelength stabilization". In: *Semiconductor Science and Technology* **28**.3 (2013).

[76] P. Crump, S. Böldicke, C.M. Schultz, H. Ekhteraei, H. Wenzel, and G. Erbert. "Experimental and theoretical analysis of the dominant lateral waveguiding mechanism in 975 nm high power broad area diode lasers". In: *Semicon.Sci.Technol* **27**.045001 (2012).

[77] B. Eppich. "Optical Design of Beam Delivery and Beam Forming Systems". In: *Optik and Photonik* **2** (2008).

[78] A. Liero, A. Klehr, S. Schwertfeger, T. Hoffmann, and W. Heinrich. "Laser driver switching 20 A with 2 ns pulse width using GaN". In: Microwave Symposium Digest (MTT), 2010 IEEE MTT-S International, 2010.

[79] S. Spiessberger, M.Schiemangk, A. Sahm, A. Wicht, H. Wenzel, G. Erbert, and G. Tr änkle. "Narrow-linewidth high-power semiconductor-based laser module". In: *Lasers and Electro-Optics Europe (CLEO EUROPE/EQEC)*. IEEE, 2011.

[80] R. Maciejko K. J. Kasunic D. M. Adams A.Champagne J. Camel and B. Tromborg. "Linewidth Broadening in a Distributed Feedback Laser Integrated With a Semiconductor Optical Amplifier". In: *IEEE JOURNAL OF QUANTUM ELECTRONICS, VOL. 38, NO. 11, NOVEMBER 2002* **38**.11 (2002), pp. 1493–1502.

[81] A. Egan, C.Z. Ning, J.V. Moloney, R.A. Indik, M.W. Wright, D.J Bossert, and J.G. McInerney. "Dynamic instabilities in master oscillator power amplifier semiconductor lasers". In: *Quantum Electronics, IEEE Journal* **34**.1 (1998), pp. 166 –170.

[82] G. C. Dente and M. L.Tilton. "Modeling multiple-longitudinal-mode dynamics in semiconductor lasers". In: *Quantum Electronics, IEEE Journal* **34**.2 (1998), pp. 325 –335.

[83] B. Sumpf, K-H. Hasler, P. Adamiec, F. Bugge, F. Dittmar, J. Fricke, H. Wenzel, M. Zorn, G. Erbert, and G. Tränkle. "High-Brightness Quantum Well Tapered Lasers". In: *IEEE JOURNAL OF SELECTED TOPICS IN QUANTUM ELECTRONICS* **15**.3 (2009), pp. 1009–1011.

[84] T. N.Vu, A. Klehr, B. Sumpf, H. Wenzel, G. Erbert, and G. Tränkle. "973 nm wavelength stabilized hybrid ns-MOPA diode laser system with 15.5 W peak power and a spectral line width below 10 pm". In: *Semiconductor Lasers and Laser Dynamics VI*. **9134**. 91340T. SPIE. Brussels: Proc. SPIE 9134, 2014.

[85] T. Ulm, F. Harth, A. Klehr, G. Erbert, and J. L'huillier. "Passively mode-locked 1 GHz MOPA system generating sub-500-fs pulses after external compression". In: **8432**. SPIE. SPIE Proceedings, 2012.